

# Silicon Photonic Filters: A Pathway from Basics to Applications

Nabarun Saha, Giuseppe Brunetti, Annarita di Toma, Mario Nicola Armenise, and Caterina Ciminelli\*

Silicon photonics has found a profound place among emerging technologies in the past few decades due to several advantages. Due to a series of breakthroughs and increased funding from private and government sectors, the development of silicon photonics has accelerated especially starting from the two years 2004–2005 with a persisting and ever-growing momentum. Among various components, the silicon photonic filters that selectively pass or block particular wavelengths with a finite bandwidth have found particular interest as they are useful in signal processing in different fields ranging from optical communication to microwave photonics and quantum photonics. Herein, a comprehensive review of silicon photonic filters focusing on the four most commonly used architectures, such as microring resonators, waveguide Bragg grating, Mach–Zehnder interferometers, and arrayed waveguide grating, encapsulating basics, and guidelines, in terms of simulating tools and topologies, of realizing reconfigurable and high-performing filters for several applications, is provided. The novelty of this review relies on the fact that it summarizes these filter architectures covering a broad range of applications concisely and constructively and includes the basics, growth, and future trends, providing a clear understanding and importance of silicon photonic filters from research to commercialization perspective.

manufacturing complementary metal-oxide semiconductor (CMOS)-compatible technology.<sup>[2,3]</sup> Silicon photonics brings optical communications into the fabrication space of the semiconductor industry, mainly enabling low-cost and high-volume assembly. The optoelectronic functions are fabricated on the same CMOS wafers using the same equipment and methods as electronic chips. The wafers are processed in the same fabs as those running electronic chips. The wafers are diced into chips just like electrical ones. The great crystal quality of silicon and low-cost per unit area of silicon wafers already leads to the high-density integration of electronic components. Since the photonic components can be realized in the same silicon substrate, it also leads to the possibility of integrating different electronics and optical components in a single microchip.<sup>[4]</sup>


The high-index contrast of silicon ( $=3.47$  at  $1550$  nm) over the surroundings ( $=1.44$  at  $1550$  nm for  $\text{SiO}_2$ ) ensures the subwavelength level of light guiding and

thus close spacing, tight bending, and eventually high-density integration of different optical components on a single chip as well as low energy consumption due to miniaturization. The competing materials such as silicon nitride ( $\text{Si}_3\text{N}_4$ ) and lithium niobate ( $\text{LiNbO}_3$ ) have much lower-index contrast. The refractive index of  $\text{Si}_3\text{N}_4$  at  $1550$  nm is 2 whereas for  $\text{LiNbO}_3$  it is 2.21 and 2.13 corresponding to ordinary and extraordinary polarization respectively, clearly reflecting the advantages of silicon in developing miniaturized components like filters. Another advantage is the possibility of hybrid or monolithic integration of different silicon photonic components such as filters, modulators, and routers with the source and detectors on a single microchip. However, the indirect bandgap nature of silicon makes it challenging to realize light sources and detectors with it. Researchers are coming up with different approaches to overcome this problem, such as integrating with III/V material through bonding or direct growth approach<sup>[5–8]</sup> or group IV materials such as germanium.<sup>[9,10]</sup> In addition, rare earth materials can be doped within the photonic layers to realize an on-chip laser source.<sup>[11,12]</sup> Furthermore, the large thermo-optic coefficient (TOC) of silicon<sup>[13]</sup> as well as the electro-optic (EO) effect through the plasma dispersion function<sup>[14]</sup> facilitates realizing reconfigurable devices in silicon photonic chips. The TOC of

## 1. Introduction

Silicon photonics is an important branch of science and technology in which silicon is used as the optical medium to guide, transmit, process, and manipulate the propagation of light on a thumb-size scale. Since its invention in the mid-1980s,<sup>[1]</sup> the growth of silicon photonics in different fields is quite astonishing due to various advantages. The most favorable argument is its compatibility with mature silicon integrated circuits (IC)

N. Saha, G. Brunetti, A. di Toma, M. N. Armenise, C. Ciminelli  
Optoelectronics Laboratory  
Department of Electrical and Information Engineering  
Politecnico di Bari  
Orabona 4 street, 70125 Bari, Italy  
E-mail: caterina.ciminelli@poliba.it

 The ORCID identification number(s) for the author(s) of this article can be found under <https://doi.org/10.1002/adpr.202300343>.

© 2024 The Authors. Advanced Photonics Research published by Wiley-VCH GmbH. This is an open access article under the terms of the Creative Commons Attribution License, which permits use, distribution and reproduction in any medium, provided the original work is properly cited.

DOI: 10.1002/adpr.202300343

silicon is  $1.8 \times 10^{-4} \text{ } ^\circ\text{C}^{-1}$ <sup>[13]</sup> much higher than that of  $\text{Si}_3\text{N}_4$  ( $2.5 \times 10^{-5} \text{ } ^\circ\text{C}^{-1}$ )<sup>[15]</sup> and  $\text{LiNbO}_3$  ( $3.67 \times 10^{-5} \text{ } ^\circ\text{C}^{-1}$ ,  $4.18 \times 10^{-6}$ ).<sup>[16]</sup> Although in  $\text{LiNbO}_3$  the EO effect is used to realize the reconfigurability, its incompatibility with the standard CMOS fabrication technology provides a bottleneck toward mass production. On the other hand,  $\text{Si}_3\text{N}_4$ -based waveguides show the lowest propagation losses ( $0.1\text{--}0.5 \text{ dB cm}^{-1}$ ) but they suffer from high power consumption due to low TOC as well as the absence of EO effect. Silicon also has a very broad low-loss wavelength window spanning from  $1.1 \mu\text{m}$  to nearly  $7 \mu\text{m}$ <sup>[17]</sup> comparable to  $\text{Si}_3\text{N}_4$  ( $0.4\text{--}6.7 \mu\text{m}$ ) and  $\text{LiNbO}_3$  ( $0.35\text{--}4.5 \mu\text{m}$ ).<sup>[18]</sup> Moreover, silicon photonic devices could reach a high modulation rate enabling the design of elevated-performance passive components that can be simulated through a huge variety of hierarchical set design tools. All these combinations are scaling up silicon photonics from a promising topic in science and technology to a large-scale industrially viable platform.<sup>[19]</sup>

As a result, Bookham Inc. launched the first product on the silicon photonics platform in 1998, and since then tremendous industrial growth has been observed. The total market value of silicon photonics in 2022 was \$68M and it is estimated that by 2028 the market will be close to \$613M (Figure 1a) by the research firm Yole group.<sup>[20]</sup>

To satisfy the growing demand for silicon photonic components, different research groups all over the world are extensively working on those components and their integration, and this corresponds with the growth in the number of research articles as can be seen from the Scopus data (Figure 1b).<sup>[21]</sup> The growth has been observed in different fields including optical interconnections, data center and long-haul transceivers, microwave photonics (MWP), photonic computing, biomedical and life sciences, home wiring and consumer applications, sensors, etc. Among various silicon photonic elements, one of the most important components is the silicon photonic filter which selectively passes or blocks wavelengths, and is suitable for spectral manipulations, offering various applications ranging from optical communications to MWP and quantum photonics.

Among various silicon photonic components, this article meticulously reviews silicon photonic filters. Indeed, driven by advanced integrated photonics technologies, integrated silicon photonic filters have demonstrated to guarantee reconfiguration and wideband filtering functionalities that were difficult to

achieve using conventional electronics exhibiting an improvement in terms of compactness, lightweight, stability, low power consumption, and low latency at the same time.<sup>[22]</sup> Furthermore, they can benefit from photonics intrinsic advantages as very low propagation losses, immunity against electromagnetic interferences (EMI), large immunity to radiations, and good mechanical features such as flexibility and resistance to vibrations/shocks.<sup>[23]</sup>

Bandpass filters are one of the essential building blocks in wireless communications systems. For this reason, studies have been carried out to develop design theories and methods for reconfigurable bandpass filters. Nowadays, the best results in terms of reconfigurable electronic bandpass filters are reported in refs. [24–26]. In particular, Jeong et al.<sup>[24]</sup> proposed an adaptive third-order absorptive filter based on a microstrip line with a central frequency spanning from 1.35 to 1.65 GHz, a 3 dB fractional bandwidth from 5 to 10% of the central frequency, a return loss (RL) larger than 17.20 dB, and an insertion loss (IL) lower than 5 dB. Another interesting solution has been proposed by Lalbakhsh et al.<sup>[25]</sup> Here, a dual-band band-pass filter (BPF) is proposed using double-coupled, high-impedance transmission lines and a bent T-shaped resonator loaded by L-shaped stubs. The filter has a fractional bandwidth of 78.9% centered at 7.6 GHz, characterized by an IL of 0.6 dB, an RL of 16.32 dB, and a footprint of  $18.4 \times 9 \text{ mm}^2$ . A compact dual-band bandpass filter based on parallel coupled lines and shorted stubs has been presented in ref. [26]. The authors demonstrated a reconfigurability of both central frequency (1.45–2.67 GHz) and fractional bandwidth (11.7–2.62%), with maximum IL of 2.5 dB, minimum RL of 14 dB, and a footprint of  $41.5 \times 12.2 \text{ mm}^2$ .

However, due to the electronic bottleneck, traditional electronic filters are facing significant challenges for meeting the exponentially increasing capacity of next-generation radio-frequency (RF) systems. Next-generation communications' need for ultrahigh transmission speed ( $100 \text{ Gb s}^{-1}$ ) in the band from 30 to 300 GHz while electronic filters to date are limited to 10 GHz. To overcome these limits, a synergy among integrated coherent optics, integrated MWP, and photonic digital signal processing seems to be the new cutting-edge solution.<sup>[27]</sup>

Recently, a photonic bandpass filter based on cascaded decoupled microring resonators (MRRs) whose coupling regions are constructed by a tunable balanced MZI is demonstrated.<sup>[28]</sup> This device experimentally proved to achieve a bandwidth

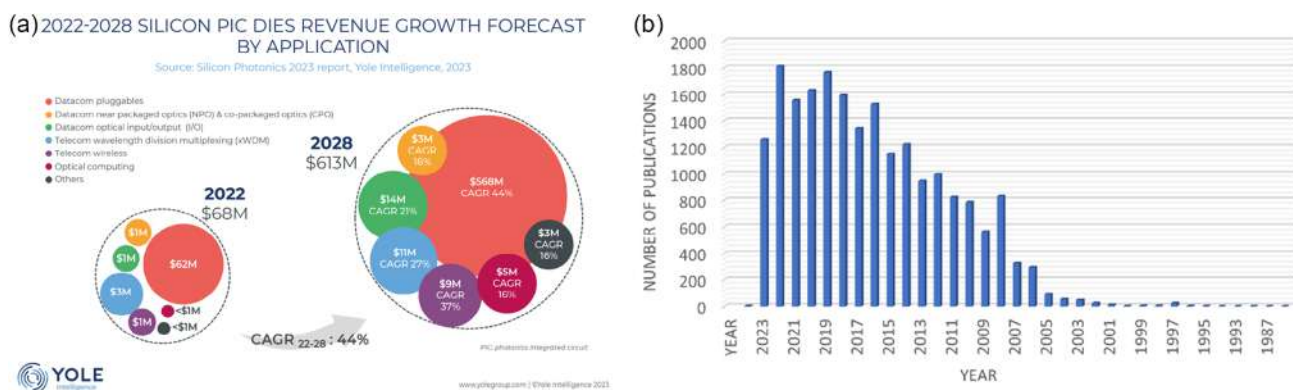


**Figure 1.** a) The growing market of silicon photonics as predicted by Yole development. Reproduced with permission.<sup>[20]</sup> Copyright 2023, Yole Développement. b) The growth of research articles published on silicon photonics over the years according to Scopus data.<sup>[21]</sup>

reconfiguration from 0.38 to 15.74 GHz, a shape factor optimization from 2 to 1.23, and a central frequency tuning from 4 GHz to 21.5 GHz. The fiber-to-fiber IL of the chip is 2.6 dB, the rejection ratio of sidebands is 34 dB, and the footprint is about  $2.8 \times 3 \text{ mm}^2$ .

It can be noticed that silicon photonic filter solutions can provide significant improvements compared to their electronic counterparts, especially in terms of device size (at least 20 times smaller) and tunability range, allowing at the same time to push up the frequency meeting next-generation communication requirements.

Going into details, silicon filters typically rely on interference or resonance to selectively pass or block specific wavelengths. Taking advantage of its integrability with electronics, silicon photonic filters lead to the development of various compact and power-efficient high-speed communication systems as well as the development of MWP and quantum photonics through signal processing in integrated geometry. Since its invention in the 1980s, silicon photonics have seen hardly any growth until the 2000s.<sup>[20,29]</sup> One possible reason may be that the dimension of silicon waveguides is only a few hundred nanometers. With the advancement of microfabrication technology, in the early 2000s, the linewidth reached  $\approx 100 \text{ nm}$ , providing a boom to silicon photonics.<sup>[30]</sup> This further gets a boost due to interest shown by different pioneering companies like Intel, Rockley, etc. During its initial stage, silicon photonic filters stayed within research laboratories and made a transition to commercialization in 2010, as multiple companies started offering various applications in data centers, telecommunications, etc. The year-wise growth of silicon photonics is shown in **Figure 2**, giving a clear perspective.

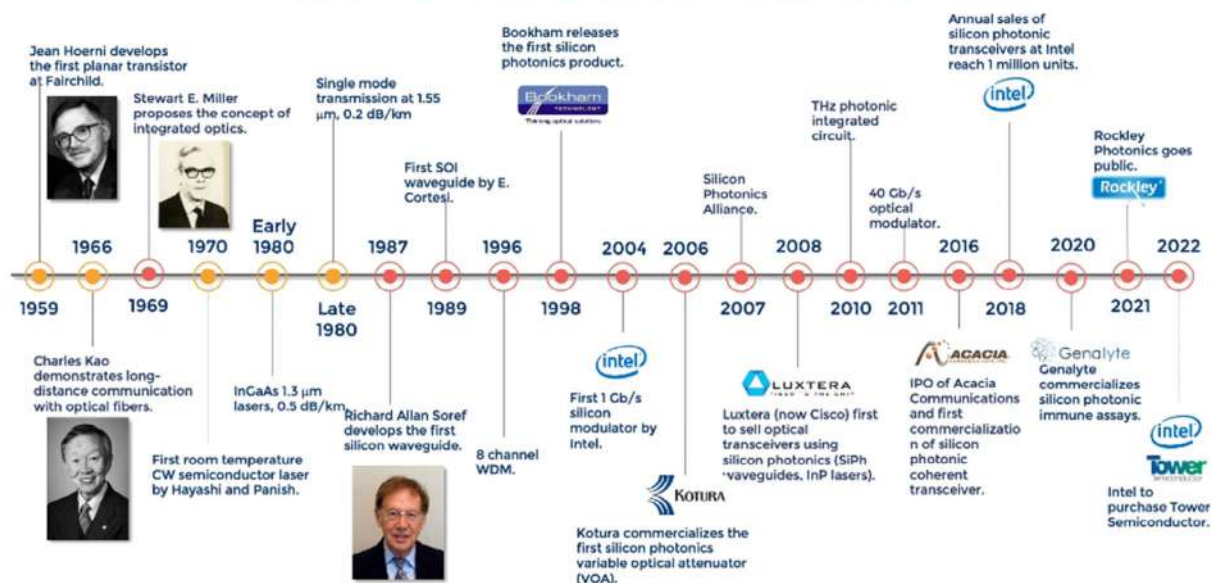
Silicon photonic filters can be categorized as passive and active filters. Passive filters simply pass or block selective wavelengths without offering any tunability, making their application limited. However, it offers structural simplicity and does not require any external power source. On the other hand, the active filters are integrated with external power sources and offer much freedom in controlling the filters' performance in terms of different parameters like central frequency, bandwidth, transmittance etc., making them suitable for signal processing. This article includes both types of filters and, instead of classifying them, it focuses on the development trends of different configurations in an application-specific manner.

The significance of the silicon photonic filters relies on the fact that they can be densely integrated due to their high-waveguide contrast, versatility in realizing different active configurations with low-power consumption thanks to high TOC and availability of plasma dispersion effect, their integrability with electronics through well-established CMOS-compatible chip generation offering cost-effective and power-efficient solutions, on-chip integration with silicon modulators making it suitable especially for MWP, strong third-order nonlinearity paving the way of on-chip photon pair generation imperative for quantum photonics, etc.

In this article, the silicon photonic filters mainly based on four commonly used architectures have been reviewed, such as MRRs, Mach-Zehnder interferometers (MZI), waveguide Bragg grating (WBG), and arrayed waveguide grating (AWG) from their basic principle to their applications in optical communications, MWP, and quantum photonics. **Table 1** depicts the two main classifications and subclassifications of silicon photonic filters discussed in this review.

## 1959-2022 SILICON PHOTONICS HISTORICAL PERSPECTIVE

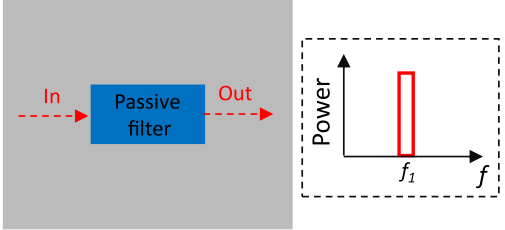
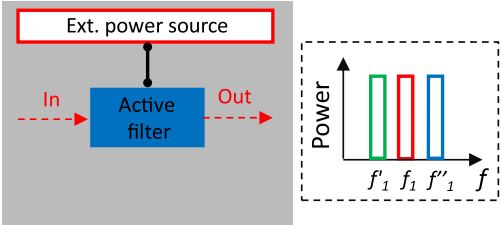
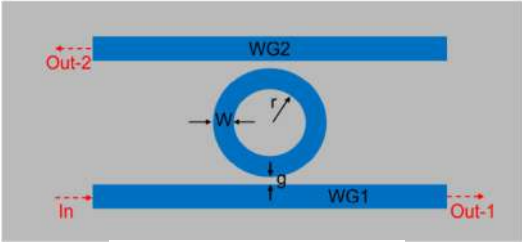
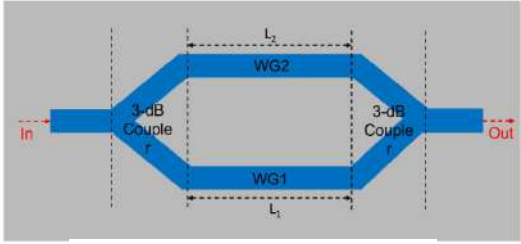
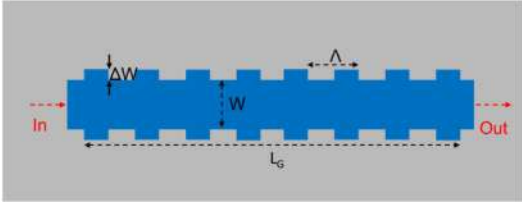
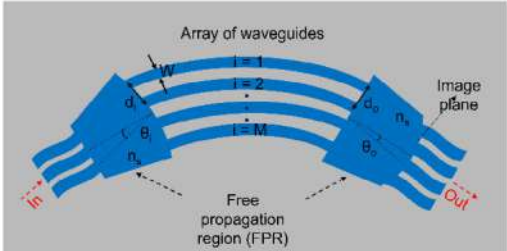
Source: Silicon Photonics report, Yole Intelligence, 2022



www.yolegroup.com | @Yole Intelligence 2023

**Figure 2.** Historical growth of silicon photonics over the year. Reproduced with permission.<sup>[20]</sup> Copyright 2023, Yole Développement.

**Table 1.** Silicon photonic filters classification.

Classification principle	
Tunability	
 <p>Passive</p>	 <p>Active</p>
Building Block	
 <p>Micro-Ring Resonator (MRR)</p>	 <p>Mach-Zehnder Interferometers (MZI)</p>
 <p>Waveguide Bragg Grating (WBG)</p>	 <p>Arrayed Waveguide Grating (AWG)</p>

Covering all the application fields in a concise manner, this article provides a detailed review of silicon photonic filters which also extends the discussion presented on wavelength division multiplexing (WDM) filters in ref. [31]. Further, this article includes the basic analysis of silicon waveguides and the operating principle of four commonly used architectures indicating their differences, a description of different approaches to realize reconfigurability, an extensive overview of numerical techniques with constructive suggestions, applications-oriented development trends, and challenges and future perspective with market growth. In Section 2, first, the basic silicon waveguide geometry is studied, followed by the discussion of four different filter architectures including their working principle and spectral properties. In Section 3, the main simulation tools have been analyzed aiming at driving the engineers to choose the most suitable solver following the target device and/or application. Next, in Section 4, a brief review has been given about the possible ways to realize reconfigurability to make the circuit more flexible. In the next sections, a comprehensive review has been presented to evaluate and analyze the different proposed filters with particular attention to applications in optical communication, microwave,

and quantum photonics. Before concluding the article, a brief discussion about the industrialization of silicon photonics is presented, highlighting its high market value.

## 2. Silicon Waveguide and Filter Topologies

In silicon photonics, the research and developmental work is mainly focused on a subwavelength silicon-on-insulator (SOI) geometry, in which a silicon core is formed over a silicon substrate interleaved by 2–3  $\mu\text{m}$ -thick silica box layer. The most commonly used thickness of the silicon core is 220 nm. The large refractive index contrast ( $\Delta n > 2$  at 1550 nm) between the silicon core and surroundings ensures strong confinement of the light guided in a strip- or a rib-shape waveguide, whose cross sections are shown in Figure 3a,b, respectively.

The confined light in the core is usually referred to as guided mode labeled with certain field distributions and modal effective index. In general, the waveguide modes can be defined as the allowed solutions of a given boundary value problem, as the continuity of the electric and magnetic field components at the

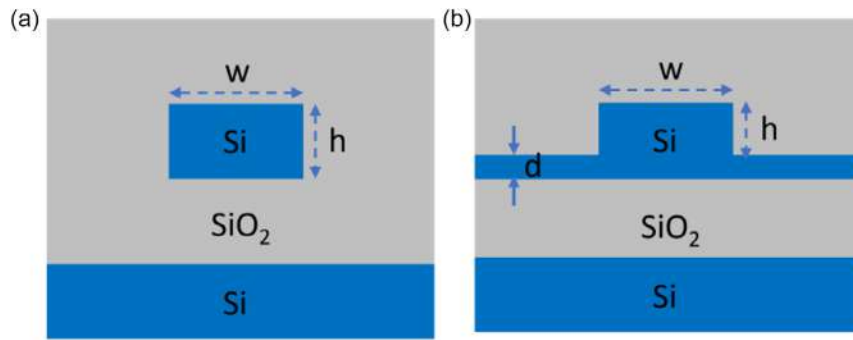


**Figure 3.** Cross-sectional view of the two most commonly used geometry in silicon photonics: a) ridge and b) rib waveguide.

waveguide interfaces. According to the relative values of two electric field components,  $E_x$  and  $E_y$ , the modes can be classified as transverse electric (TE) mode and transverse magnetic (TM) mode, for propagation along the  $z$ -direction. When the ratio between  $E_x$  and  $E_y$  is  $>1$ , the modes are referred to as TE mode whereas it is called TM mode. The field distribution of the fundamental TE and TM modes has been shown in **Figure 4a**, with the relative  $E_x/E_y$  ratio.

The variation of the modal effective index with the core width for the strip/ridge waveguide with silica as the surroundings is shown in **Figure 4b** with a 220 nm-thick core. As evident from the figure, the silicon waveguide supports only the fundamental TE mode up to 450 nm above which it supports higher-order TE modes. It should be noted that a significant trade-off between the mode confinement and scattering loss exists for silicon waveguides. Although the large-index contrast ensures strong mode

confinement, it also causes high scattering losses due to sidewall roughness. **Figure 4c** reports a bird's-eye view of the scanning electron microscope (SEM) image of a silicon waveguide before the formation of silica upper cladding that shows sidewall striation.<sup>[32]</sup> This is the major source of the propagation loss in the silicon waveguide which is taking place due to strong scattering from the rough sidewall of the silicon waveguide. At larger widths, the guided mode is more confined in the silicon core, reducing the power outside the core which makes it less vulnerable to the sidewall roughness. As a result, the scattering loss reduces and results in lower propagation loss. The propagation loss is found to be much lower at a width of 500 nm than at 450 nm<sup>[33]</sup> thanks to a better mode field confinement. At 500 nm, although the waveguide supports the higher-order mode, it still effectively acts as a single-mode waveguide due to the highly lossy nature of the higher-order mode. As a result, in most of

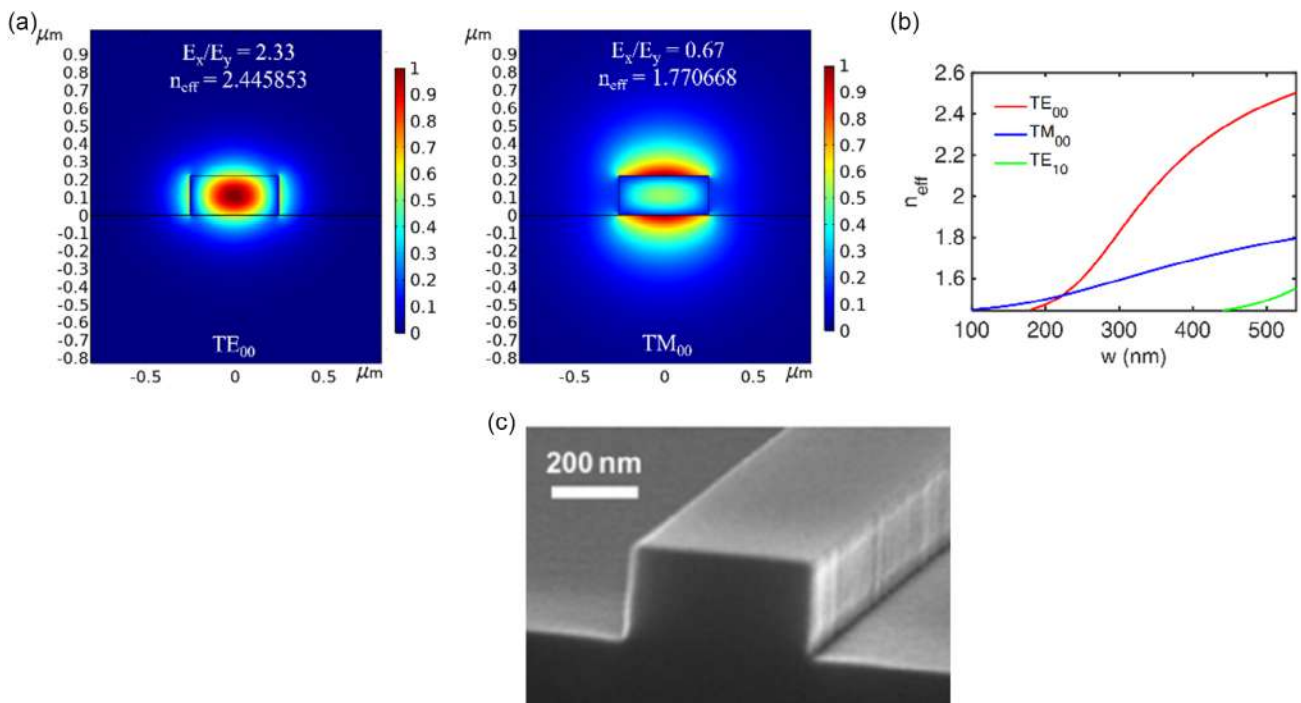


**Figure 4.** a) Field distribution of the  $TE_{00}$  mode and  $TM_{00}$  mode with the relative amplitude of two field components and effective index values. b) Variation of the modal effective index as a function of waveguide width for a commonly used height of 220 nm. c) Bird's eye view of the Si waveguide before the formation of silica upper cladding, showing side wall roughness. Reproduced with permission.<sup>[32]</sup> Copyright 2016, MRS Communications.

the research works for single-mode operation, the silicon waveguide's core width is considered to be between 450 and 500 nm.

The filters in the SOI platform use the guided mode property to selectively pass or block different wavelengths with finite bandwidth and extinction ratio (ER). The performance metrics for an ideal filter include flat top response, low in-band ripples, and sharp roll-off with strong rejection outside passing bandwidth. The most commonly used geometries and their spectral

behaviors are shown in **Figure 5**, respectively, known as 1) RRs, 2) WBG, 3) MZI, and 4) AWG. Although more complex topologies have been proposed in the literature, a brief discussion about the basic structures of these filters and their spectral behavior has been given below for fundamental understanding.

In the simplest configuration, RR consists of a straight waveguide coupled with a ring-shaped waveguide having a gap  $g$ . The top view of a RR is shown in Figure 5a in which  $r$  and  $w$  denote

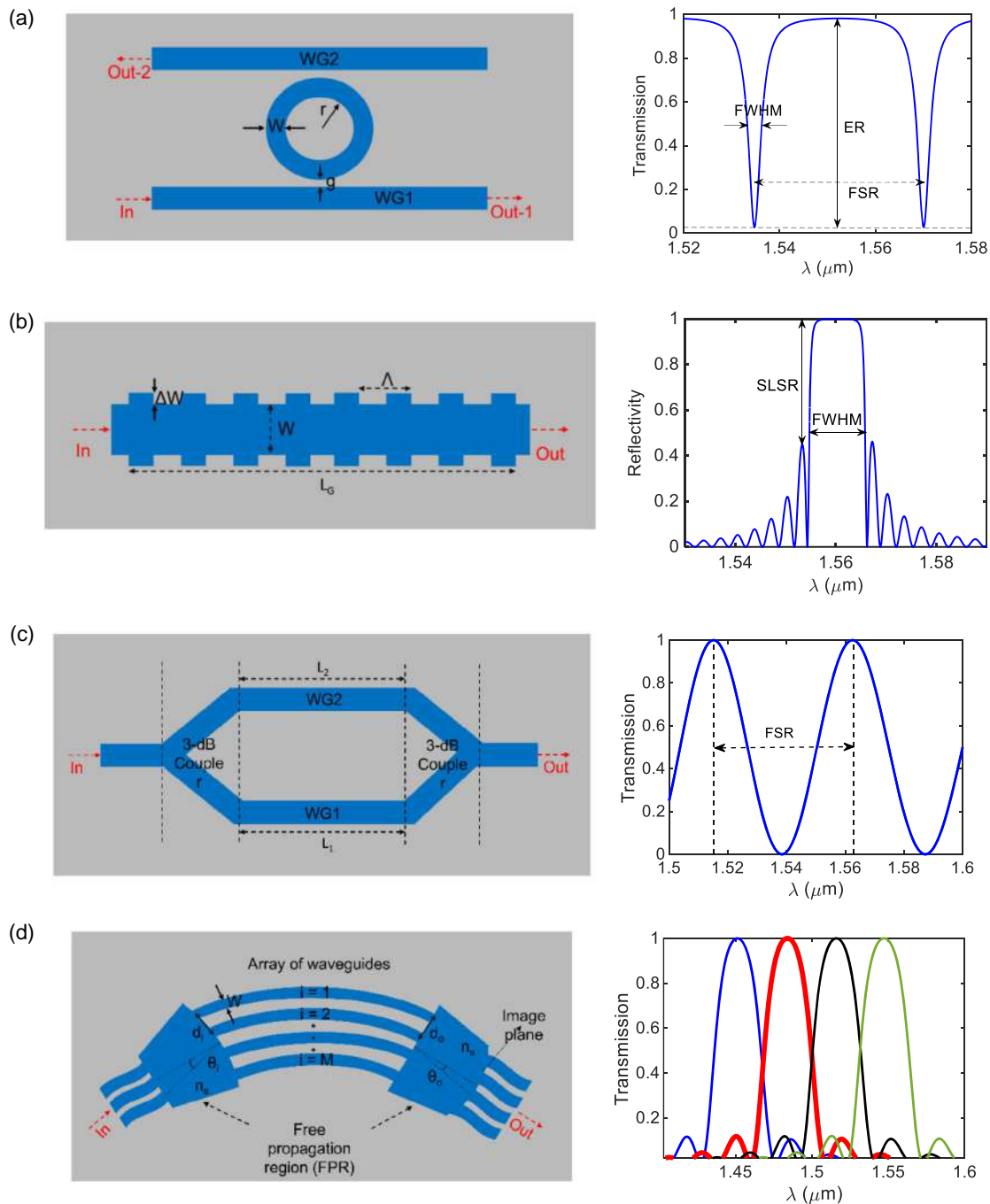


**Figure 5.** Schematic diagram of four commonly used geometry of Si photonic filters and their spectral characteristics presented besides a) MRRs, b) WBG, c) MZI, and d) AWG.

the radius of the ring and width of the waveguide, respectively. The light travelling through the straight waveguide (WG1) excites the mode inside the ring waveguide. The structure is in resonance when the built-in roundtrip phase inside the ring is an integer multiple of  $2\pi$ .

The straight waveguide is used to feed the resonator cavity as well as extract the transmittance characteristics. In another popular configuration, an additional straight waveguide is placed on the opposite side concerning WG1. In this configuration, the RR acts as an add-drop filter and the output port (Out-2) acts as the drop port. The resonating condition can be expressed as<sup>[34,35]</sup>

$$k_0 L n_{\text{eff}} = 2\pi m \rightarrow \lambda = n_{\text{eff}} L / m \quad (1)$$

where  $k_0 = 2\pi/\lambda$  is the propagation constant in free space,  $L = 2\pi r$  is the circumference of the ring, and  $n_{\text{eff}}$  is the modal effective index of the waveguide. The transmittance spectrum (Out-1) of a RR is shown in Figure 5a, including its spectral features. The spectral behavior of an RR can be characterized by the following features: full-width half maximum (FWHM) that represents the 3 dB spectral bandwidth, free spectral range (FSR) estimated as the separation between consecutive spectral dips (or peaks in Out-2 in add-drop configuration), which is inversely proportional to the length of the resonator cavity  $L$ , and the ER, as the contrast of the spectrum. These parameters largely depend on the coupling power coefficient  $K$  and the propagation losses  $\alpha$ .<sup>[35]</sup> To enlarge the coupling region and then the coefficient  $K$ , racetrack resonators have been proposed, that show the same features of RR.

The WBG is a periodic modulation of the effective refractive index of a waveguide along the propagation direction. In silicon photonics, it is generally realized by periodic corrugation of the sidewalls (so-called sidewall grating, shown in Figure 5b) or the top surface of a straight waveguide (so-called top grating). Figure 5b illustrates a sidewall grating in which  $W$  refers to waveguide width whereas  $\Delta W$  and  $\Lambda$  indicate the depth of the periodic corrugation and the period, respectively. The periodic variation in waveguide core width leads to a periodic change in effective refractive index, therefore creating a resonating structure. The constructive interference takes place between the incident and the reflected light when the roundtrip phase generated in each grating period is an integer multiple of  $2\pi$ . The constructive interference build-up in each grating period adds up and produces a high reflectance at the resonance wavelength which increases with the increase in grating length. Following the roundtrip phase, the resonance condition can be expressed as<sup>[36,37]</sup>

$$2k_0 \Lambda n_{\text{eff}} = 2\pi m \rightarrow 2\Lambda n_{\text{eff}} = \lambda / m \quad (2)$$

Here,  $m$  refers to the order of the Bragg grating, which is in general considered to be 1. The reflected spectrum of a WBG is shown in Figure 5b. The reflected spectrum is characterized by FWHM, peak reflectivity, both dependent on the grating strength or the corrugation depth  $\Delta W$  and grating length  $L_G$ , and sidelobe suppression ratio (SLSR), expressed as the difference between peak reflectivity and the reflectivity of the first side lobe. Moreover, it should be noted that the resonance wavelength corresponding to  $m = 2$  is usually well away from the  $m = 1$ ; therefore, WBG produces a nearly FSR-free spectrum.

MZI consists of an input and an output waveguide, two 3 dB couplers, acting as splitter at the input and combiner at the output, and two intermediate waveguide arms ( $L_1$  and  $L_2$  longs) referred to as reference (WG1) and phase shifter/sensing arm (WG2), as shown in Figure 5c. As a 3 dB coupler, different techniques such as Y-splitter, straight or bend directional coupler (DC), multimode interferometers (MMIs), etc. have been reported in the literature. The phase difference created between the two arms decides the output spectrum of the structure. The spectrum shows peaks or dips following constructive or destructive interference between the two arms. For constructive interference, the phase difference created between two arms should be an integer multiple of  $2\pi$ , which can be expressed as<sup>[38]</sup>

$$k_0 (n_{\text{eff}1} L_1 - n_{\text{eff}2} L_2) = 2\pi m \rightarrow \lambda = (n_{\text{eff}1} L_1 - n_{\text{eff}2} L_2) / m \quad (3)$$

where  $L_1$  and  $L_2$  are the lengths of two arms and  $n_{\text{eff}1}$  and  $n_{\text{eff}2}$  are their modal effective indices. In general, the waveguide features of the two arms in MZI are chosen to be the same ( $n_{\text{eff}1} = n_{\text{eff}2}$ ); thus, the phase difference is created by the length difference between the two arms. The output spectrum shows a sinusoidal-like behavior, as shown in Figure 5c, where the FSR and FWHM can be estimated.

An AWG consists of five components: an input waveguide, a set of a phased array of waveguides sandwiched between two free propagating regions (FPR) or star coupler, and output waveguides as shown in Figure 5d. The incoming light enters the input FPR and diverges laterally toward the waveguide array. In the arrayed waveguide, the length of each waveguide is such that a phase difference of  $2\pi$  builds between two adjacent waveguides corresponding to a central wavelength. In the image plane of the output FPR, the plane waves with constant phase delay interfere constructively and deliver a bandpass characteristic around a central wavelength at each output waveguide. As the free propagation region, the two most commonly used couplers are Rowland-type star couplers and confocal-type star couplers.<sup>[39]</sup> The grating resonance condition is given as

$$n_s d_i \sin\theta_i + n_{\text{eff}} \Delta L + n_s d_o \sin\theta_o = m\lambda \quad (4)$$

where  $n_s$  and  $n_{\text{eff}}$  respectively represent the slab refractive index and effective index of the arrayed waveguides,  $\Delta L$  denotes the constant difference in length between two adjacent arrayed waveguides, and  $d_i$  and  $d_o$  is the center-to-center spacing between the arrayed waveguides at the input and output star coupler. Figure 5d illustrates the 4-channel spectrum of an AWG.

In summary, in RRs, a circular waveguide geometry forms a resonant cavity in which the peaks in the transmission spectrum correspond to the roundtrip phase equal to an integer multiple of  $2\pi$ . WBG in silicon photonics is realized by a periodic corrugation of the waveguide's geometry. The peak in the reflected spectrum refers to the  $2\pi$  roundtrip phase inside each grating period. In the MZI configuration, the interference between two silicon waveguide arms generates peaks or dips at the transmission spectrum depending on constructive or destructive interference. The AWG consists of an array of a large number of waveguides with each having a different length. The interference of the propagating light in these waveguides results in a peak or dip in the output spectrum. In general, the RR and WBG are resonating structures, whereas in MZI

and AWGs, physical interferometry occurs. Moreover, the AWGs can be considered as the extended architecture of MZI-based geometry. To meet the requirements of an ideal filter, various designs have been reported based on the aforementioned basic geometries, aiming at engineering the spectra according to the target application as will be described in the next sections.

The abovementioned structures are usually fabricated on standard SOI wafers consisting of silicon substrate, 2–3  $\mu\text{m}$ -thick buried silicon dioxide layer, and finally a 220 nm-thick silicon layer on top. To form the ridge or rib shape with the desired filter architecture, the standard e-beam lithography technique followed by etching for patterning is the most commonly used approach since it offers high resolution as well as accurate fabrication possibilities. In this approach, once the filter specifications are defined and the desired architecture's parameters are known, a photoresist (e.g., PMMA, HSQ) is spin coated on top of the SOI platform.<sup>[40,41]</sup> Next, the e-beam lithography exposes the photoresists according to the desired architecture in which to achieve the desired resolution, different parameters of e-beam like beam current, exposure dose, and acceleration voltage can be controlled. After the development of the photoresists through the appropriate solution, finally, the desired architecture was accomplished using a commonly used technique like inductively coupled plasma dry etching.<sup>[42,43]</sup> To protect the different filter architectures, a layer of  $\text{SiO}_2$  having a thickness of around 2  $\mu\text{m}$  is deposited through plasma-enhanced chemical vapor deposition.

In addition to the fabrication steps, before going into the detailed description of different filters and their applications, it is important to mention the basic readout technique in silicon-based filter architectures. In this setup, the silicon filter architectures are coupled with a laser source at the input and a photodiode or an optical spectrum analyzer at the output. The in-and-out light coupling to the silicon-based filter architecture is a critical issue as the strongly filled confinement causes a large field mismatch with the optical fibers. Two common techniques to couple light are in-plane butt coupling and off-plane grating coupling.<sup>[44,45]</sup> In in-plane light coupling, the fiber is placed at the chip facet aligned horizontally with the silicon waveguide. The problem of large field mismatch is addressed through an inverse tapered waveguide or fiber lens tip. In this configuration, it is a must to have a properly cleaved and polished facet to reduce the coupling losses. In off-chip coupling, the fiber is placed on top of a diffractive grating structure. Thanks to the presence of grating, the off-plane wave vector shifts to the in-plane wave vector and excites the guided mode efficiently through a spot size converter usually realized with curved grating, making the entire structure compact. Apart from these two, in hybrid integration, the modal field matching with materials like InP, GaAs relies on waveguide tapering for efficient readout.<sup>[46]</sup>

### 3. Simulation Approaches

The development of high-performance optical filters needs accurate modeling aiming at tailoring their performance. The design benefits from the development of computer-aided modeling and design software, that pave the way to critical insights into the

device under study or the evaluation of new device concepts. For a proper device design, an electromagnetic model that can substantially reduce the computational time as well as memory requirement while maintaining as much as accuracy possible is highly desirable. Four major families of numerical methods can be identified as suitable for electromagnetic simulations of optical filters, such as the beam propagation method (BPM), eigenmode expansion (EME) method, finite difference time domain (FDTD), and finite-element method (FEM). Each approach is best suited for particular cases of study and shows trade-offs, in terms of speed, memory, rigorousness, dispersion, nonlinearities, and so on. All features of the aforementioned approaches are summarized in Table 1, by taking into account the computational speed, the request in terms of memory, the robustness, the capability to take into account reflections, nonlinearities, dispersion, and the approach to sketch the device under test. Moreover, to help the reader to drive the choice of the best simulation approach, a score has been given to the suitability of the aforementioned methods for the simulations of RRs, Bragg gratings, AWG, and MZI, by taking mainly into account speed, memory, and robustness. However, a rigorous suggestion cannot be provided since the approach choice depends also on the target application.

The BPM approximates the wave equation for monochromatic waves by decomposing a mode into a superposition of plane waves, each travelling in a different direction.<sup>[47]</sup> This approach ensures to solve the resulting equations numerically. Two variants have been proposed, Fourier Transform (FT-BPM) and finite difference (FD-BPM).<sup>[48,49]</sup> The BPM was first introduced in the 1970s by Feit and Fleck<sup>[50]</sup> and its simplest form of BPM assumes the electric field as a vector value, also neglecting the polarization of light and assuming that the propagation occurs just in a particular direction (paraxial method). Moreover, the BPM was derived from the slowly varying envelope approximation<sup>[47]</sup> that assumes that the envelope of a forward-travelling wave pulse varies slowly in time and space with respect to the period or wavelength. In the 1990s, the BPM has been successfully modified to take into account the TE and TM polarizations.<sup>[51]</sup> In practice, the approach is usually used in a 2D domain, neglecting the dependence of the field in the transversal direction. From a numerical point of view, the propagating electric field is calculated for each plane along the propagating direction, that is,  $z$ . The distribution in each  $z$  plane is used as the input field to evaluate the field distribution in the next plane. This approach reduces the computational complexity of several problems, also speeding up the computational calculations. However, the speed and requested memory are strictly correlated to the device under the test area. The main limitations of the model are strictly correlated to the nature of the algorithm. In particular, the slowly varying envelope approximation limits the index contrast  $\Delta n$ . Moreover, the method is intrinsically monodirectional and it is not very rigorous for the simulation of devices where the phase variation is critical, such as the MMI. To relax these limitations, several BPM extensions have been proposed in the literature, such as vectorial BPM (electric field is assumed as a vector),<sup>[52]</sup> wide-angle BPM (reduction of the paraxial limitations),<sup>[53]</sup> and bidirectional BPM (overcome the monodirectionality by considering multiple interfaces and reflections).<sup>[54]</sup>

The EME is a fully vectorial bidirectional method in which the electric and magnetic field components can be written as a sum of local eigenmodes.<sup>[55,56]</sup> Next, the analysis is carried by following the continuity equation of the electric and magnetic field associated with the local eigenmodes. The EM behavior of any components could be expressed in terms of a scattering matrix that relates entering and exiting modes. Thanks also to an intrinsic bidirectionality,<sup>[57]</sup> EME allows efficient and fast modeling of periodic structures, by calculating the S-matrix of just one period and then repeating it. It allows also to simulate very large circuits by dividing them into multiple parts, calculating the related S-matrix and multiplying them. Moreover, since it is a fully vectorial algorithm with a rigorous solution of Maxwell's equations, all polarizations, all  $\Delta n$  and wide angles can be simulated with high accuracy. However, EME is inappropriate to evaluate the EM behavior of structures that continually change in cross section, as taper, and devices with a very large cross section, that impact the computational time scaling as the cross section. All the modes need to be recomputed for every change of the cross section with a strong impact on the computational efficiency.

Moreover, nonlinear structures are difficult to simulate, since only small nonlinearities ensure the convergence of the method.

The FDTD method estimates the device performance by discretization of the Maxwell equation in the time domain using the central difference technique without using any approximation with a second-order, stable, staggered-grid approach for electric and magnetic fields.<sup>[58]</sup> The FDTD has been proposed in 1966 by Kane Yee.<sup>[59]</sup> FDTD is the most widely used approach for Maxwell's equations, with very high accuracy, and even if  $\Delta n$  is large, there are several reflecting interfaces, the material is nonlinear, or the device shows wide angles. All these benefits come at the price of slow speed and huge memory, which both scale as the device volume. One of the main accuracy limitations is the so-called numerical dispersion error related to the approximation of the dispersion relations of Maxwell's equations caused by the propagation of a wave in a discrete grid. Therefore, the error accumulates over time, resulting in very time-consuming simulations. Moreover, another limitation is related to the regular rectangular grid that forces the same resolution along the whole device. To overcome it, some tools use subgridding to

**Table 2.** Comparison of BPM, EME, FDTD, and FEM with a score/10 about their suitability to simulate photonic filters (A: area, c-s: cross-section, V: volume).

	BPM	EME	FDTD	FEM
Speed	Scales linearly with A.	Poorly scales with c-s A. Very efficient for long structures only if the c-s changes slowly.  PhC simulations scale with the number of periods.	Scales as V (a bit more efficient than FEM).	Scales as V.
Memory	Scales linearly with A.	Scales with c-s $A^2$ – $A^3$ . Efficient for long structures.	Scales as V (a bit more efficient than FEM).	Scales as V.
Reflections	Inherently not possible. Bidirectional expansion has been proposed at the expense of low speed.	Easy and stable.	Easy and stable.	Easy and stable.
Rigorousness	Best with low $\Delta n$ .	Accurate even with high $\Delta n$ .	Very accurate even with $\Delta n$ .	Very accurate even with $\Delta n$ .
Nonlinearities	Easy to implement.	Very difficult to implement.	Easy to implement.	Easy to implement.
Dispersion	Easy to implement.	Easy to implement.	Exact fit to the spectrum over a wide wavelength is difficult.	Easy to implement.
Geometry	Easy modelling of devices with complex shapes.	Different structure discretization could be used in different c-s.	Arbitrary geometries by using fine rectangular grids	Variable shapes, like triangles, tetrahedrons, and prisms, can discretize different structures.
Main software	<ul style="list-style-type: none"> <li>• Synopsys BeamPROP<sup>[274]</sup></li> <li>• OptiwaveOptiBPM<sup>[275]</sup></li> </ul>	<ul style="list-style-type: none"> <li>• PhotonDesign FIMMPROP<sup>[276]</sup></li> <li>• Ansys Lumerical FEEM<sup>[277]</sup></li> <li>• CAMFR<sup>[278]</sup></li> </ul>	<ul style="list-style-type: none"> <li>• Meep<sup>[279]</sup></li> <li>• gprMax<sup>[280]</sup></li> <li>• OpenEms<sup>[281]</sup></li> <li>• Synopsys RSoft<sup>[282]</sup></li> <li>• Ansys Lumerical FDTD<sup>[283]</sup></li> <li>• PhotonDesignOmniSim<sup>[284]</sup></li> <li>• PhotonDesignCrystalWave<sup>[285]</sup></li> </ul>	<ul style="list-style-type: none"> <li>• FEniCS<sup>[286]</sup></li> <li>• Elmer FEM<sup>[287]</sup></li> <li>• FreeFEM<sup>[288]</sup></li> <li>• Comsol Multiphysics<sup>[289]</sup></li> </ul>
Simulation method suitability of				
RRs	2/10	9/10	8/10	7/10
BGs	2/10	8/10	8/10	4/10
MZIs	7/10	6/10	8/10	9/10
AWGs	10/10	0/10	8/10	2/10

thicken the resolution in certain areas. Moreover, since the simulation of circular or spherical objects struggles, the pseudospectral time domain method has been proposed by subdividing the structure of the subdomain with a uniform index with also a varying grid size.<sup>[60]</sup>

The FEM was first proposed in 1940<sup>[61]</sup> and its robustness and versatility have pushed its use in several fields of science and engineering. In the photonics field, the FEM technique approximates the time-harmonic Maxwell's equations in partial differential equations (PDEs). The approach relies on splitting the geometry into multiple meshing elements, with different shapes, and numerically solving the PDEs in two or three space variables.<sup>[62]</sup> In summary, the method is based on weak integrals of the product of PDE by test functions and integration-by-parts arguments. The operation is referable to sparse linear algebra problems by restricting the variables and target functions into discrete spaces. The discretization of the volume could represent at the same time an advantage or disadvantage. In particular, the volumetric discretization allows to easily consider anisotropic material, but at the same time, for a homogeneous medium, the discretization represents a simulation speed limitation.

For the simulation of an RR, the BPM technique is fundamentally unable to evaluate the EM response due to its paraxial approximation. Although BPM expansion approaches have been proposed to overcome this limitation, the  $\Delta n$  constraint limits the available technology platforms. EME is the best approach for the RR simulation because it provides quite accurate results with a very low computation time. An alternative to EME is the FDTD or FEM which shows strengths and weaknesses. In particular, the time domain nature of FDTD leads to a long time to reach a precise steady state, while the mesh for FEM could represent a hurdle, in particular for large RRs with high-aspect-ratio waveguides.

EME is capable of simulating 2D/3D photonic crystals in an efficient manner although with a slight mismatch with respect to experimental results,<sup>[63]</sup> by repeating the S-matrixes along the whole structure with a significant saving of computational time. However, this performance is restricted to straight waveguide-based Bragg gratings. The nature of BPM clashes with the simulation of Bragg grating, due to the incapability to take into account the bidirectionality. Bidirectional expansion BPM could be useful at the expense of large computational time. FDTD can predict the most accurate results at the cost of large computational time, although more efficient with respect to FEM that requests a very huge amount of mesh elements. **Table 2** illustrates a comparison between the overmentioned methods including a score about their suitability to different filter topology simulations.

For both accurate and fast simulation of MZI, the BPM is usable although the input/output couplers should show small divergence and small  $\Delta n$ , for example, silicon technology is unfeasible. EME can predict accurate results with low computational time only if tapers are not included in the design. FDTD could be the best approach when, for example, MMIs are used as couplers. However, the simulations take a long time caused by a uniform grid that could be thickened at the couplers and wide at the straight arms. In our opinion, FEM is the best suitable approach to evaluate the EM response of MZI since its

multiphysics nature could be helpful to study the reconfigurability, preserving the accuracy with a relatively low computational time.

For the simulation of AWG, the presence of several waveguide tapers limits the use of the EME solver. Instead, the use of a FEM solver is not recommended because the setting of curved mesh is very challenging, requiring a huge designer effort and time. Several papers reported in the literature compare the performance of the FDTD and wide-angle BPM methods, in terms of the accuracy of the results with respect to measurements.<sup>[64]</sup> In particular, the best agreement between simulated and measured results has been achieved using BPM-based software, with a significant saving of time.

## 4. Reconfigurability

Filter reconfigurability can be realized by altering the modal effective index of the guided mode. The two most common techniques are based on the TO<sup>[65]</sup> and the EO effect.<sup>[66]</sup>

The TO effect relies on the TOC of the waveguide material as well as its thermal conductivity. Silicon is a material particularly suitable for the TO effect due to its high positive TOC of  $1.8 \times 10^{-4} \text{ }^\circ\text{C}^{-1}$  as well as high heat conductivity ( $149 \text{ W mK}^{-1}$ ).<sup>[13,67–69]</sup> As a result, in the past few decades, various tunable silicon photonic filters based on the TO effect have been reported, with low power consumption and reconfiguration speed (of the order of  $\mu\text{s}$ ). The associated losses restrict the tunability range.

The basic configuration consists of a metal heater fed by electric current, placed in proximity to the waveguide core. The cross-sectional view is shown in **Figure 6a,b**. The heat generated in the metal, following Joule heating, induces a change in the waveguide refractive index as  $n = n_o + dn/dT \times \Delta T$  where  $dn/dT$  denotes TOC and  $n_o$  is the refractive index at room temperature.<sup>[67]</sup> This phenomenon modifies the modal effective index and thus the resonance wavelength. The tuning power efficiency can be defined as the power required to cause a phase shift of  $\pi$  which can be expressed as<sup>[70,71]</sup>

$$P_\pi = G \times A \times \Delta T_\pi \quad (5)$$

where  $G$  is the thermal conductance between the waveguide and surroundings,  $A$  is the area of the heater, and  $\Delta T_\pi$  is the change in temperature for  $\pi$  phase shift. Another important quantity is the response time  $\tau$  normally defined as 10–90% rising time and or 90–10% falling time in response to a square pulse of the electrical signal. The response time can be expressed as<sup>[70,71]</sup>

$$\tau \approx H / (G \times A) \quad (6)$$

where  $H$  is the heat capacity. Here, it is important to note that the separation between the metal layer and waveguide ( $t_s$ ) should be sufficiently thick to avoid absorption loss due to the metal. However, thick upper cladding also increases the surface area and thus reduces the tuning efficiency. Therefore, a trade-off must be made when choosing the separation between the metal layer and the waveguide core. The configuration in **Figure 6a** shows a common tuning efficiency below  $0.2 \text{ nm mW}^{-1}$  with a response time of the order of  $10 \mu\text{s}$ . **Figure 6c** shows a 3D view

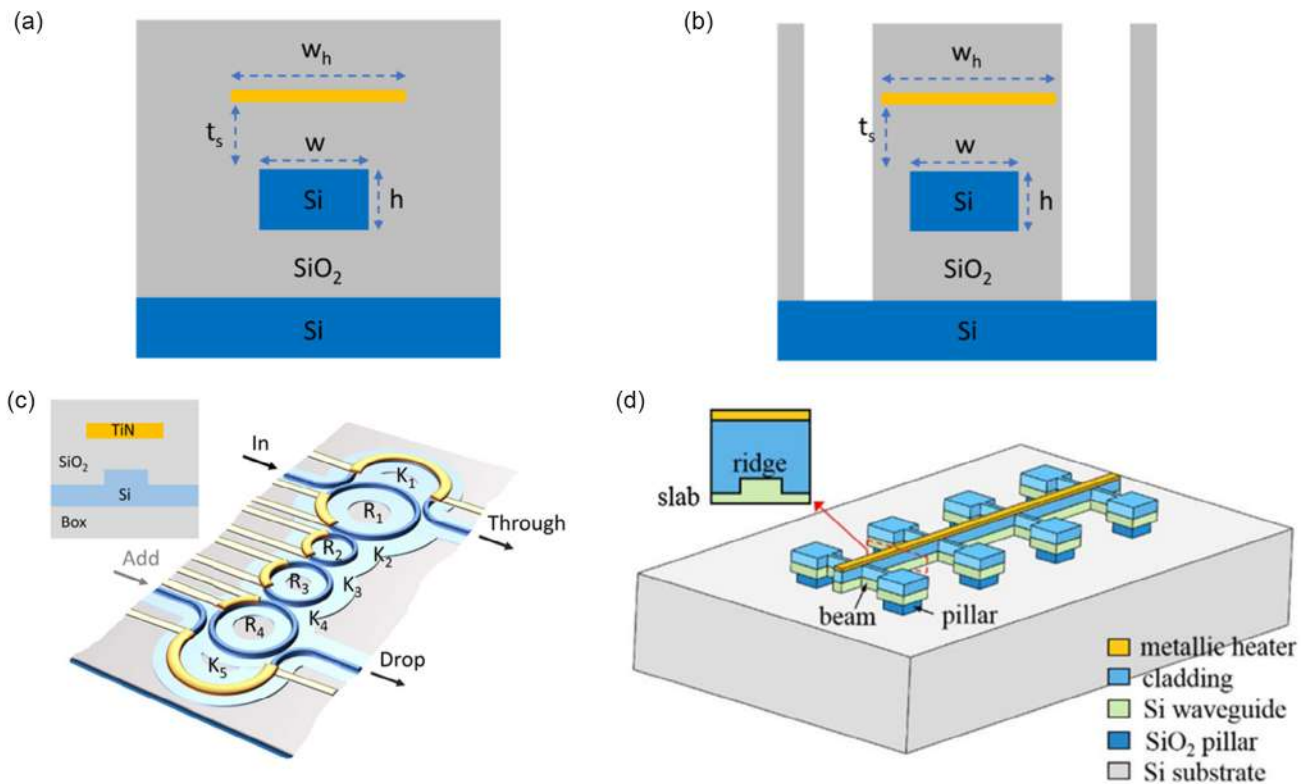


**Figure 6.** a) Commonly used cross sections of TO tuning with metallic heater geometry of Si photonic filters and b) cross section with air trenches to increase the tuning efficiency. c) Schematic view of metallic heater placed over RRs. Reproduced with permission.<sup>[72]</sup> Copyright 2021, Nature Communications. d) Suspended structure with a metallic heater to realize low-power consumption. Reproduced with permission.<sup>[82]</sup> Copyright 2020, Optical and Quantum Electronics.

of a fourth-order tunable MRR filter integrated with a metallic heater of TiN.<sup>[72]</sup> The TiN heater is placed 700 nm above the silicon core, ensuring low-loss performance. In this structure, both the resonance wavelength and coupling coefficient have been tuned with TiN heaters placed on top of each resonator section and two coupling sections K1 and K5. Following a similar principle, different tunable filters have been realized over the years. For example, a tuning efficiency of  $0.16 \text{ nm mW}^{-1}$  has been achieved by a recently reported Bragg grating-based structure,<sup>[73]</sup>  $0.17 \text{ nm mW}^{-1}$  for RR-based structure,<sup>[74]</sup> and  $0.07 \text{ nm mW}^{-1}$  for long-period gratings.<sup>[67,75]</sup> It is to be noted that the metal layer like TiN is deposited on top of the SiO<sub>2</sub> upper cladding up to the desired thickness and next the lift-off technique is used to form the pattern of the metallic heater.

Therefore, large values of power are needed to enlarge the tuning range of the filter. To reduce power consumption, several approaches have been investigated, such as optimizing the surface area of the metallic heater or creating air trenches beside the waveguide core,<sup>[76–78]</sup> the bottom of the core,<sup>[71,79]</sup> or both.<sup>[76,80,81]</sup>

The cross section of a waveguide structure with air trenches is shown in Figure 6b. Since the air trenches prevent heat leakage in the vertical and horizontal direction, this provides thermal isolation and thus significantly reduces power consumption. A 3D schematic view of a silicon photonic waveguide with air trenches is shown in Figure 6d.<sup>[81]</sup> The air trenches are present in both vertical and horizontal directions, making the structure a

suspended waveguide. This can significantly improve the tuning efficiency. For example, in ref. [75], the Authors have experimentally demonstrated such suspended architecture with a racetrack resonator. The tuning efficiency is found to be as high as  $4.8 \text{ nm mW}^{-1}$  at the cost of a higher response time of 170  $\mu\text{s}$ . This can be attributed to the fact that the response time is inversely proportional to the air gap. Therefore, it is challenging to simultaneously reduce the power consumption and increase the tuning speed. One way to overcome this problem is to use graphene instead of metal as the heater. Due to its remarkable electrical and optical properties, such as high heat conductivity, good transparency over a broad wavelength range, CMOS compatibility, and high damage threshold, recently graphene nanolayer has been used as an efficient heater to provide fast reconfigurability to devices.<sup>[82–84]</sup> In 2014, for the first time, graphene was demonstrated as the nanoheater in which it is placed in direct contact with the silicon core, greatly enhancing the tuning efficiency as well as the tuning speed.<sup>[85]</sup> Unlike metal, graphene also introduces low excess loss as it has much lower absorption losses compared to metals; therefore, it can be placed in direct contact with the silicon core. As a result, various reconfigurable silicon photonic devices with graphene nanoheaters have been reported.<sup>[86,87]</sup> For example, a tuning efficiency of  $1.5 \text{ nm mW}^{-1}$  with a possibility of a further improvement toward  $3.75 \text{ nm mW}^{-1}$  has been demonstrated in ref. [86], whereas the 10–90% rising time is found to be only 1.11  $\mu\text{s}$ . Moreover, a

response time of  $0.8 \mu\text{s}$  has been reported in ref. [88], which is much lower than the metallic microheater.

EO tuning is another promising and popular technique to reconfigure silicon photonic devices. In this configuration, a silicon rib waveguide is doped with P- and N-type impurities, as shown in **Figure 7**. By applying a biasing voltage to the p-n junction it is possible to locally change the refractive index of the core by plasma dispersion effect.<sup>[14,85,86]</sup> The P+- and N+-doped silicon can be realized through the implantation of boron and phosphorus respectively doping with required concentration deciding the refractive index. The refractive index of the core changes with the carrier injection or depletion in response to the biasing voltage. However, in addition to the change in the refractive index, it also introduces extra loss in the waveguide. Soref and Bennett quantified the changes in the real and imaginary parts of the refractive indices in the C-band, which can be expressed<sup>[85,87,88]</sup> as

$$\begin{aligned} \Delta n &= -8.8 \times 10^{-22} \Delta N - 8.5 \times 10^{-18} \times \Delta P^{0.8} \\ \Delta \alpha &= 8.5 \times 10^{-18} \times \Delta N + 6 \times 10^{-18} \times \Delta P \end{aligned} \quad (7)$$

where  $\Delta N$  and  $\Delta P$  refer to changes in electron and hole concentration respectively. The cross-sectional view of one of the most popular configurations for the EO effect is shown in **Figure 7a**, where the two edges of a rib waveguide are doped with p-type and n-type impurities. An MRR architecture following this principle is shown in **Figure 7c**. The thickness of the strip part is typically considered to be  $50 \text{ nm}$ . Since the thickness is well below the operating wavelength of around  $1.55 \mu\text{m}$ , the rib waveguide

effectively behaves like a ridge waveguide. The two doped sections are considered to be well away from the core ( $\approx 1 \mu\text{m}$ ) to minimize the modal overlap with the doped section which helps to reduce the absorption loss.<sup>[83]</sup> In some configurations, to achieve higher refractive index modulation, the waveguide section is also doped with a lower concentration in addition to the heavy doping at the two edges, as shown in **Figure 7b**. In such cases, the width of the p-doped section is usually taken to be higher than the n-doped section.<sup>[84]</sup> This ensures relatively low absorption loss as the contribution in loss coming from the p-doped section is lower than the n-doped section (see Equation (7)). The EO tuning mechanism shows good efficiency. For example, in ref. [89] a Bragg grating-based structure (see **Figure 7d**) provides a tuning efficiency of  $1.35$  and  $0.52 \text{ pm V}^{-1}$  in forward and reverse bias respectively. The EO effect also provides a quicker time response ( $\approx \text{ns}$ ) than the TO effect ( $\approx \mu\text{s}$ ). However, the tuning range of wavelength is usually lower than the TO effect. The most performing results of the investigated tuning mechanisms are reported in **Table 3**.

## 5. Applications

### 5.1. Optical Communications

Silicon photonic filters have been extensively studied over the years in both coarse and dense wavelength division multiplexing (CWDM and DWDM) and demultiplexing networks.<sup>[31]</sup> Passive or reconfigurable WDM channels and interconnects are the

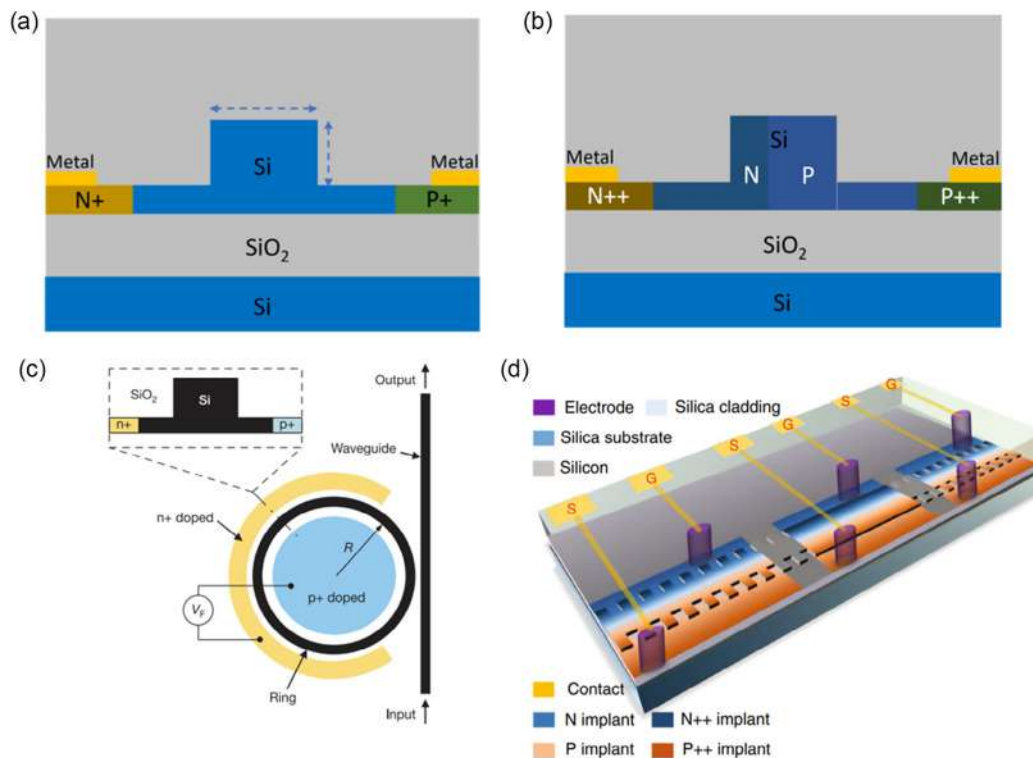


**Figure 7.** Most commonly used EO tuning configurations in silicon waveguides with plasma dispersion effect with a) doping in the edges only and b) doping in the silicon core and heavy doping at the edges. Schematics of a filter with EO tuning in c) RR. Reproduced with permission.<sup>[83]</sup> Copyright 2005, Nature. d) WBG. Reproduced with permission.<sup>[84]</sup> Copyright 2018, Nature Communications.

**Table 3.** Comparison in terms of efficiency and tuning speed, of the most commonly used tuning mechanisms.

Tuning Mechanism	Efficiency	Response time (Rise/Fall)	References
TO with metallic heater	4.8 nm mW <sup>-1</sup>	170/170 μs	[76]
	–	3.7/3.44 μs	[69]
	0.07 nm mW <sup>-1</sup>	9.94/9.75 μs	[67]
TO with graphene nanoheater	0.24 nm mW <sup>-1</sup>	1.2/3.6 μs	[290]
	1.5 nm mW <sup>-1</sup>	1.11/1.47 μs	[291]
	0.11 nm mW <sup>-1</sup>	0.75/0.8 μs	[292]
EO with plasma dispersion	20.17 GHz V <sup>-1</sup>	≈1 ns	[66]
	15.6 μm μW <sup>-1</sup>	–	[84]
	0.15 nm V <sup>-1</sup>	10 ns	[83]

backbone for telecommunication, 5 G backhaul networks, intra-, inter-datacenter connection, etc. Si-based filters operating in different optical bands, such as O-band (1260–1360 nm),<sup>[90,91]</sup> C-band (1530–1565 nm),<sup>[92,93]</sup> L-band (1565–1625 nm),<sup>[94]</sup> and recently developed 2 μm band,<sup>[95]</sup> have been extensively studied by several research groups and companies. The availability of thulium-doped fiber amplifiers which show a broader bandwidth

(1700–2100 nm) as compared to Er-doped fiber amplifiers (1480–1610 nm) has gained significant interest in developing different telecommunication components including filters in the 2 μm wavelength window in recent time.<sup>[96]</sup> This section provides a brief review of the state-of-the-art development of WDM networks with different Si filter architectures.

### 5.1.1. Mach–Zehnder Interferometer (MZI)

For the single-stage MZI, the output spectrum shows a sinusoidal-like behavior, as in Figure 5c. However, multiple MZIs can be cascaded to form a flat top spectral response with sharp roll-off by carefully engineering the coupling coefficient of each coupler. Horst et al. reported a 1 × 8 channel WDM based on binary tree-like cascaded MZI filters.<sup>[97]</sup> It comprises three-stage structures in which each stage consists of a specific number of delay lines and couplers having optimized coupling coefficients, as shown in Figure 8a. A flat top response with an ER of 15 dB, channel spacing of 3.2 nm, and IL below 1.6 dB around a central wavelength of 1.49 μm has been demonstrated (Figure 8b). Utilizing the cascaded MZI structure, various CWDM networks in the Si technology platform have been reported.<sup>[95,98]</sup> Xu et al. reported a four-channel WDM filter using a cascaded MZI suitable for CWDM application<sup>[99]</sup> with a bent

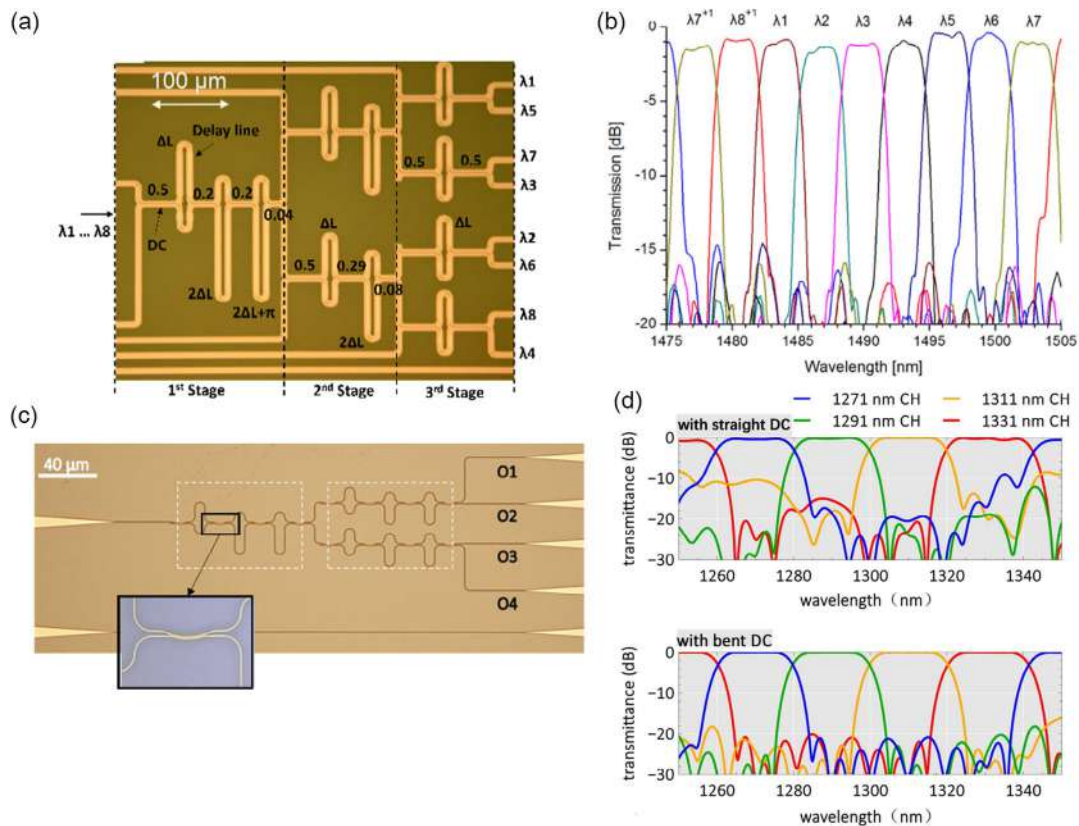


**Figure 8.** a) Micrograph of the cascaded MZI with optimized coupling coefficients and delay length. Reproduced with permission.<sup>[97]</sup> Copyright 2013, Optics Express. b) The calculated transmission spectra of the eight-channel cascaded structure. Reproduced with permission.<sup>[97]</sup> Copyright 2013, Optics Express. c) Cascaded 4-channel MZI structure with bent DC. The inset image shows the enlarged view of the bent DC. Reproduced with permission.<sup>[99]</sup> Copyright 2018, IEEE Photonics Technology Letters. d) The spectrum of the 4-channel WDM with straight DC (top one) and bent DC (bottom one). Reproduced with permission.<sup>[99]</sup> Copyright 2018, IEEE Photonics Technology Letters.

DC (see Figure 8c). It has been reported that a bent DC instead of a straight DC leads to a significant improvement in the crosstalk between channels due to a stronger coupling and thus a larger 3 dB bandwidth of the power splitter/combiner. The crosstalk is found to be around  $-10$  dB with a straight DC whereas it is less than  $-20$  dB with a bent DC having a 3-dB bandwidth of 19 nm (Figure 8d).

Here it is to note that due to high-index contrast a small variation in the waveguide's width or thickness causes a large-scale variation in guided mode property. As a result, the sidewall roughness that originated during the lithography makes it challenging to hold the channel wavelengths at specific positions. To overcome this effect, Han et al. reported a thermal tuning compensation technique to stabilize the channel wavelengths at specific positions.<sup>[100]</sup> In another approach, a multimode waveguide has been used to reduce the sensitivity to fabrication errors, thanks to its wide dimension.<sup>[101]</sup>

Recently, Yen et al. demonstrated a fabrication-tolerant MZI-based four-channel filter by adjusting the variation of the

effective index with respect to the waveguide's width.<sup>[102]</sup> This has been achieved by controlling the width and the lengths of two arms for each MZI, as shown in Figure 9a. The proposed design shows an average spectral shift of  $0.487 \pm 0.878$  nm from the defined wavelength grid whereas the regular MZI shows an average shift of  $15.398 \pm 2.5$  nm (see Figure 9b), reflecting a significant improvement. To mitigate the effect of fabrication imperfection, a dispersion-engineered MZI structure has been also reported in the O-band of optical communications.<sup>[90]</sup>

Another issue is the polarization sensitivity of the structures. The random polarization of the optical fiber exiting the MZI channel drop filters can cause a significant shift in the central wavelength due to the large difference in TE and TM mode's effective indices. A square cross section can be used to overcome this problem but at the cost of fabrication tolerances. Xu et al. reported a four-channel CWDM structure operating in the O-band in which polarization insensitivity has been achieved utilizing a polarization-insensitive bent DC and a polarization

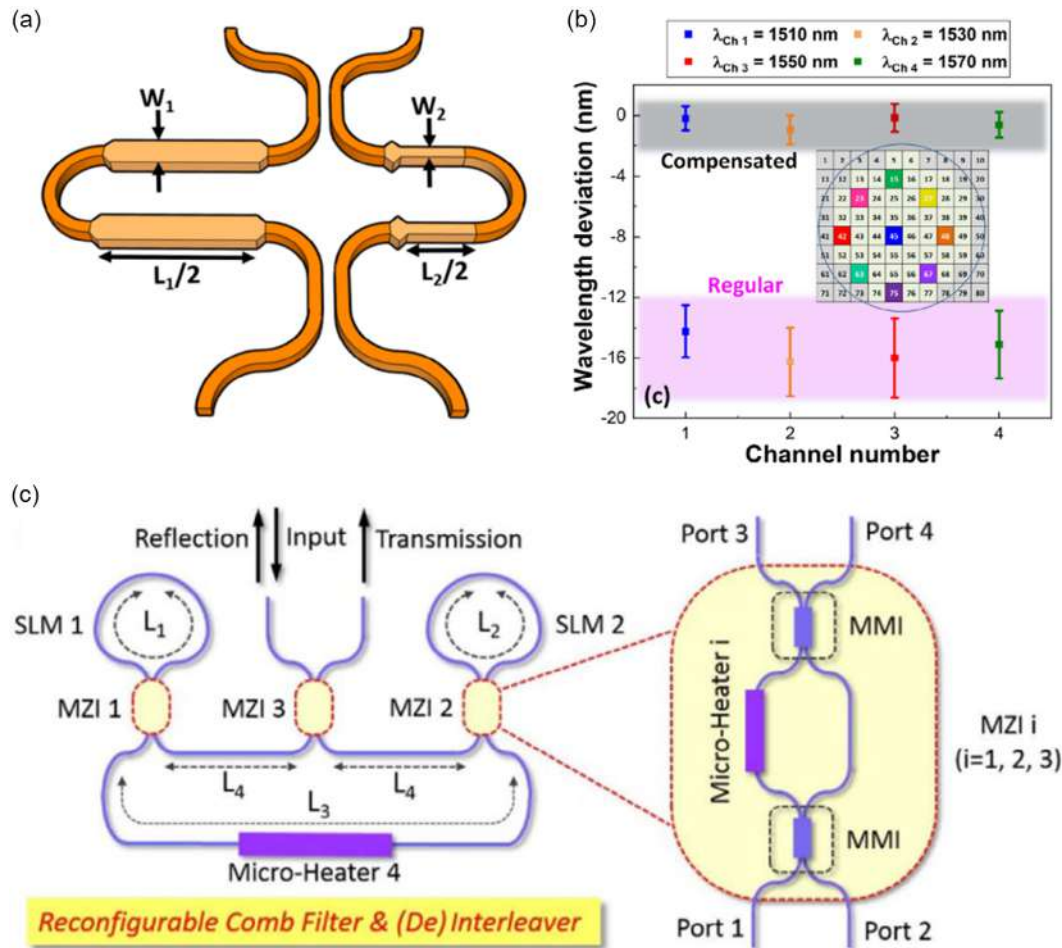


**Figure 9.** a) Schematics of the fabrication-tolerant MZI. Reproduced with permission.<sup>[102]</sup> Copyright 2021, Journal of Lightwave Technology. b) The statistic wavelength deviation for the fabrication tolerant and a regular four-channel CWDM structure with MZI. The inset image shows the wafer location with nine highlighted regions corresponding to nine devices under test. Reproduced with permission.<sup>[102]</sup> Copyright 2021, Journal of Lightwave Technology. c) Schematic diagram of a reconfigurable comb filter and formation of (de)interleaver with SLMs and tunable MZIs. Reproduced with permission.<sup>[106]</sup> Copyright 2018, OAPA. The inset shows the MZI structure with the microheater placed in one arm and the MMI coupler.

rotator.<sup>[103]</sup> The 3 dB bandwidth is found to be 17 nm with polarization-dependent losses <0.5 dB for all the channels. It is to be noted that nanometer-scale variation in the waveguide's dimensions makes it extremely difficult to hold the different channels placed closely, a hindrance in its application toward DWDM. To avoid this issue, a trimmer or a tuner should be used but it would be expensive and would waste a lot of power, especially for a large number of channels. Munk et al. successfully demonstrated an eight-channel DWDM filter by combining seven unbalanced MZIs in a cascaded tree structure with a nested MRR structure.<sup>[93]</sup>

The postfabrication trimming of phase delays in different arms was carried out by local illumination of a photo-sensitive upper cladding made of chalcogenide glass. The proposed structure produces a low crosstalk of <-22 dB and a channel spacing of only 17 GHz.

To meet the growing demand for data traffic, optical interleavers and optical comb filters became essential components in WDM systems. The dynamic tunability of such filters in terms of the central wavelength, bandwidth, and switching between comb filter and interleaver operation is highly desirable for a flexible WDM system. For example, Song et al. reported an MZI-based interleaver structure assisted by RR, where the crosstalk has been improved from 6 to 17 dB using thermo-optic fine-tuning.<sup>[104]</sup> Jiang et al. reported a bandwidth and central wavelength tunable optical comb filter with an MZI coupler-assisted Sagnac loop mirror (SLM).<sup>[105]</sup> The proposed structure consists of two cascaded SLMs with an MZI coupler. To control the phase shift and reflectivity of the SLMs, microheaters are placed on the top of both arms of each MZI. By thermally controlling both the arms in common and differential modes, tuning in terms of central wavelength and bandwidth has been achieved. The proposed comb filter consists of 93 comb lines in the C-band of telecommunication in which the central wavelength has been tuned with an efficiency of 0.019 nm mW<sup>-1</sup> over a wavelength range of ≈0.462 nm. A continuous bandwidth tuning has been reported from 5.88 to 24.89 GHz with a differential heating power, spanning over 0.53 from 0 mW. Zhou et al. reported a reconfigurable filter incorporating both comb filtering and interleaving functions based on SLM architecture,<sup>[106]</sup> as presented in Figure 9c. Three MZI couplers have been used with a metallic heater placed on top of one interfering arm of each MZI to realize the reconfigurability through thermal tuning. By properly adjusting the three microheaters placed on MZIs and the fourth microheater placed in the cavity of large SLMs, the reconfigurability and switching between comb filter and (de)interleaver has been accomplished. The FSR is found to be 0.22 and 0.45 nm for the comb filter and (de)interleaver with a respective 3 dB bandwidth of 0.032 and 0.225 nm. The tuning efficiency for the comb filter and (de)interleaver is found to be 0.0224 and 0.0193 nm mW<sup>-1</sup>, respectively.

In summary, this subsection provides an organized review of MZI-based filters including a discussion about how to realize flat-top response through cascaded architectures and the strategies for attaining fabrication-tolerant and/or polarization-insensitive structures. The realization of a switching section between comb filters and interleavers by merging MZIs with RRs has been also discussed.

### 5.1.2. Microring Resonator (MRR)

The spectrum of an MRR has a Lorentzian shape, as shown in Figure 5a, that limits possible applications. However, its small footprint, structural simplicity, and scalability give it an edge over other silicon photonic architectures. To guarantee a box-like response, multiple rings can be cascaded with optimal coupling coefficients. Little et al. reported a coupled RR design that provided a flat top response with sharp roll-off.<sup>[107]</sup>

A more box-like response can be achieved with an increase in coupled MRRs. Following this principle, several higher-order RRs are being reported. For example, Dong et al. experimentally demonstrated a fifth-order MRR with an ER of 50 dB and stiff roll-off in which a metallic heater was placed on top of each MRR, to tune the spectral response, as shown in Figure 10a.<sup>[108]</sup> The ER has been significantly improved for the fifth-order MRR (50 dB) as compared to the second-order MRR (30 dB) (Figure 10b). A third-order MRR, having an intraband ripple of 0.65 dB with an ER of 40 dB, is reported in ref. [109]. For the WDM application, MRR is used in add drop configuration in which two straight waveguides have been used with the coupled ring structure. The multiplexing function has been achieved by adding the input port to the through port.

In MRR-based WDM applications, the number of channels is usually limited by the FSR which is inversely proportional to the ring's circumference. In general, the radius of the rings is taken to be 5–10 μm which provides FSR around 20 nm. Prabhu et al. reported an FSR of 52 nm and a 3 dB bandwidth of 1.6 nm with a ring radius of 1.5 μm.<sup>[110]</sup> In a recent study, the same authors have further improved the FSR to 80.5 nm with the radius scaled down to 1 μm but at the cost of increased 3 dB bandwidth (3.3 nm).<sup>[111]</sup> For these ultracompact MRR structures, the control of the coupling between the ring and the straight waveguide is particularly challenging due to phase mismatch and the excitation of higher-order mode. For small bending radius, the bend DCs can be the best choice over the MMI couplers or straight DCs. Bent DCs bring some unique advantages, such as no excess loss due to mode mismatch at the junction, flexibility in controlling the coupling ratio by choosing the length of the coupling region and maximum FSR within a smaller cavity length. The highest FSR for the MRR is reported to be 93 nm. It consists of an MRR assisted by bent asymmetrical DCs with a submicrometer ring radius of 0.8 μm.<sup>[112]</sup> The 3 dB bandwidth is found to be 0.8 nm. Liu et al. reported a higher-order MRR with the bent DCs in which elliptical rings with both adiabatic radius and width have been used to reduce the propagation loss, and the sharp bending produces an FSR of 37 nm,<sup>[113]</sup> as shown in Figure 10c. Further, an eight-channel WDM based on a second-order MRR has been reported with channel spacing of 3.2 nm, 3 dB bandwidth of 2.6 nm, and ER > 30 dB (see Figure 10d). Using the adiabatic elliptical microring, an all-passive tenth-order MRR structure has been reported, which produces FSR = 37 nm, 3 dB bandwidth = 3 nm, box-like spectrum, and ER = 60 dB.<sup>[114]</sup> Besides reducing the circumference of the ring, the Vernier effect is also used to increase the FSR. For example, in ref. [115], quadruple MRRs with the Vernier effect have been proposed to achieve an FSR of 37.52 nm and channel isolation of 37.2 dB, resulting suitable for DWDM application.

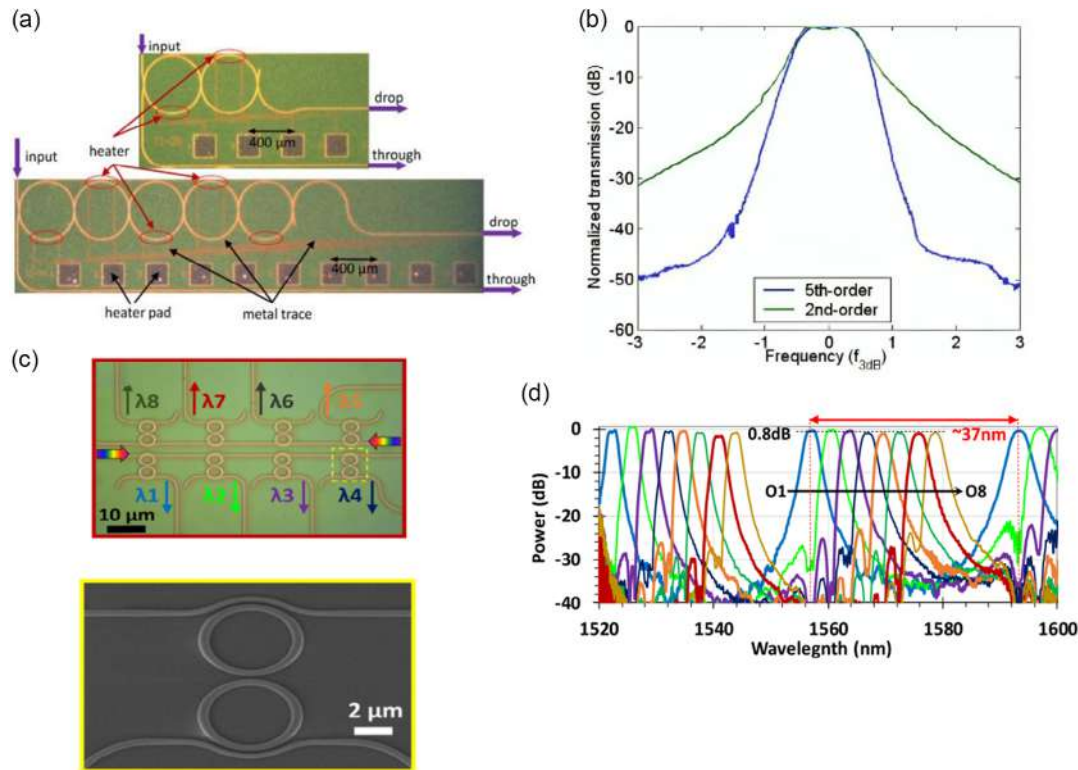


**Figure 10.** a) Schematics of the second-order and fifth-order cascaded RRs and b) corresponding drop port spectrum. Reproduced with permission.<sup>[108]</sup> Copyright 2010, Optics Express. c) Eight-channel second-order RR-based filter for WDM application with bent DC and d) the corresponding drop port spectrum showing an FSR of 37 nm. Reproduced with permission.<sup>[113]</sup> Copyright 2021, Journal of Lightwave Technology.

The high birefringence of the Si waveguide makes the multiple-channel MRR-based WDMs highly polarization sensitive. Therefore, to reduce the crosstalk arising from two different polarizations, it is desirable to engineer the polarization dependency of the filters. Tan et al. reported a TE- and TM-selective MRR-based structure in which the bent DCs and radius of the rings are designed such that the MRR only works for resonances associated with either TE or TM mode.<sup>[116]</sup> The bent DC controls the coupling ratio for two different polarizations whereas the ring radius introduces high propagation loss for the unwanted polarization. This technique successfully depressed the undesired polarization with a high ER. For the TM-type (TE-type) RR, at the drop port, the peak transmission is depressed to be  $< -50$  dB ( $\approx -40$  dB) and at the through port the transmission loss is  $< 0.5$  dB ( $< -0.5$  dB) when TE (TM) mode is input. The high TOC of Si is another source of concern for RR-based WDM systems. Recently, Verma et al. reported a temperature-insensitive RR structure with  $\text{TiO}_2$  as the upper cladding.<sup>[117]</sup> The high negative TOC of  $\text{TiO}_2$  significantly reduces the thermal dependence while maintaining a high FSR (45 nm). Rukerandanga et al. designed a sixth-order silicon-rich nitride RR structure for the DWDM application which is simultaneously insensitive to the polarization of the mode and ambient temperature.<sup>[94]</sup> The insensitivity to both these parameters has been achieved by the careful selection of materials and waveguide dimensions. The bandwidth is found to be only 0.4 nm with an extended FSR of 20 nm.

Tuning the central wavelength over a wide wavelength range is a critical feature for a flexible WDM system. Because of that, various attempts have been made out of which the Vernier effect is found to be particularly promising. With a fourth-order Vernier cascaded RR, Ren et al. reported a widely tunable filter over a range of 32 nm.<sup>[118]</sup> The tuning has been achieved through the TO effect. The proposed structure consists of two cascaded double RRs with different FSRs of 7.8 and 6.5 nm. The proposed cascaded geometry allows thermally isolating the two stages and individual calibration, due to which accurate tuning of each stage without further spectral optimization at each set wavelength has been achieved. The tuning efficiency is found to be  $80.6 \text{ pm mW}^{-1}$  and  $83.4 \text{ nm mW}^{-1}$  for the two stages.

Besides tuning over a wide range, hitless tunability is an important feature in which the selected channel can be dynamically rerouted without perturbing the other channel. Recently, Morichetti et al. reported a polarization-insensitive cascaded RR structure where the central wavelength was turned over a wide wavelength range of 100 nm in a complete hitless fashion with channel isolation  $> 35$  dB.<sup>[72]</sup> The schematic of the proposed structure with the TiN microheater and both with heater and p-i-n junction has been shown in Figure 11a,b, respectively, with corresponding microscopic images of the fabricated devices. The wide-wavelength range operation has been realized by the noninteger Vernier effect between the FSR of different RRs. The radius of the rings is taken to be different to cancel the periodicity of the filter response and realize FSR-free operation.

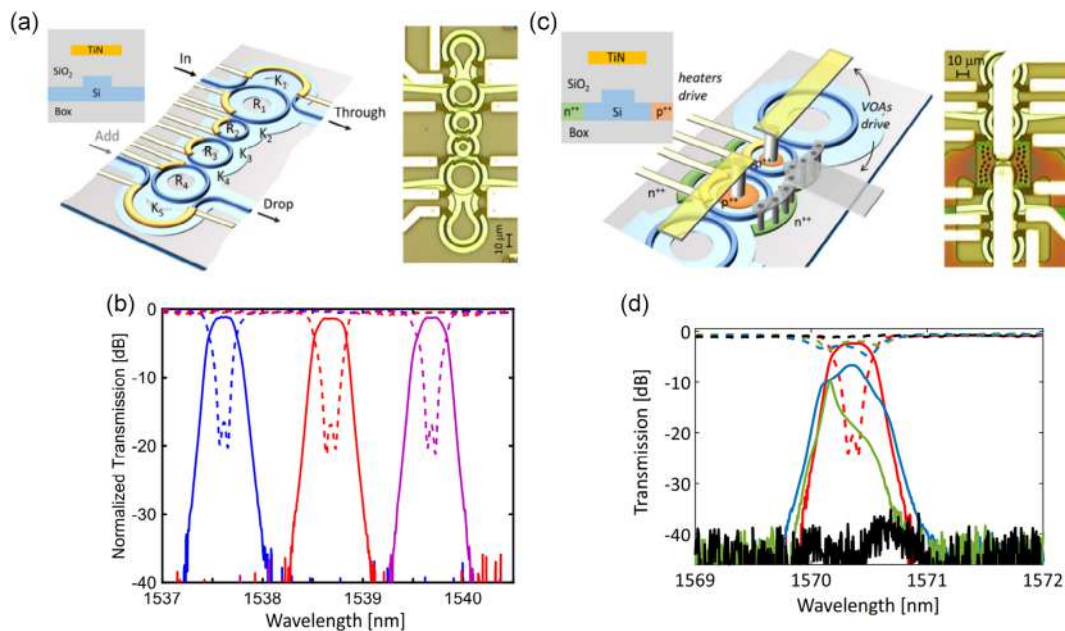


**Figure 11.** a) Schematics of the fourth-order MRR with MZI coupler and TiN microheater placed 700 nm above the waveguide and the corresponding microscopic picture of the fabricated device. b) Drop port and through port spectrum of the cascaded MRR structure tuned to three different channels having 3-dB bandwidth 40 GHz. c) The coupled MRR structure with p–i–n junctions acts as variable optical attenuators in addition to integrated thermal actuators. The corresponding fabricated structure is shown on the right. d) The drop and through port spectrum during the hitless operation for different stages: connected state (0 V, red), disconnected state (1.3 V, black), and intermediate state (0.9 V, blue; 1 V, green). Reproduced with permission.<sup>[72]</sup> Copyright 2021, Nature Communications.

The hitless operation has been achieved with the help of p–i–n junction acting as an optical attenuator. The polarization-dependent loss is found to be 1.2 dB.

The above subsection focuses on RR architectures and provides details about how to realize flat-top sharp roll-off filters and how to achieve polarization insensitivity. The different approaches for increasing the FSR, which often limits the application of MRRs, have been also discussed. The next section reviews the WBGs which are free from FSR-related problems and inherently provide flat top response.

### 5.1.3. Waveguide Bragg Grating (WBG)

Due to a flat-top response, tunability over a wide wavelength range, and ultra-large FSR, WBGs in WDM configuration have emerged as a promising approach to meet the requirement of high data transmission capacity. In a conventional architecture, WBG has two ports (input/reflect and through). To separate the reflected port from the input one, a circulator can be used. However, the presence of a circulator also makes a simple geometry complicated. To avoid this, a four-port geometry can be implemented (input, reflect/drop, add, and through), which has been realized using highly asymmetric contra-DCs (contra-DCs),<sup>[119–121]</sup> combining the MMI with two WBGs<sup>[122]</sup> or multimodal waveguide gratings (MWGs) with an adiabatic coupler.<sup>[123]</sup> The structure based on MWGs provides the best fabrication tolerance due to the larger waveguide geometry. Various multichannel filters have been reported by cascading the WBGs which are capable of realizing reconfigurability in

terms of central wavelength and bandwidth, suitable for flexible networking.<sup>[119,124]</sup>

In WBG, the main source of concerns is the SLSR, which causes strong crosstalk between different channels. Therefore, different apodization techniques, like amplitude modulation and phase modulation, have been reported for the improvement of the SLSR. In the amplitude modulation scheme, the recess amplitude of the side wall corrugation is modulated following the Gaussian function along the direction of propagation, inducing Gaussian apodization in the coupling coefficient.<sup>[125,126]</sup> However, this technique cannot suppress the side lobes in the shorter wavelength side, due to local effective index change caused by the local change in recess amplitude.<sup>[36]</sup> To overcome this, both the waveguide width and recess amplitude should be tightly controlled, which requires precise fabrication.<sup>[127]</sup> In the phase apodization technique, the grating tooth on the two sides of the waveguide is placed with a lateral mismatch having Gaussian apodization along the direction of propagation,<sup>[128]</sup> as shown in **Figure 12a**. An adiabatic coupler is added at the input side to separate the drop port from the input. This introduces a cosine-like apodization in the coupling coefficient ensuring strong suppression of the side lobes. **Figure 12b** shows the reflected spectrum with phase modulation having an SLSR of 22 dB.<sup>[128]</sup> The left and right inset images show the comparison between the spectrum of a normal grating and amplitude apodized grating. The SLSR without the apodization is quite low (7 dB) whereas the amplitude apodization improves the SLSR (15 dB) only on the right side.

Using the phase apodization technique, a four-channel CWDM flat-top filter with four cascaded MWGs has been

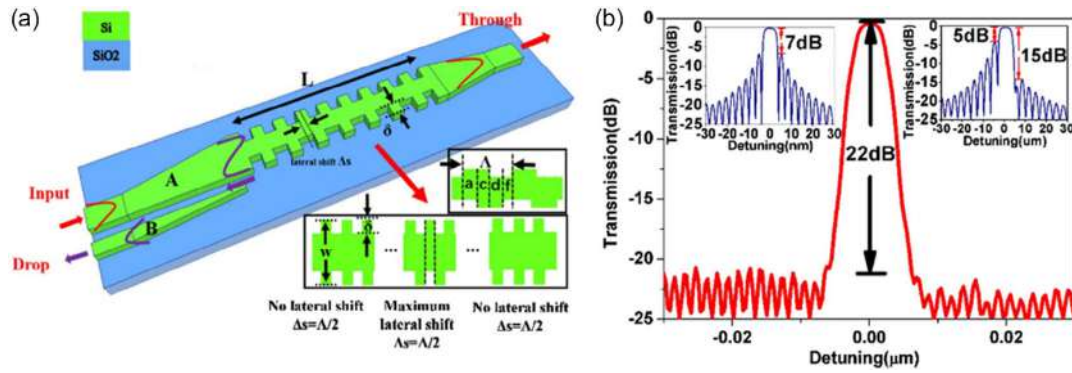


**Figure 12.** a) Schematics illustration of lateral shift apodized WBG in a multimode waveguide. b) The reflected spectrum of the reported structure has an SLSR of 22 dB. The inset shows the reflected spectrum for a WBG without apodization (left) and one with amplitude apodization (right). Reproduced with permission.<sup>[128]</sup> Copyright 2017, Applied Optics.

designed with low crosstalk ( $< -20$  dB), low IL ( $< 1$  dB), and a large 1 dB-bandwidth  $\approx 15$  nm in the O-band.<sup>[91]</sup> In particular, the ratio of 0.75 between the bandwidth at 1 and 20 dB ensures sharp roll-off. Moreover, the negative TOC of the SU-8 upper cladding guarantees low thermal cross-sensitivity ( $46 \text{ pm } ^\circ\text{C}^{-1}$ ). In another study, a four-channel CWDM filter is realized with four cascaded contra-DCs with a channel spacing of 6 nm, bandwidth of 3 nm, and an in-band ripple  $< 0.8$  dB.<sup>[129]</sup> The high-index contrast of Si/SiO<sub>2</sub> produces a strong dielectric perturbation, leading to a large 3 dB bandwidth. Although the width of the grating teeth can be reduced to achieve narrow bandwidth, it is often limited by state-of-the-art fabrication facilities. Therefore, it is particularly challenging to implement WBG for the DWDM application. To overcome this issue, a four-channel DWDM filter based on phase-apodized cascaded contra-DCs is reported in ref. [119], where a narrow bandwidth has been achieved by

carefully designing the two waveguide widths and corrugation widths. Further, for each channel, two sets of contra-DCs are cascaded to reduce the bandwidth and to accomplish rapid roll-off. The schematic of the proposed structure is shown in **Figure 13a–c**. The structure shows a 3 dB bandwidth of 0.4 nm, a 3–20 dB bandwidth ratio of 0.5, channel spacing of 1.6 nm, and cross-talk  $< -20$  dB (Figure 13d). A metallic heater is placed on top of each contra-DC to tune each channel individually with a maximum tuning range of 25 nm. In another geometry, an RR has been used with contradirectional WBG to realize a four-channel DWDM filter with a 3-dB bandwidth of 0.5 nm and crosstalk of 16 dB.<sup>[92]</sup>

Several WBG-based geometries have been reported for the simultaneous tuning of bandwidth and central wavelength to move from a fixed frequency grid to a flexible WDM system.<sup>[130,131]</sup> Yves et al. demonstrated simultaneous tuning by

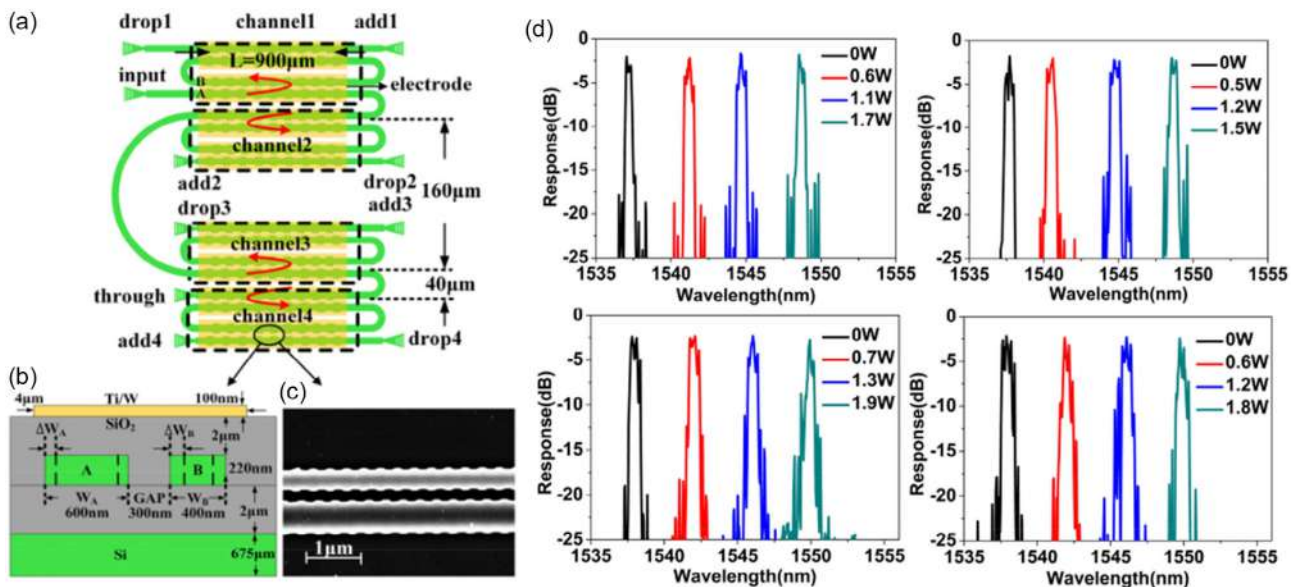


**Figure 13.** a) Schematics of the four-channel add-drop filter with lateral apodization, b) the cross-sectional view, and c) SEM image of the fabricated structure, with an illustration of lateral shift apodized WBG in a multimode waveguide, and d) measured spectrum of the four channels for different heating powers. Reproduced with permission.<sup>[119]</sup> Copyright 2019, IEEE OAPA.

cascading two contra-DCs with amplitude apodization.<sup>[132]</sup> In the structure, the drop port from the first contra-DC feeds into the input port of the second contra-DC. The two heaters are placed on top of each contra-DC to realize the reconfigurability. To tune the bandwidth, the second heater is activated keeping the first heater fixed whereas both heaters are simultaneously activated to tune the central wavelength. The bandwidth tuning range is found to be 5.36 nm. A higher-bandwidth tuning range of 11.65 nm has been reported in ref. [133], using cascaded MWGs in a loop which also provides central wavelength tuning over a span of 13 nm. Wang et al. recently reported a two-channel filter with the two cascaded geometries of MWGs for the hitless and gridless tunability of the central wavelength and bandwidth, which demonstrated that one channel can be tuned independently without perturbing the other channel.<sup>[134]</sup> The 3 dB bandwidth was tuned from 0.2 to 2.4 nm whereas the central wavelength by 14.5 nm.

One critical issue of WBGs that limits their use in WDM applications is the strong birefringence of silicon waveguides. The polarization splitter and combiner can be used with the WBG-based component to process the TE and TM modes separately,<sup>[135,136]</sup> at the expense of a larger overall footprint. Therefore, various polarization-insensitive WBG filters have been designed to address this issue. For example, Liu et al. designed a dual-polarization-based add-drop filter with MWG and adiabatic coupler in which two gratings designed for the TE and TM modes are cascaded together.<sup>[137]</sup> The triangular (rectangular) shape grating is used to couple the fundamental TE (TM) mode with the higher-order TE (TM) mode having grating periods designed such that the resonance occurs at the same wavelength in the C-band of telecommunication. The phase shift apodization has been used with a lateral shift of two sidewall gratings to suppress the sidelobes. An IL of 0.6 and 1.5 dB, 3 dB bandwidth of 11 and 12 nm, and SLSR of 23 and 17 dB have been achieved for TE and TM mode, respectively, with a shift between the Bragg wavelengths of 0.7 nm caused by fabrication issues. The triangular corrugation profile of

TE-mode MWG is used to reduce the undesired reflections and suppress Fabry–Perot resonances. Recently, Ning et al. used a hybrid geometry of Si and SiN to realize a polarization-insensitive response of MWG-based structure,<sup>[138]</sup> as shown in **Figure 14a,b**. The sidewall gratings with the lateral shift apodization have been used to couple the fundamental and higher-order TE modes, whereas the loaded SiN grating with lateral apodization is placed on top of the structure to couple the TM modes. The periodicity of two gratings is adjusted to achieve the same resonance wavelength of around 1.55  $\mu\text{m}$ . For the TE (TM) mode, the 3 dB bandwidth, IL and SLSR are found to be 5.1 nm (3.5 nm), 1 dB (1.72 dB), 18.5 dB (19.1 dB), respectively (see Figure 14c).

The detailed review on WBG addresses issues like improving SLSR and realizing polarization insensitivity as well as discusses the potential of these devices toward flexible WDM applications. Here, we like to mention that WBGs can be considered as 1D photonic crystals. The periodic or aperiodic variation of refractive indices in 2D or 3D respectively generates 2D or 3D photonic crystals, also characterized by the presence of photonic bandgaps. Over the years, WDM filters based on silicon 2D or 3D photonic crystals have been reported. A detailed analysis of such WDM filters and their performance can be found in very recent review articles.<sup>[139,140]</sup>

#### 5.1.4. Arrayed Waveguide Grating (AWG)

The AWG is the most commonly used device for the WDM application. Due to the large-index contrast, silicon waveguides drastically scale down the AWG-based device cross section from  $\text{cm}^2$  to  $0.1 \text{ mm}^2$  or even less. However, the phase errors originating due to the large area of the structure make it desirable to keep reducing occupied space.<sup>[141]</sup> The large size of AWG also hinders efficient tuning of different channels in flexible WDM systems due to high power consumption. For example, in ref. [142], the central wavelength of the channels has been tuned by the TO effect with a very low tuning efficiency of  $7.5 \text{ pm mW}^{-1}$  and

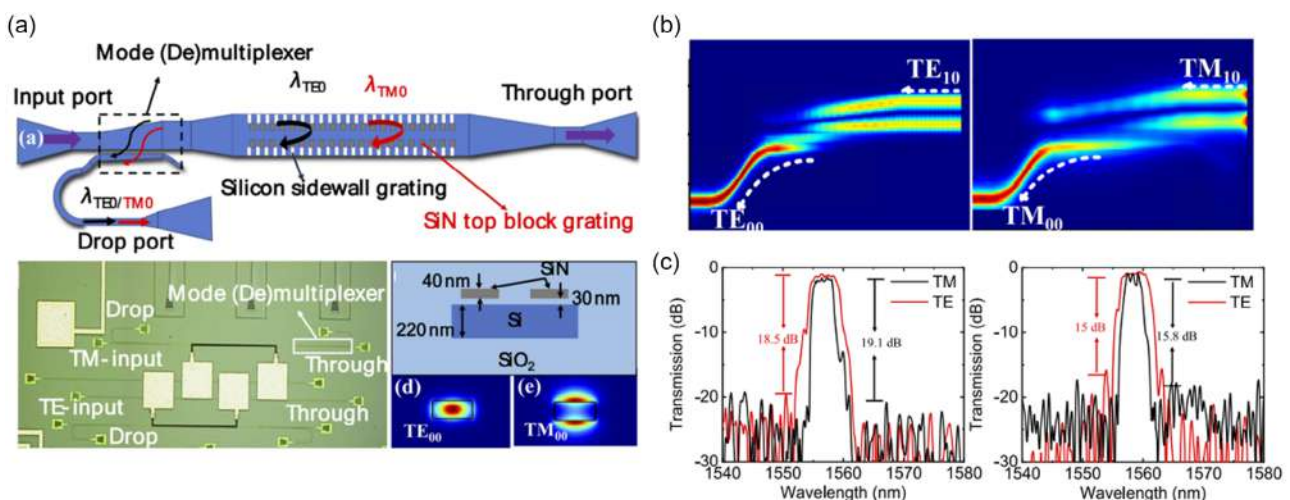


**Figure 14.** a) Schematic diagram of the polarization-insensitive filter and the top view of the fabricated structure, b) propagating field distribution of two polarizations, and c) the spectrum for two polarization-insensitive filters with different dies. Reproduced with permission.<sup>[138]</sup> Copyright 2023, Optics Letters.

high-power consumption of 7600 mW/FSR. Therefore, to reduce the footprint, different techniques, like reflective-type AWG and bidirectional AWGs, have been adopted. To reduce the size, unlike transmission-type AWG, in reflection mode, a reflecting architecture has been used at the end of the arms of phased array waveguides. Different approaches, such as distributed Bragg grating (DBR),<sup>[143,144]</sup> photonic crystal reflectors,<sup>[145]</sup> reflecting surfaces,<sup>[146,147]</sup> etc., have been reported by the different research groups. For example, Okamoto et al. reported a reflective-type AWG with second-order DBR as the reflection facet.<sup>[143]</sup> The proposed structure has a 14-output channel with a spacing of 400 GHz and crosstalk of  $-20$  dB within a footprint of  $230 \mu\text{m} \times 530 \mu\text{m}$ . The average length of the array waveguides in reflection mode is found to be 3–4 times lower than that of transmission mode. To further reduce the overall footprint, a reflective AWG structure with photonic crystal has been analyzed,<sup>[145]</sup> as shown in **Figure 15a**. The proposed idea considers dielectric photonic crystal mirrors producing a WDM system with an eight-channel spacing of  $0.8$  nm (Figure 15b), a footprint of  $134 \mu\text{m} \times 115 \mu\text{m}$ , excess loss of 3 dB, and crosstalk of  $-12$  dB.

Chen et al. demonstrated an 18-channel DWDM with a bidirectional AWG structure and MZI interleaver, shown in Figure 15c.<sup>[148]</sup> The proposed structure has a total footprint of  $520 \mu\text{m} \times 190 \mu\text{m}$  with 200 GHz channel spacing and channel crosstalk between  $-15$  and  $-18$  dB (Figure 15d). It has been shown, that instead of two AWG and MZI interleavers, a single bidirectional AWG with MZI can be used to achieve the double-channel number and halved channel spacing.

The application of the AWG in closely spaced WDM is often limited by thermal crosstalk due to the high TOC of silicon and strong birefringence of the Si waveguide. To compensate for the huge birefringence of the Si waveguide, unlike conventional

AWGs, an angled star coupler in Rowland circle configuration combined with different diffraction orders associated with TE and TM mode has been utilized by Zou et al.<sup>[147]</sup> The polarization-dependent wavelength shift of all the channels of a CWDM has been cut down from 380–420 to 0.5–3.5 nm, at below 25% of the 3 dB bandwidth of each channel. The crosstalk associated with the TE (TM) mode is  $< -14$  dB ( $-18$  dB). In another approach, Dai et al. optimized the cross-sectional dimensions of the arrayed waveguides to realize polarization-insensitive channel spacing which simultaneously holds good fabrication tolerances.<sup>[149]</sup> In addition, the different diffraction orders for the TE and TM modes have been utilized to reduce the polarization-dependent wavelength shift. To compensate for the thermal dependence, waveguide dimension optimization, combined with negative TOC polymer, has been used.<sup>[150]</sup> However, it puts a strict restriction on the waveguide dimension. Chen et al. proposed two different architectures to reduce thermal dependence where the slab or the free propagation region has been used.<sup>[151]</sup> In one case, the slab region has been divided into two sections having different upper cladding, whereas in the other case, the coupling section has been designed with an oblique incident. The wavelength shift due to the ambient temperature is found to be  $5 \text{ pm } ^\circ\text{C}^{-1}$ .

Recently, Chung et al. reported a bidirectionally tunable (both red and blueshift) AWG for fine tuning of filtering response with the potential of stabilizing the spectral response using a feedback loop.<sup>[152]</sup> Instead of a rectangular footprint, an S-shaped footprint has been utilized with two triangular-shaped heaters with complementary phase distributions, as shown in **Figure 16a**. The proposed structure illustrated a bidirectional linear shift (Figure 16b), with a tuning efficiency of  $30.5 \text{ nm } \text{W}^{-1}$  over the wavelength range of 8 nm.

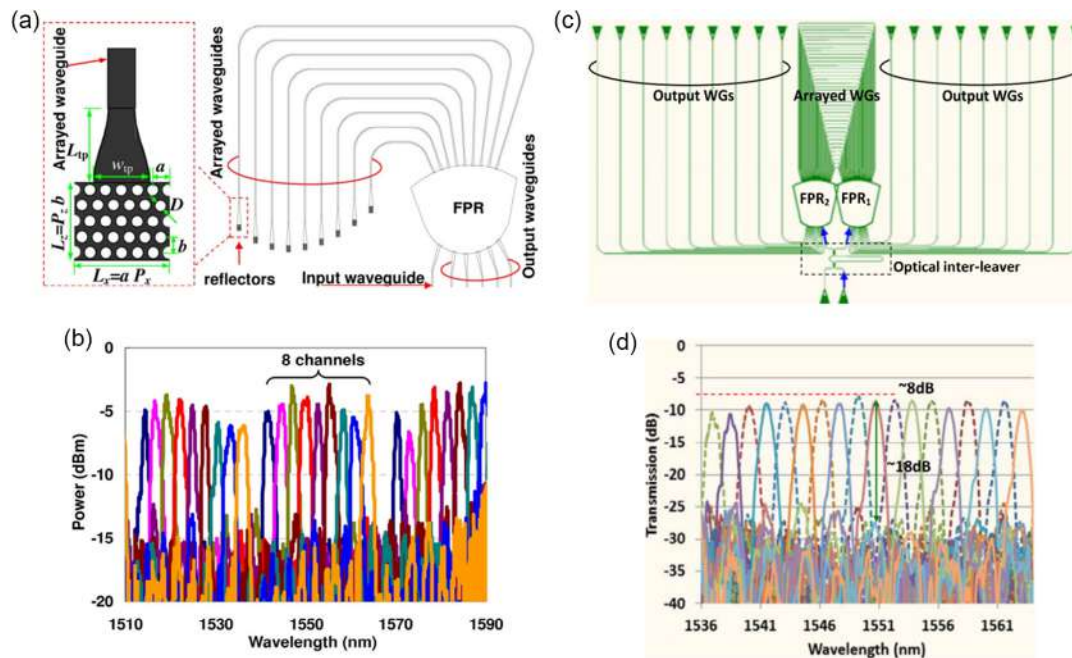


**Figure 15.** a) Schematics diagram of the reflected AWG with photonic crystal and b) the reflector and the corresponding eight-channel spectrum. Reproduced with permission.<sup>[145]</sup> Copyright 2013, Optics Letters. c) Bidirectional-AWG with MZI interleaver and d) the output spectrum. Reproduced with permission.<sup>[148]</sup> Copyright 2015, Journal of Lightwave Technology.

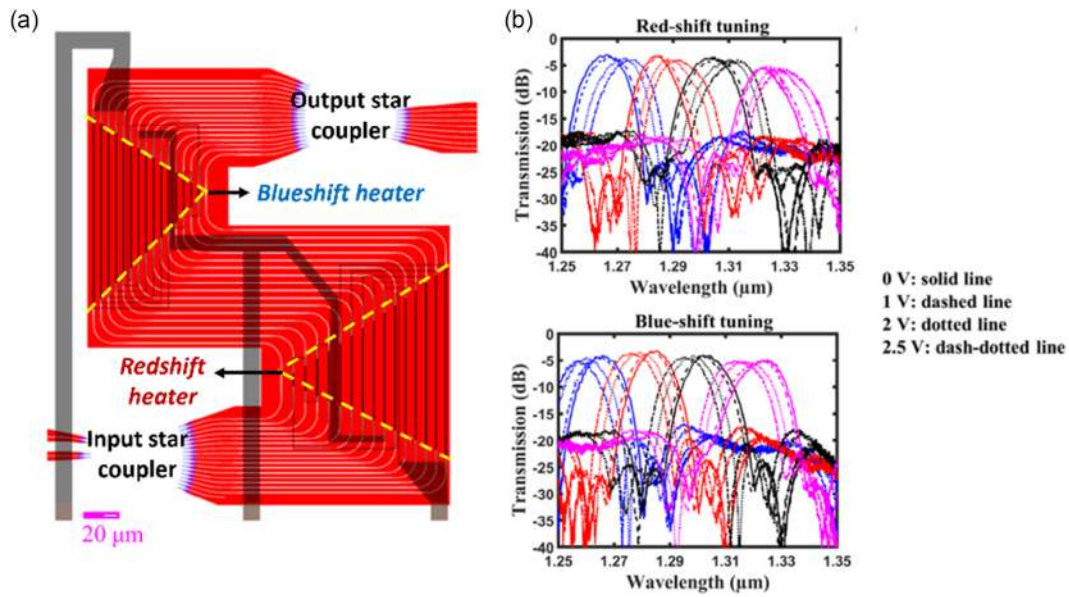


**Figure 16.** a) Mask layout of the bidirectionally tunable AWG structure and the position of the two heaters and b) redshifted and blueshifted spectrum response for four different applied voltages to the micro-heater. Reproduced with permission.<sup>[152]</sup> Copyright 2022, OAPA.

Liu et al. demonstrated a 64-channel DWDM, around a wavelength of 2  $\mu\text{m}$ , driven by the demand to extend the telecommunication band from the conventional C + L band.<sup>[153]</sup> The proposed structure has 64 channels with a spacing of 50 GHz spanning over a wavelength range from 1967 to 2012 nm. The channels can be tuned through a metallic heater of TiN with a tuning efficiency of 0.27 GHz  $\text{mW}^{-1}$ . The proposed structure potentially allows for 100 Gbit  $\text{s}^{-1}$  and even more using suitable modulation schemes.

This subsection provides a detailed review on AWGs, showing their potential for DWDM applications, different techniques in

realizing polarization insensitivity, as well as approaches to reduce the size of the AWG architecture.

### 5.1.5. Discussions on Filter Architectures for Optical Communication

To provide an overall comparison between different filter architectures, **Table 4** summarizes the performance of such filters with applications targeting CWDM and DWDM. The table includes important parameters such as IL, bandwidth, crosstalk

**Table 4.** A comparison table between different filter architectures for optical communication.

	Structure	IL [dB]	Bandwidth [nm]	Crosstalk [dB]	Tuning efficiency	Telecommunication band	Size [ $\mu\text{m}^2$ ]	References	
CWDM	MZI	1.6	–	15	–	S-Band	500 × 400	[97]	
		$\approx 1$	19 (3-dB)	20	–	O-Band	300 × 100	[99]	
		0.9	2.3 (1-dB)	20.6	–	2 $\mu\text{m}$	500 × 900	[95]	
	MRR	0.8	2.6 (3-dB)	18	–	C & L-Band	–	[113]	
		WBG	1	3 (3-dB)	16	–	C-Band	1.6 × 950	[92]
			$\approx 1$	15 (1-dB)	20	–	O-Band	40 × 600	[91]
AWG	5	6.7 (3-dB)	25	–	O-Band	55 × 3900	[293]		
	2.5–6	–	11	–	O-Band	700 × 270	[294]		
	DWDM	MZI	–	–	22	–	C-Band	–	[93]
		MRR	0.82	0.4 (3-dB)	–	8.95 $\text{pm V}^{-1}$	L-Band	15 × 60	[94]
WBG	1.5–4.5	0.3–0.4 (3-dB)	20	0.45 $\text{nm mW}^{-1}$	C-Band	–	[295]		
	1	0.5 (3-dB)	16	–	C & L-Band	–	[92]		
AWG	2.6	0.4 (3-dB)	20	0.007 $\text{nm mW}^{-1}$	C-Band	$\approx 350 \times 900$	[119]		
	3.9–8.4	0.66 (3-dB)	21.65	–	O-Band	270 × 580	[296]		
	3.6	–	20	0.03 $\text{nm mW}^{-1}$	O-Band	–	[152]		
	6.28	–	27	–	C & L-Band	276 × 299	[297]		

between different channels, the footprint, that is, the overall size, tuning efficiency, as well as the telecommunication band in which it is applicable. The table shows that the IL is very small ( $\approx 1$  dB) for all the architectures except AWGs in which it is slightly higher. In terms of device footprint, the MRR is the best choice and next to it is WBGs. The size is usually larger side for MZIs and AWGs, highlighting the requirement of higher power consumption to realize reconfigurability.

The above discussion points out various challenges and future trends in research work with these commonly used filtering techniques in silicon photonic platforms. The high-index contrast of silicon waveguide makes it possible to realize dense integration and is thus suitable for large-scale integration over a small footprint. However, the large-index contrast also brings issues in fabrication accuracy as slight variations in waveguide parameters cause a significant deviation from the desired performance. In addition, the sidewall roughness causes unwanted loss as well as phase changes, degrading the filters' performance, especially for resonance-based structures like WBGs and MRRs. Therefore, fabrication-tolerant design strategies are strongly requested, which can be achieved through smarter designing approaches like machine learning.<sup>[154,155]</sup> Thanks to the small footprint and better flexibility, MRRs and WBGs are gaining great attention in realizing flexible WDM technology which offers hitless and gridless tuning.<sup>[72,134]</sup> It implies the tuning of central frequency as well as of the bandwidth of a particular channel without perturbing other channels. This is particularly suitable for multimedia and cloud computing, inter and intra data center interconnects, 5G backhauling networks etc.<sup>[156,157]</sup> For DWDM, applications based on AWGs are found to be the most suitable ones. For example, a  $512 \times 512$  AWG router is reported with only 25 GHz of channel spacing in a silicon photonic rib waveguide, reflecting its potential.<sup>[158]</sup> The two main issues with AWGs which should be addressed in future are nonflat-top response and larger footprint. Operating AWGs in bidirectional mode or reflection mode can be one option to reduce the footprint as discussed above. Recently, it has been reported that parabolic tapering at the input end of AWGs can provide a flat-top response but with a high IL of around 3 dB.<sup>[159]</sup> Taking advantage of each filter architecture and high integration possibility, merging different silicon filter architectures can be a future goal to realize flexible WDM over large channels. However, further miniaturization, power-efficient operation, and fabrication accuracy are still required. The last is expected to be achieved with the advancement in fabrication and smart design technologies. Integration of silicon photonic filters with phase change materials (PCMs) shows promising growth in recent times which can

offer a power-efficient and more compact architecture.<sup>[160,161]</sup> In PCMs, the phase change from crystalline to amorphous or vice versa causes a large change in refractive indices. Therefore, better reconfigurability can be achieved with a smaller tuning element which significantly reduces the power consumption and device footprint. Further, due to their nonvolatile nature, a constant power supply is also not required to operate the filters. Given that, different PCM materials such as  $\text{Ge}_2\text{Sb}_2\text{Te}_5$  (GST),  $\text{Ge}_2\text{Sb}_2\text{Se}_4\text{Te}_1$  (GSST), and  $\text{Sb}_2\text{Se}_3$ , are rapidly emerging in recent times.<sup>[162]</sup> The one drawback of such materials is that, in addition to the large change in the real part of the refractive index, phase change also induces a large change in their absorption coefficient. Therefore, researchers are in constant search for new PCM materials as well as smart approaches to integrate PCM in silicon photonic platforms. The advancement of WDM technology and the possibility of monolithic or hybrid integration with lasers, modulators, and germanium-silicon photodiodes can result in high-capacity silicon photonic transceivers, expected to dominate the future communication technologies.<sup>[163]</sup>

## 5.2. Microwave Photonics Filters

MWP is becoming a trending topic in the research field since it allows to manage RF signals derived from telecommunications at the rate, bandwidth, and data processing capability typical of photonics. It involves the advantageous integration of microwave technology with photonics to enable the generation, processing, and distribution of microwave signals with the use of optical waveguide architectures. A generic schematic diagram of MWP is shown in **Figure 17**. The laser source generates the optical carrier frequency ( $\omega_c$ ) (in the telecommunication bands) which is modulated by the RF signal ( $\omega_{RF}$ ). The modulated signal is further processed through the compact high-speed photonic ICs (PICs) followed by conversion back to the RF domain through the photodiodes. This kind of ability could be extremely useful in several fields, such as space, guaranteeing fast on-board data processing and interlinking for Earth observation, communications, and aviation aims.<sup>[164–166]</sup> A key element in this emerging field is the filter, useful in RF front-end receivers to cancel noise, reduce RF interference, and avoid RF amplifier saturation. Its use is crucial in applications that need wide bandwidth, ultra-wide tuning bandwidth, high integrability, and low losses, as next-generation telecommunications.<sup>[22]</sup> The main operation of an MWP filter in an RF receiver is sketched in **Figure 18**.

After an electro-optic (E/O) transducer, an integrated photonic processor performs filtering of undesired spectral components.

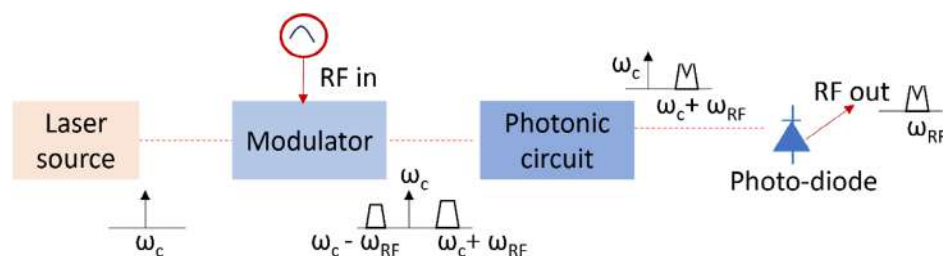


**Figure 17.** Schematic representation of a typical MWP setup.

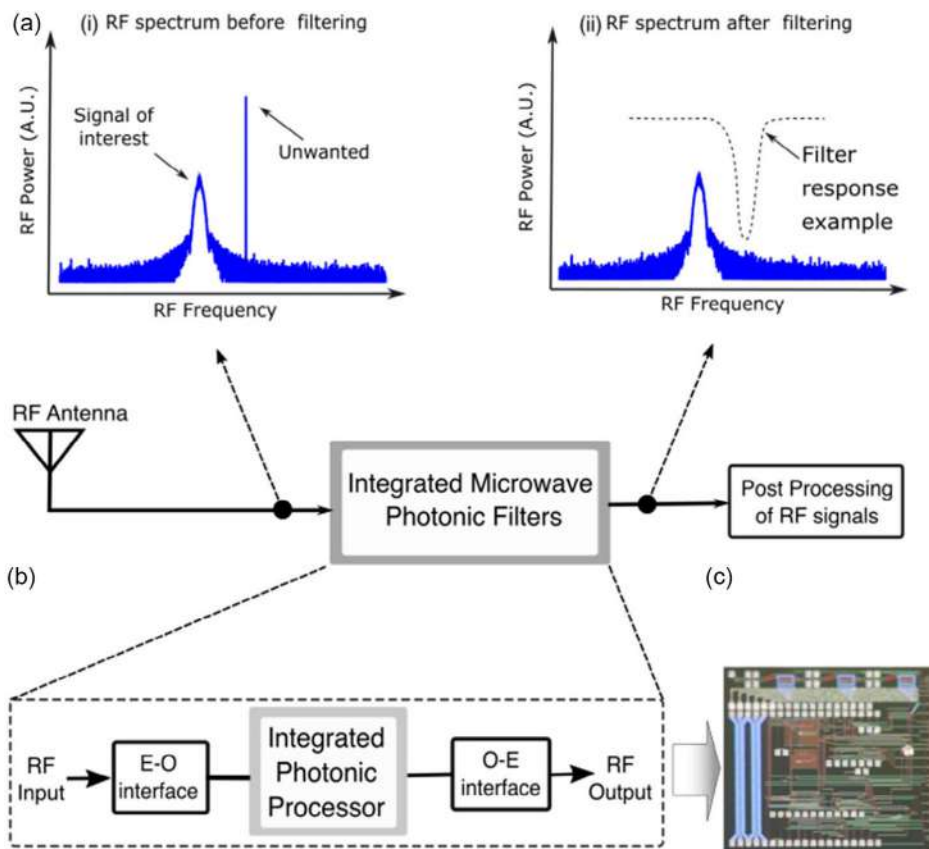


**Figure 18.** a) Scheme of an RF receiver, consisting of an RF antenna, an IMWPF, and an RF postprocessing circuit, b) typical IMWP filter architecture, c) scheme of fully integrated IMWP filter. a(i) RF spectrum of received RF signals consisting of a weak signal of interest and a strong undesired interference. a(ii) Filtered RF spectrum. The filter response (the dashed curve) suppresses the strong interference without attenuating the signal of interest. Reproduced with permission.<sup>[22]</sup> Copyright 2020, Advances in Optics and Photonics.

The RF signal, generated by opto-electronic (O/E) transduction, is sent to the postprocessor. The chain of O/E transducer integrated photonic processor, and E/O transducer forms the so-called integrated MWP filter (IMWPF). The E/O transducer consists of a modulator performing the upconversion from RF to optical wavelengths, while the O/E transducer performs the downconversion from optical to RF wavelengths, as the photodetector (PD).

The most important parameters to rate a silicon IMWPF are the bandwidth, the rejection ratio, the tunability, and the spurious free dynamic range (SFDR), which in turn depend on the sidelobe suppression ratio.<sup>[22]</sup> According to the devices proposed in the literature, the architecture of MWP filters could be classified, as a tapped delay line or down-converted response of a coherent optical filter.

In the tapped delay line architecture, the filter is made by the sum of RF signal copies, with different amplitudes and delays that have to be properly chosen to create the desired periodic frequency response.<sup>[166]</sup> If the tap number is countable, the filter shows a finite impulse response (FIR), while if the tap number is approximately infinite, the filter shows an infinite impulse response (IIR), with larger ER and narrower bandwidth with respect to FIR ones.<sup>[167,168]</sup> However, it should be noted that this architecture needs a lot of few GHz sources, resulting in expensive, bulky, and niche in the market. However, to overcome this

problem, the use of a comb laser has been suggested, bringing also reconfigurability and flexibility according to the number and features of the selected taps.<sup>[22,169]</sup> The architecture of the tapped delay-based MWP filter is sketched in **Figure 19**, where the key building blocks are the multifrequency optical sources, as the microresonator-based optical frequency comb,<sup>[170]</sup> the spectral shaper, that sets amplitude and phase to each tap, and a dispersive delay line, to create a basic unitary delay between consecutive taps.<sup>[166,171]</sup> As a spectral shaper, an AWG could be used combined with a semiconductor optical amplifier (SOA) to also guarantee reconfigurability, while a photonic crystal could be used as dispersive delay line.<sup>[171]</sup>

As a coherent filter, the basic architecture is schematized in **Figure 20**, which mainly consists of a single-wavelength optical source at  $\lambda_s$ , as a continuous wave (CW) laser,<sup>[144]</sup> and an on-chip optical filter with tailored frequency response. The phase modulator (PM) is fed by an RF signal at  $\lambda_{RF}$  and it generates a modulated optical signal, with an optical carrier at  $\lambda_s$  and sidebands located at  $\lambda_s \pm \lambda_{RF}$ . The optical filter coherently modifies the sideband spectra. At the end of the process, the optical signal is reconverted into an RF signal by the PD which transduces the optical power into an electrical current.<sup>[142]</sup> The coherent filter operation guarantees higher flexibility with respect to the multi-tapped ones, and flexibility of the output spectrum, since it is

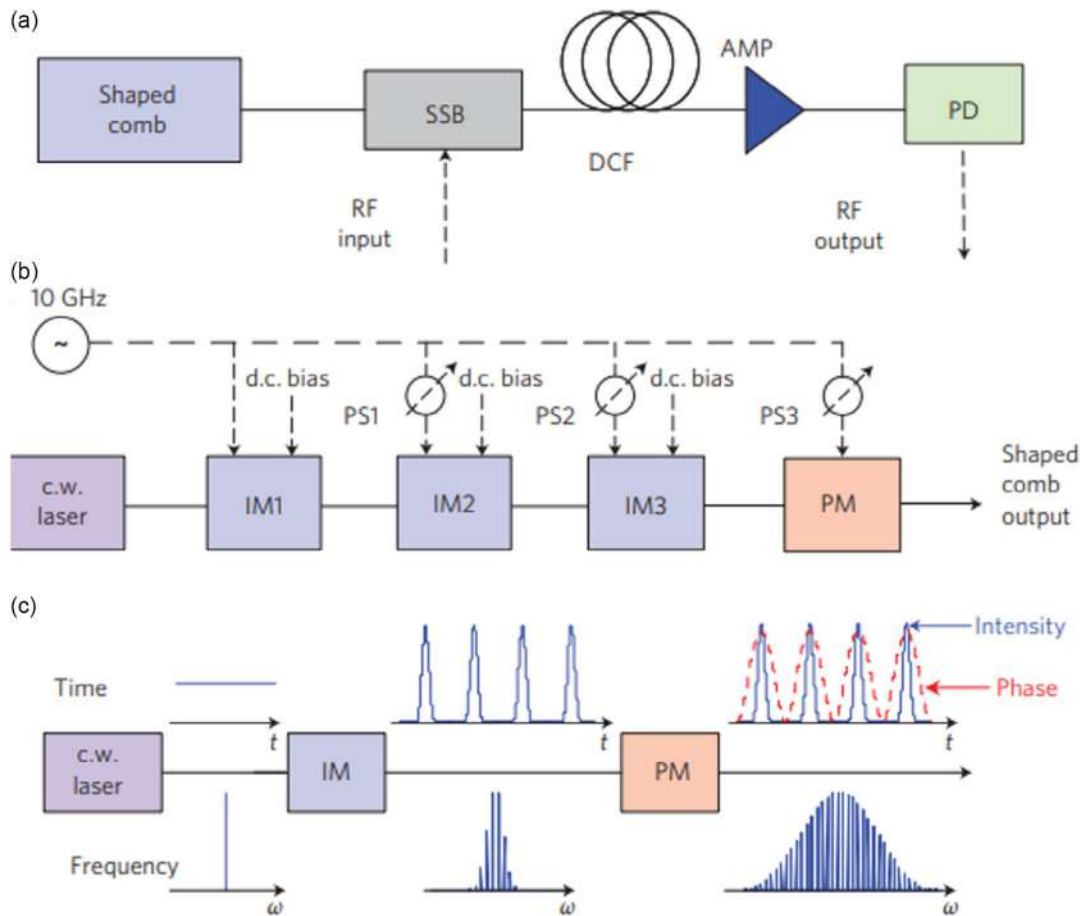


**Figure 19.** a) Schematic of a multitap MWP filter using an optical frequency comb, a SSB, dispersion-compensating fiber, fiber amplifier (AMP), a PD, b) experimental scheme representation, c) experimental scheme of direct quasi-Gaussian frequency comb generation. CW laser; intensity modulator; PM (PS) microwave phase shifter. Reproduced with permission.<sup>[173]</sup> Copyright 2012, Nature Photonics.

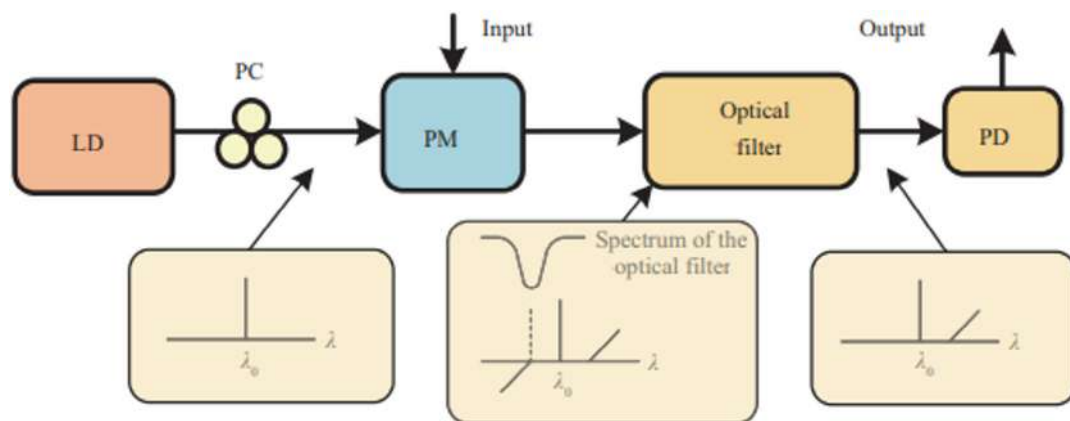


**Figure 20.** Schematic of a coherent MWP filter, in which an optical notch filter is used to filter out one sideband of a phase-modulated signal, thus achieving phase modulation to intensity modulation conversion. Reproduced with permission.<sup>[164]</sup> Copyright 2022, Science China. Information sciences.

easily tunable by changing the optical carrier and/or the optical filter central frequency. To perform band-stop or band-pass behavior, the simplest approach is based on single-sideband modulation (SSB) and spectrum mapping, which one-to-one

maps the optical response into the RF one. The SSB modulation can be easily implemented by filtering one RF sideband or using a dual-parallel Mach-Zehnder Modulator (DPMZM) or a dual-drive MZM (DDMZM).<sup>[142]</sup>

As from the topologies in Figure 19 and 20, the performance of the optical filter affects the overall system. Therefore, the research pushes for the improvement of the performance of photonic filters since the other MWPF building blocks are conventional.

One of the most important features for the next generation of filters is the tunability that guarantees the flexibility of the RF system. The most common approaches for the tunability of Si-based optical filters are the conventional ones, as TO<sup>[169,172]</sup> and EO,<sup>[172–174]</sup> extensively described in Section 4. EO tuning allows fast reconfigurability (of the order of ns) at the expense of a limited tunability range, while TO guarantees a larger tunability range and limited power consumption with slower reconfiguration time (of the order of  $\mu$ s). According to the target application and related requirements, several topologies of Si-based IMWPFs have been proposed in the literature, mainly based on RRs, subwavelength gratings (SWGs), ring-assisted Mach–Zehnder interferometers (RAMZIs), or exploiting the stimulated Brillouin scattering (SBS) nonlinear effect.

### 5.2.1. Ring Resonators (RRs)

RRs bring the advantages of compactness, unique amplitude, phase response, and the easy tunability of the central frequency.<sup>[35,175–177]</sup> However, it should be noted that a trade-off between the rejection ratio and the filtering bandwidth limits the performance. The bandwidth, strictly correlated to the propagation losses, increases as the coupling ratio increases, while the rejection ratio shows a maximum value in correspondence with the critical coupling condition when the coupling light compensates for the optical losses.<sup>[22]</sup>

The early Si resonators, with ring or disk shapes, showed a rejection ratio  $>20$  dB and a bandwidth of tens of GHz, due to the large propagation losses in the C-band ( $\approx 3$  dB  $\text{cm}^{-1}$ ).<sup>[178–180]</sup> As an example, Long, et al proposed MRR with a radius of 10  $\mu\text{m}$  for filtering at 20 GHz, with a rejection ratio  $>15$  dB, a bandwidth of 12 GHz, and a tunability of the central frequency of 14.2–30.6 GHz by varying the laser central frequency. The rejection ratio has been further improved up to 60 dB by cascading a tunable bandpass filter.<sup>[179]</sup> Since the bandwidth is mainly limited by the propagation losses, silicon multimodal waveguides with a width greater than 2  $\mu\text{m}$ <sup>[181]</sup> have been investigated, aiming at reducing the mode interaction with the rough sidewalls. A bandpass filter bandwidth of 170 MHz with a tunability of 2–18.4 GHz and a rejection ratio  $>26$  dB has been achieved by a thermal tunable racetrack resonator with Q-factor  $>10^6$  based on a 2  $\mu\text{m}$ -wide Si waveguide with a loss coefficient of 0.25 dB  $\text{cm}^{-1}$ .<sup>[182]</sup> The racetrack configuration leads to a larger and more accurate coupling region and then coupling coefficient with respect to RR, mainly ensuring the enhancement of the rejection ratio.

Besides the Lorentzian shape and a rejection ratio correlated to fabrication constraints, the principal drawback of the RR is the limited roll-off and SFDR for a bandpass filter, linked to the periodic spectral response of the architecture. The resonant nature of RR leads to multiple equally spaced resonances (FSR) with the same amplitude that, therefore, strongly limits the SFDR for bandpass and notch filter, respectively. This issue could be solved by engineering the FSR via the exploitation of the Vernier

effect<sup>[183]</sup> or using the parallel-cascaded RR configuration,<sup>[184]</sup> at the expense of a limited rejection ratio. Zhuang et al. proposed cascaded racetrack resonators with different radii to achieve a larger FSR with respect to a simple RR, with a flat-top bandpass shape  $<1$  GHz wide and a rejection ratio of 3 dB.<sup>[183]</sup>

To enhance the tailoring capability of the ring filtering shape, the double-injection technique has been investigated. It consists of two waves that travel through the waveguides toward the resonator, where they are injected into the racetrack in opposite directions. Since both injected waves show the same wavelength, they interfere with each other inside the racetrack, thus allowing to obtain several filtering transmission windows.<sup>[185]</sup> An all-pass filter that consists of a double-injection-based racetrack resonator has been proposed in ref. [186], with a rejection ratio of 50 dB and a bandwidth of 40 GHz. By adjusting the voltage applied to the microheaters deposited on the MRR, several functions can be implemented, ranging from passband to notch filter, in addition to tuning of the central frequency up to 40 GHz.

### 5.2.2. Coupled Ring Optical Waveguides (CROWs) and Side-Coupled Integrated Spaced Sequence of Resonators (SCISSORs)

To achieve both a large rejection ratio and flat-top response for a bandpass filter, however neglecting the engineering of the FSR that results to be constant, coupled ring optical waveguides (CROWs) have been proposed. They consist of  $N$  vertically coupled resonators with a single-input waveguide. Several degrees of freedom of coupling coefficients between RRs guarantee an increased spectral bandwidth with respect to a single RR.<sup>[187]</sup> To increase the filter roll-off targeting to a box-like filtering shape, the number  $N$  should be very large ( $N \geq 100$ ) with a resulting bandwidth of tens of GHz.<sup>[187,188]</sup> Promising results have been reported in ref. [189]. The proposed filter consists of three cascaded CROWs with different  $N$  values (see **Figure 21a**). The combination of three stages with different  $N$  values allows to achieve a bandpass filter with top-flat behavior and a large sidelobe suppression ratio ( $>8$  dB) with a bandwidth of 800 GHz. Finally, the use of thermal tuning, not in the coupling regions, allows for further improving the sidelobe suppression ratio.

A different arrangement of RRs, such as side-coupled integrated spaced sequence of resonators (SCISSORs), provides more flexibility, for example, it is possible to widely tune the filtering response or process different signal spectral components with each RR.<sup>[190]</sup> Zhuang et al. proposed a nonuniform SCISSOR (N-SCISSOR), sketched in **Figure 21b**, made of three thermal tunable racetracks with different pathways, able to simultaneously and independently perform filtering and down-conversion. Several filtering shapes have been achieved, ranging from a flat-top bandpass to a notch filter with a rejection ratio larger than 40 dB, both with a bandwidth of about 1 GHz and large reconfigurability (2.75–10.25 GHz).<sup>[191]</sup>

### 5.2.3. Ring Assisted Mach–Zehnder Interferometer (RAMZI)

To further increase the roll-off aiming at achieving a box-like filter response, that is the gold standard in the filtering field, an architecture based on a RR located in an unbalanced RAMZI can be employed.<sup>[192,193]</sup> This configuration merges the

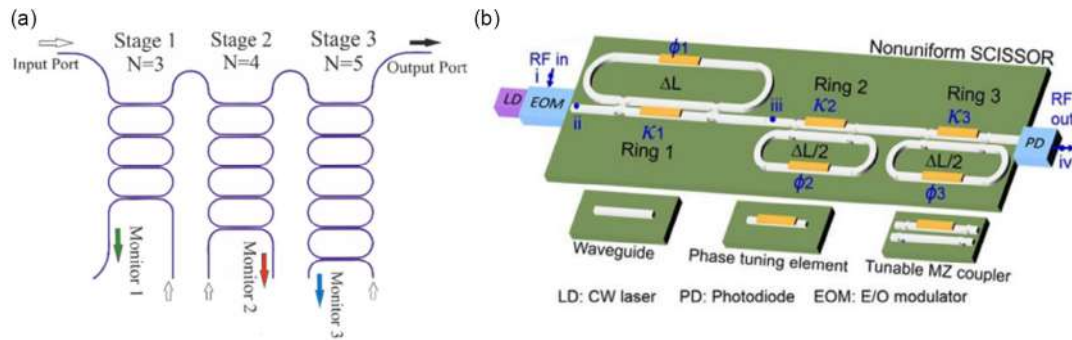


**Figure 21.** a) Schematic layout of a multistage CROW filter with three stages and orders  $N = 3, 4,$  and  $5$ . All individual resonators have identical racetrack layouts and gaps. Reproduced with permission.<sup>[189]</sup> Copyright 2018, CC BY 4.0. b) System configuration of  $N$ -SCISSOR. Reproduced with permission.<sup>[191]</sup> Copyright 2016, Optics Letters.

advantages of RR, as the faster roll-off, and MZI, as the large rejection ratio. To obtain a box-like shape, the system should be designed such that the FSR of MZI should be twice RR.<sup>[22]</sup>

A multifunctional filter with double ring-loaded MZI has been proposed in ref. [194], shown in **Figure 22**. It can implement different filtering windows (Butterworth, Chebyshev, elliptical) adding flexibility in terms of reconfigurability of the architecture. The resulting bandpass filtering shape shows a box-like response with an in-band ripple of 2 dB with bandwidth and overall rejection ratio dependent on the type of the filtering window (minimum  $> 20$  dB), for example, the elliptical BPF presents a bandwidth of 250 GHz with a rejection ratio of 60 dB.<sup>[194]</sup> However, the configuration shows a very large IL ( $\approx 20$  dB), with a large power consumption for thermal tuning of the filter (hundreds of mW).

To further increase the rejection ratio, also preserving the bandwidth at the expense of Lorentzian shape, architectures based on MZI in cascade to RAMZI<sup>[195,196]</sup> have been proposed. Rejection ratios of 60 and 78 dB, with a bandwidth of 780 and 860 MHz, have been experimentally measured in refs. [195,196], respectively, with a frequency tuning range of up to 40 GHz.

If two or more RAMZIs are cascaded, they do not influence each other and can be driven separately. The cascade design enables box-like shapes with ultralarge flatness, large SFDR, and larger tunability range, also allowing to reduce the number of RRs for each stage, resulting in more tolerance to fabrication imperfections, at the expense of a larger footprint. A remarkable thermal tuning range of 760 GHz has been reported in ref. [197],

by cascading second-order RAMZI filter stages, with an ultraflat bandpass shape (in-band ripple  $< 0.1$  dB), ultra rejection ratio of 25 dB, SFDR  $> 60$  dB, very low IL (1 dB), and a bandwidth of 120 GHz. To decrease the footprint of the filter, preserving the benefits of the cascaded RAMZI configuration, the outputs of the RAMZI could be linked together, exploiting the Sagnac effect to produce a mirror.<sup>[198]</sup> However, this solution has not yet been demonstrated in the Si technology platform.

#### 5.2.4. Subwavelength (SWG) and Bragg Gratings

The on-chip SWGs have recently been employed in filtering structures thanks to their compactness and large dispersion features. The gratings are realized by corrugating the sidewalls of the waveguide, either on the ridge or on the slab. The coupling coefficient can be varied by changing the corrugation width and it allows a precise control of the bandwidth and a huge fabrication tolerance. Narrow bandwidth ( $\approx 50$  GHz) has been achieved using SWG  $580 \mu\text{m}$  long, suitable for practical WDM applications.<sup>[199]</sup> However, the performance could be affected by fabrication and temperature changes. During the past years, a remarkable enhancement of the SWG-based filter performance has been obtained thanks to the ongoing improvements of the fabrication tools. Recently, Zhang et al. proposed a fully reconfigurable grating based on SWG that incorporates a defect at the middle, that acts as FP, and an independent lateral p-n junction that can be biased to shift the Bragg wavelength (see **Figure 23**).<sup>[84]</sup> The measured reflection spectrum shows a

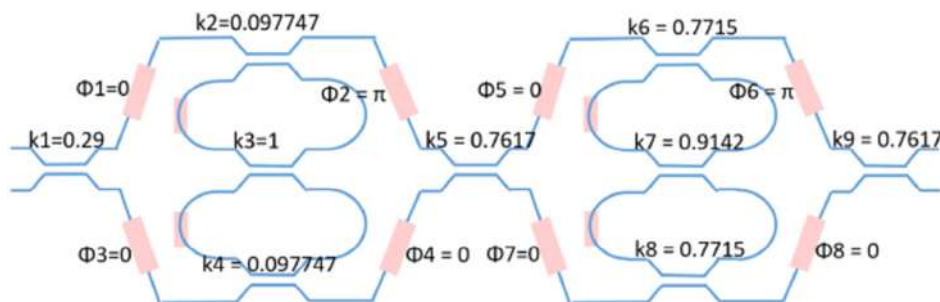


**Figure 22.** Schematic drawing of the tunable filter and the corresponding coupling and phase values to realize the elliptical filter. Reproduced with permission.<sup>[194]</sup> Copyright 2022, CC BY 4.0.

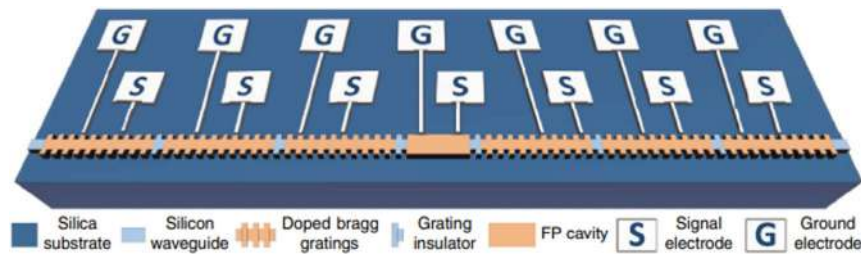


**Figure 23.** Schematic view of reconfigurable filter based on Bragg grating. The grating is made of multiple cascaded uniform Bragg grating sections and a Fabry–Perot cavity section in the middle of the structure. Each grating section is connected to an independent lateral p–n junction, and between two neighboring sections there is an un-doped grating acting as an insulator. A pair of electrodes (S: signal, and G: ground) are connected to each independent p–n junction. Reproduced with permission.<sup>[84]</sup> Copyright 2018, Nature Communications.

notch shape with a bandwidth of 6 GHz and a rejection ratio of 8.7 dB. When the device is configured as a uniform SWG, by applying a large forward bias voltage to the p–n junction, avoiding the light confinement within the defect, the reflection spectrum has a bandwidth of 88 GHz and a rejection ratio of 9.05 dB with a quasiflat shape. An overall IL of 25.1/20.6 dB has been measured at the reflection and transmission ports, respectively. A tunability of 60 GHz has been experimentally demonstrated with low-power consumption (applied voltages of tens of V). An improvement in the fabrication has led to a smaller bandwidth (3.5 GHz) with a rejection ratio of 6.4 dB.<sup>[200]</sup>

A similar configuration has been also proposed by Serafino et al. in ref. [201]. It consists of a Bragg grating with  $\lambda/4$ -long phase shifters within each grating period. The Bragg grating features, as a larger period with respect to the SWG, relax the fabrication constraints. A sharp-edge passband filtering shape, with a rejection ratio of 42 dB, IL < 5 dB, a bandwidth @ -10 dB of 75 GHz, and a tuning range of 190 GHz, although with large ripples (<4 dB) in the passband, has been obtained using a phase-shifted Bragg grating (PS-SWG). By engineering the position of defects, a notch filter with a Lorentzian shape, a bandwidth of 1 GHz, a rejection ratio >20 dB, and an IL of 30 dB has been demonstrated in ref. [202]. Moreover, Brunetti et al. numerically demonstrated in 2019 that the arrangement of the defects, according to Newton's role, along Bragg grating, which is superimposed within a part of a simple RR, leads to a Gaussian notch filter with a rejection ratio of 40 dB, a bandwidth of 10 GHz, and a tunability of the central frequency of 15 GHz via feeding p–i–n junctions corresponding defects.<sup>[66]</sup>

### 5.2.5. Stimulated Brillouin Scattering

To guarantee high-resolution filtering (tens of MHz), SBS is usually employed. This nonlinear phenomenon takes place in waveguides made of high electrostriction and EO coefficients materials. To produce this effect, it is necessary a high overlap between the acoustic and optic modes. To produce it, phonon loss, which takes place in silicon (Si) and silicon dioxide (SiO<sub>2</sub>), has to be counteracted using suspended structures or making a hybrid integration between SBS and CMOS-compatible materials. The Stokes gain in the SBS process can be exploited to realize an MWP bandpass filter, providing a broadly tunable microwave filter with a bandwidth of about 10–30 MHz,<sup>[203]</sup> although with a low-sidelobe suppression ratio (<7 dB).

To improve it, SBS filters are combined with noise cancelling filters, with a resulting sidelobe suppression ratio >20 dB.<sup>[174]</sup> The nonlinear nature of SBS provides a large tunability range (tens/hundreds of GHz) with a power consumption of hundreds of mW.<sup>[203]</sup>

Casas-Bedoya et al. proposed in ref. [204] a silicon stop-band filter with a SBS gain smaller than 1 dB. The filter performs a bandwidth of 98 MHz with a rejection ratio of 48 dB and a tunable range of 14–20 GHz by changing the frequency of the SBS pump.<sup>[204]</sup> Moreover, a photonic–photonic emitter receiver (PPER) could be exploitable as a bandpass filter with a fine spectral resolution using suspended membrane silicon waveguides (Figure 24a). The acoustic wave induced by SBS transmits the signal to the near-silicon waveguide and modulates the optical signal. The modulated optical signal produces optical sidebands that preserve the acoustic response with a resulting bandwidth of about 3 MHz and a rejection ratio of 70 dB @ 2.95 GHz (see Figure 24b).<sup>[205,206]</sup>

### 5.2.6. Programmable Photonics

Programmable photonics is a very hot topic to support the migration toward quantum networks. However, only a few experimental results have been reported on a mesh based on silicon nitride<sup>[207]</sup> and SOI<sup>[208,209]</sup> technologies. The concept behind programmable structures is the repetition in space of the same basic building block, for example, MZI, that can be enabled or not to make light passes.

Different functions can be realized through the same processor by defining the main mesh element, the kind (triangular, squared, hexagonal), the light path and the phase shifts. In particular, a waveguide mesh composed of seven hexagonal cells fabricated in SOI has been proposed in refs. [208,209] to implement over 100 different circuits. For MWP filtering applications, basic MZI, FIR transversal filters, tunable ring cavities and IIR filters, as well as compound structures such as CROWS and SCISSORS are of particular interest. Figure 25 shows, for instance, five examples of MWP FIR and IIR filters, realized using the same architecture, achieved by changing the operation state point of the different MZI elements in the mesh. The main advantage of this solution is the possibility to have in a CMOS-compatible single chip several windows needed for different applications, ensuring both flexibility and compactness. Although the bandwidth of the order of GHz has been

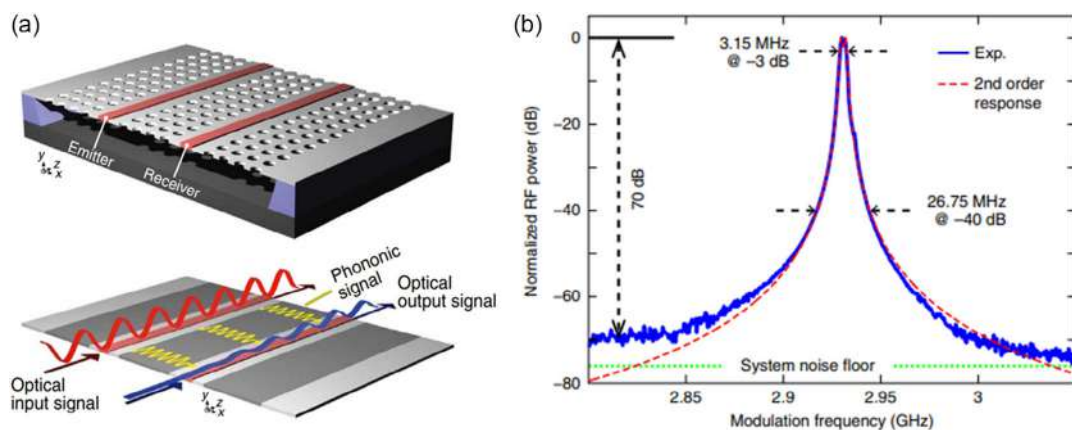


**Figure 24.** a) PPER and b) normalized RF response of a PPER system (theoretical prediction in red, experimental results in blue, system noise floor in green). Reproduced with permission.<sup>[205]</sup> Copyright 2015, CC BY 4.0.

performed, the main drawback concerns the IL (up to 20 dB) that limits its use in applications where the optical power should be preserved.<sup>[210]</sup>

### 5.2.7. Discussions on Filter Architectures for MWP

**Table 5** compares the performance of different topologies of IMWFs discussed in the previous sections. The table includes the crucial features, such as IL, bandwidth, range of tunability, rejection ratio, footprint, tuning efficiency, and the RF frequency used for the filter testing. From the table arises that RR-based devices ensure larger performance in terms of the rejection ratio (tens of dB). To achieve a more selective filter (bandwidth  $\approx$  MHz) with respect to simple RR (bandwidth  $\approx$  GHz), more complicated structures such as RAMZI, CROW, or SCISSOR are needed at the expense of a larger footprint and IL. These configurations also ensure a box-like shape. Other structures, such as SWG and SBS filters, need very long waveguides to obtain promising results. In particular, SWGs need several periods to achieve a narrow bandwidth ( $\approx$  MHz) and large rejection ratio (tens of dB), although with high IL, while SBS filters exploit a nonlinear effect that uses long travelling time through the material to perform remarkable results, as a bandwidth of MHz and rejection ratio  $>50$  dB. The tunability of all filters is strictly correlated to the tuning approach. The TO one is the most commonly applied that guarantees a simple fabrication process with a large tunability range (tens of GHz) and power consumption of hundreds of mW.

The discussion clearly indicates the potential of MWP filters in different fields. Among various filter configurations, the architectures based on microrings and microdisks are the two most used in realizing IMWPFs. Also, the on-chip SBS technology provides spectral resolution of the order to tens of MHz. The main challenge with IMWF is their poor performance with respect to RF link gain which mainly originates due to poor O-E/E-O conversion. It should be noted that the RF link gain is extremely sensitive to the losses in the photonic circuits owing to the square law of photodetection. This also deteriorates two important parameters such as noise figure and SDFR. Therefore, significant research work must be carried out to improve the IMWPF's

performance through the reduction of propagation losses as well as losses arising from fiber-to-chip coupling.

It is noteworthy that this emergent technology harbors significant potential for transformative impact across various facets of human life, promising advancements in safety, security, and operational efficiency in diverse sectors such as infrastructure and transportation.<sup>[211]</sup> The integration of MWP is anticipated to deepen, permeating various industries. One primary objective is to miniaturize complex laser systems from optical tables to board and chip levels, mirroring the historical trend observed in electronics over the past 50 years.<sup>[212]</sup> This integration is essential for fostering a comprehensive assimilation of MWP across systems. Another goal involves the development of more efficient, low-power optical sensors with higher resolutions, applicable in medical imaging, industrial safety, security, and surveillance. Photonics-based sensors offer cost-effective solutions immune to EMI and amenable to compact designs. Presently, photonics-based techniques have been employed in microwave radar measurements with a 1.5 GHz bandwidth, providing a resolution of 0.1 m.<sup>[213]</sup> However, improvements are sought to enhance sensitivity, necessitating multifunctional and multiband integration within MWP for optimal outcomes. One of the most promising breakthroughs in MWP lies in the ability to measure signals in the terahertz range with a single-shot sensor, opening a myriad of potential applications and enhancing high-frequency radar performance. Additionally, the capability to control the output frequency of photonic devices through simple pulse-by-pulse commands holds promise for applications such as array antenna beam forming and wireless power transmission in remote locations.<sup>[214]</sup> The future of MWP holds great promise and presents exciting possibilities for technological advancement.

### 5.3. Quantum Photonics Filters

Quantum photonics is an interdisciplinary field through the seamless merging of quantum mechanics and photonics which explores the quantum properties of light through the principle of superposition and entanglement of photons. In this field,

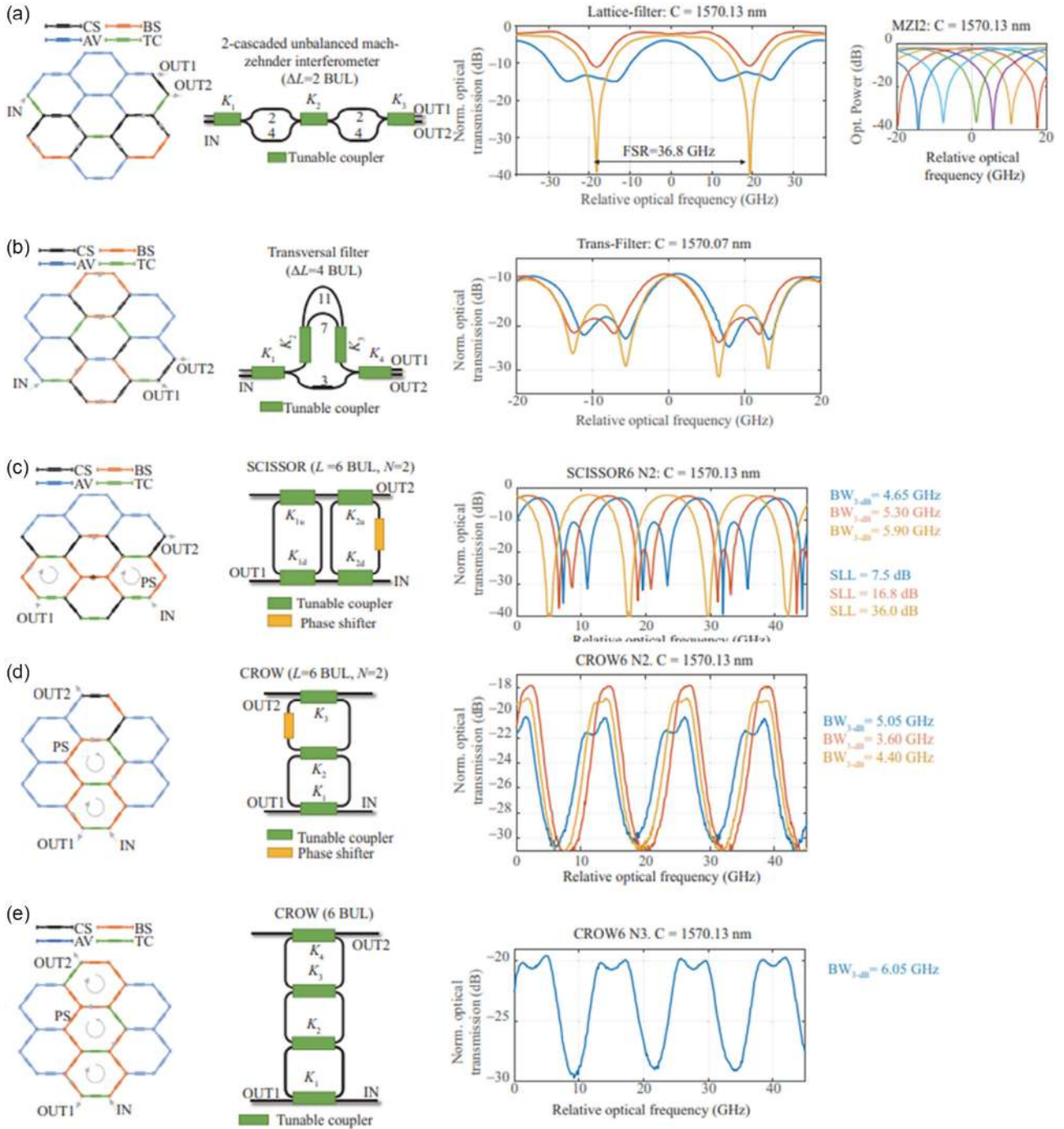


**Figure 25.** Examples of RF photonic filters using the same seven-cell hexagonal mesh. The left side shows the used basic units; the central part shows the equivalent circuit layout, the right part shows the measured spectra for the RF transfer function modules. a) Two-cascaded unbalanced 2-MZI FIR filter, b) three-tap transversal FIR filter, c) two-cavity SCISSOR FIR filter, d) two-cavity CROW filter, e) three-cavity CROW filter (CS: cross-state switch, BS: bar state switch, TC: tunable coupler, AV: available (usable)). Reproduced with permission.<sup>[208]</sup> Copyright 2017, IEEE OAPA.

researchers delve into the quantum realms of light holding multiple states. Being excellent low-noise carriers of quantum information, generation, processing, and detection of photons through integrated quantum photonics (IQP) technology can provide secure communication and help us to establish a

communication network free from classical eavesdropping techniques. Leveraging from tight light confinement in silicon photonics, photons weakly interact with the environment. This feature provides a relaxation to the requirement to operate them in ultralow temperatures or high vacuum, making them available

**Table 5.** A comparison table between different filter architectures for MWP.

	Structure	IL [dB]	Tunability [GHz]	Tuning efficiency	Rejection ratio [dB]	RF frequency [GHz]	Bandwidth [MHz]	Size [ $\mu\text{m}^2$ ]	References
RR	Cascaded pair MRRs	–	6–17	–	22	9.5	$1.65 \times 10^3$ (3-dB)	$160 \times 70$	[178]
	MRR	<14	12.4–30.6	–	60	19.32	$12 \times 10^3$ (3-dB)	$40 \times 25$	[179]
	MRR racetrack	14	2–18.4	1.14 ( $\text{GHz mW}^{-1}$ )	26.5	12.2	170 (3-dB)	$5 \times 10^4$	[182]
	N-SCISSOR	9	2.75–10.25	–	25	7.5	1.8 (3-dB)	$7 \times 1.25 \times 10^6$	[191]
	CROW	<0.5	–	31 ( $\text{mW nm}^{-1}$ )	11	1565	950 (3-dB)	$4 \times 2 \times 10^6$	[189]
SWG	SWG	–	–	–	15	–	$50 \times 10^3$ (3-dB)	$65 \times 4 \times 10^3$	[199]
	PS-SWG	20.6	30	–	8.7	–	62 (3-dB)	$3 \times 10^5$	[169]
	EPS-SWG	15	30	17–48 ( $\text{pm mW}^{-1}$ )	6.4	–	$3.5 \times 10^3$ (3-dB)	$8 \times 10^5$	[200]
	SWG	20.6	–	–	9.05	–	90 (3-dB)	$3 \times 10^5$	[169]
	SWG	5	0–20	–	20	–	1000 (3-dB)	$6 \times 500 \times 10^3$	[202]
	PS-SWG	–	250	–	41.5	–	$75 \times 10^3$ (10-dB)	$450 \times 0.522$	[201]
RAMZI	Double ring RAMZI	–	–	20 ( $\text{mW } \pi^{-1}$ )	60	–	250 (3-dB)	–	[194]
	RAMZI	<15	4–36	–	60	24	780 (3-dB)	$500 \times 200$	[196]
	RAMZI	–	0–40	–	50	20	–	$700 \times 400$	[186]
	Cascaded RAMZI	1	735	–	25	–	$120 \times 10^3$ (3-dB)	–	[197]
	RAMZI	25	–	–	78	–	860 (3-dB)	$630 \times 310$	[195]
SBS	SBS	–	14–20	–	48	15.7	98 (3-dB)	$480 \times 12.5$	[204]
	PPER	15	–	–	70	2.95	3.15 (3-dB)	$64.8 \times 4 \times 10^3$	[205]

for real-world application. Moreover, with the advancement of on-chip laser sources and detectors, and the possibility of hybrid integration, in recent years, IQP has shown tremendous growth with silicon photonics architecture.<sup>[215,216]</sup> Since the realization of on-chip quantum interference in 2008,<sup>[217]</sup> quantum photonics has shown a steady and commendable growth toward large-scale integration. Given this, IQP has gained much attention in recent times and has been intensively investigated in different fields like quantum key distribution,<sup>[218]</sup> quantum signal processing,<sup>[219]</sup> quantum sensing,<sup>[220]</sup> etc.

### 5.3.1. Pump Rejection Filters

In any large-scale PIC, entangled photon sources are the primary requirements. The photon pairs can be generated through spontaneous four-wave mixing (SFWM) by pumping a nonlinear medium through a strong laser field. The guided pump laser light ( $\omega_p$ ) generates two correlated photon pairs known as signal ( $\omega_s$ ) and idler ( $\omega_i$ ). In this setup, it is important to drop the residue of the pump laser light through a bandstop filter with a high ER, narrow bandwidth, and low loss. To accomplish this, different filter architectures have been reported in recent times including MZI,<sup>[221]</sup> WBGs,<sup>[222,223]</sup> as well as CROWs.<sup>[224–226]</sup>

Harries et al. reported an on-chip photon pair generation and rejection of pump light through MRRs and a distributed Bragg reflector, the schematic of which is illustrated in **Figure 26a**.<sup>[227]</sup>

The high-Q thermally tunable MRR having a radius of  $15 \mu\text{m}$  is used for efficient generation of the signal-idler pair, whereas the DBR is used to drop the pump light. Two additional MRRs at the output are used to demultiplex the signal and the idler photon. **Figure 26b** also includes the throughput spectrum of the first

MRR where the generation is taking place. When the MRR is tuned at the pump frequency, the photon pairs generated at the resonance wavelengths are spaced equally as the FSR. **Figure 26c** represents the transmission spectrum having a stop band overlapping with the pump and thus blocking the pump while passes the signal and idler. Finally, the two MRRs are tuned to drop the signal and idler photons, as shown in **Figure 26d**. The DBR produced a pump rejection of 65 dB, which has been further enhanced to 100 dB with the help of tunable add-drop MRRs at the output end.

A cascaded geometry of MZI with unbalanced arms is used by Piekarek et al. to achieve an ER > 100 dB.<sup>[221]</sup> The structure consists of two dies with one chip containing six cascaded MZIs and the other one containing four cascaded MZIs. To overlap the spectrum of two dies, accurately thermal tuning principle is used. However, it also requires accurate control in the one-step fabrication process, making it difficult for mass production. Utilizing the large suppression ratio of MZI in addition to the highly selective nature of MRR, an extraordinarily high ER of 150.55 dB has been numerically achieved by Brunetti et al. in ref. [226]. The schematic diagram of the proposed structure is shown in **Figure 27a**. It consists of a single MZI with two MMI couplers at the input and output sections. One arm of the MZI is coupled with an MRR, whereas the other arm is coupled with three serially coupled MRRs forming the CROW structure. **Figure 27b** shows the transmission spectrum with ring radii of  $15 \mu\text{m}$ . The spectrum shows a high ER of 150.55 dB with a bandwidth of 0.243 nm and IL of 0.104 dB. Heaters are placed on top of each ring to effectively tune the position of the resonance position with a maximum detuning of 6 MHz to bring flexibility to the structure. To minimize the effects of heating on the coupling efficiency, the heaters are placed outside the coupling regions.

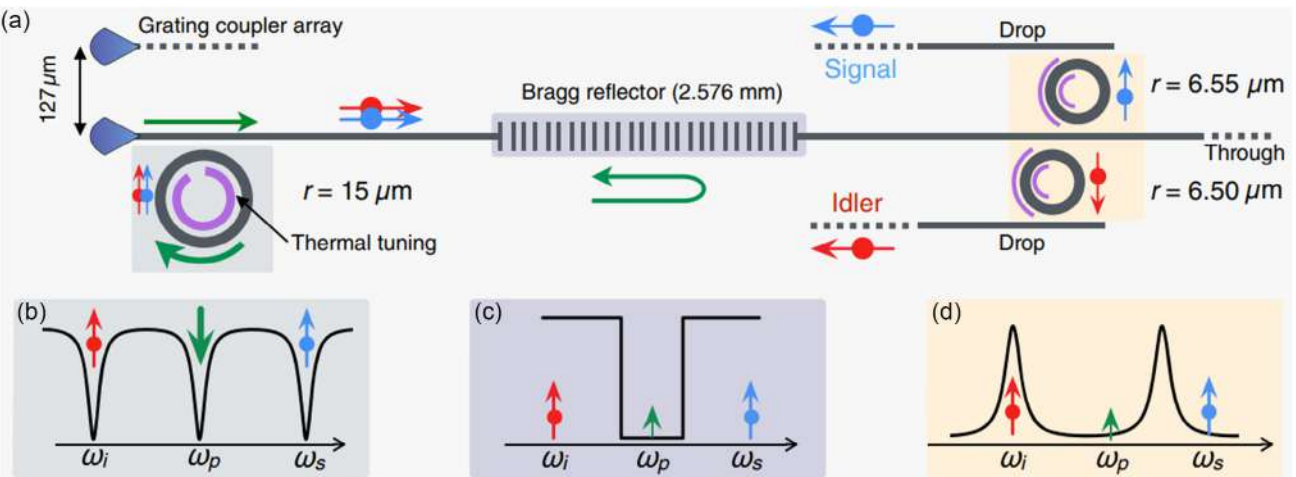


**Figure 26.** a) Schematic layout of an on-chip generation of signal-idler pair, dropping of the pump light and demultiplexing of the signal and idler, b) idler (red), pump (green), and signal (blue) signals, c) filtering shape at a central frequency  $\omega_p$ , and d) resulting spectra after filtering. Reproduced with permission.<sup>[227]</sup> Copyright 2014, CC BY 3.0.

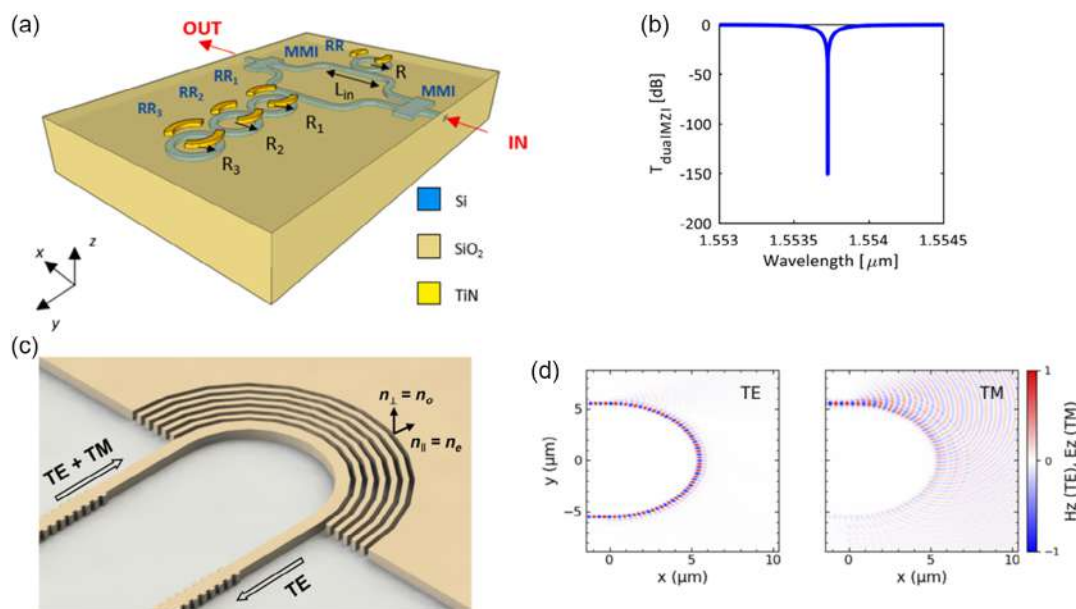


**Figure 27.** a) Schematics of the pump rejection filter having a high ER consisting of MZI and coupled MRRs, with b) the related spectrum. Reproduced with permission.<sup>[226]</sup> Copyright 2021, Optics and Laser Technology. c) Configuration of polarization-selective structure and d) corresponding view of TE and TM mode propagation at 1550 nm. Reproduced with permission.<sup>[228]</sup> Copyright 2022, Optics Letters.

Polarization diversity is a critical issue to push the increased performance of silicon PIC to further miniaturization. Recently, Michon et al. reported an innovative technique to overcome this problem.<sup>[228]</sup> The structure is illustrated in Figure 27c, made of modal-engineered Bragg grating which provides high rejection to the TE mode whereas anisotropy-engineered metamaterial bends remove any residual power propagating with the TM modes. Figure 27d shows the light propagation associated with the TE and TM modes, reflecting the lossy nature of the TM mode in the metamaterial bending section. The proposed structure shows a good ER of 60 dB associated with the TE mode.

### 5.3.2. Silicon Photonics in Entangled Photon Generation and Processing

The above analysis is focused on the suppression of pump power through high ER filters. This section focuses on the formation of entanglement through the generated signal-idler pair in the silicon photonic architectures. Entanglement in the context of quantum photonics refers to the correlations between two or more photons within the integrated optical waveguide geometry, which plays a pivotal role in different fields like quantum communications, computing, teleportation, cryptography, quantum imaging

and sensing, etc. Depending upon the states/modes of the photons the versatile platform of quantum photonics paves the way for forming different types of entanglements such as polarization, time-bin, frequency-bin, energy-time, path, spatial entanglement, etc. Among the various entanglement techniques, polarization entanglement<sup>[229–231]</sup> is the most widely used technique especially in free space applications whereas path entanglement has become a popular choice in on-chip quantum information processing. In the path entanglement technique, which correlates the spatial paths of the photons, silicon photonics has shown immense potential. Due to the strong third-order nonlinearity ( $\chi^3$ ) in silicon, photon pair generation through SFWM is relatively easy in silicon waveguides; as a result, various silicon photonic circuits have been generated in recent times in which filters play a pivotal role.<sup>[232,233]</sup> However, the integration of all components including source, generation, processing, and detection in a single chip is still a challenge. Silverstone et al. proposed a SOI device with two SFWM sources having an interferometer with a phase shifter to create and manipulate degenerate and nondegenerate path-unentangled and path-entangled photon pairs.<sup>[234]</sup> In this device, the coupling between the bright pump power and SOI chip took place through a lensed optical fiber. Next, the pump distribution and single-photon manipulation have been accomplished with  $2 \times 2$  MMI, whereas the generation of signal-idler took place through a 5.2 mm-long spiral silicon waveguide in each arm. Further, the phase shifters manipulate the quantum state, and another  $2 \times 2$  MMI coupler at the end either bunches or splits the two-output state depending on the induced phase shift. The process took place over a 1 mm-long SOI chip but the off-chip WDM filters were used to separate the signal, idler, and pump before measurement. In another study made by the same group, the generation of path entangled photons, their processing, and the analysis of the entangled photons are carried out in a scalable silicon photonic chip, as shown in **Figure 28**.<sup>[235]</sup> In this architecture, the SOI chip operates in a telecommunication band able to generate and process the path-entangled photons from two coherently pumped photon-pair sources. It is to note that unlike a spiral waveguide here, the photon pair generation took place in two MRRs. A picosecond pump laser source having frequency  $\nu_p$  is coupled into the silicon chip generating the two photon pairs at two adjacent resonance wavelengths ( $\nu_p \pm 800$  GHz) having a cavity linewidth of 21 GHz. It is

to be noted that the pump source used here has a 10.8 ps pulse with a linewidth of 40 GHz. The average pump power is  $150 \mu\text{W}$  with a peak power of 253 mW which generates 0.06 and 0.09 probabilistic photon pairs. Next, each photon pair is demultiplexed by double-bus MRRs and separated into a signal (blue) and an idler (red) path qubits. Each MRR filter is designed to select the signal while maximally rejecting the idler. The superimposed signal and idler path qubits are next analyzed by the two MZIs with TO heaters before detection. However, in this structure also, the fiber-based WDM filters are used to separate residual pump power before detection. In a single-silicon chip, Santagati et al. demonstrated a switchable entangling gate to produce a range of separable and entangled quantum states through the principle of path entanglement.<sup>[236]</sup> In the architecture, they used four photon-pair sources and a six-mode reconfigurable interferometer in a scalable and mass-reproducible geometry. Recently, Zhang et al. experimentally showed a pathway to realize all integrated silicon photonic path entanglement structures with the help of on-chip high-speed germanium photodiodes.<sup>[237]</sup>

Besides path entanglement, time-bin entanglement through silicon photonic architecture also has gained much attention in the last decades or so.<sup>[238–240]</sup> Although the time-bin entanglement is extremely resilient to the phase fluctuations originating due to external parameters like thermal variations, controlling the quantum state of the photons at which the entanglement is generated is extremely difficult. On the other hand, the polarization and path entangled suffer highly from thermal fluctuations. In this context, frequency bin entanglements in which the frequencies of the signal and idler photons are entangled have proven to be a promising alternative in recent times. It shows a stable performance with respect to amplitude variation as well. As a result, pioneering work has been carried out by different groups in the generation and manipulation of frequency bin-entangled photons through integrated resonators.<sup>[241–245]</sup> It is noteworthy to mention that the MRR architectures are found to be the most suitable ones for generating entangled photon pairs as the cavity structures provide an enhancement in generating the photon pair as well as offer a narrower bandwidth.<sup>[246,247]</sup> Utilizing SOI MRR Chen et al. reported 21 pairwise correlated peaks over a wavelength range of 1.3–1.8  $\mu\text{m}$ . In frequency bin, there exists a trade-off between the generation rate and the bin separation and thus the number of accessible

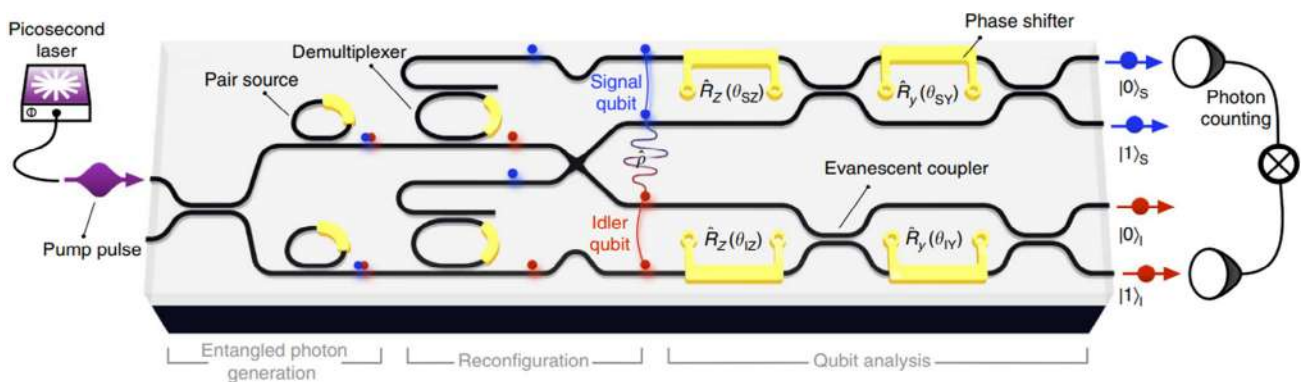


**Figure 28.** Schematic of the silicon photonic chip for the generation of entangled photon pair, their superposition, and analysis of the generated qubits. Reproduced with permission.<sup>[235]</sup> Copyright 2015, CC BY 4.0.

frequency bin/states. This can be attributed to the requirement of an off-chip commercially available EO modulator which has limited bandwidth. As a result, the separation between the frequency bins cannot exceed a few tens of gigahertz. This limits the generation rate as the efficiency of SPWM scales quadratically with the FSR of the MRRs.<sup>[248]</sup> To overcome these, various approaches have been proposed in the past few years.<sup>[242,245]</sup> In one of them, researchers have realized different states piece-by-piece by selectively and coherently pumping multiple MRR-based filters with the help of MZI and bus waveguide architecture which eliminates the requirement for off-chip modulators.<sup>[245]</sup>

Leveraging from hybrid integration, Mahmudlu et al. reported an on-chip high-dimensional frequency bin-entangled states by merging the InP platform to silicon waveguide architectures, as shown in **Figure 29**.<sup>[243]</sup> The structure consists of an electrically pumped reflective semiconductor optical amplifier generating an optical gain profile shown at the topleft corner of Figure 29.

The laser cavity is formed through a reflective coating at the amplifier side and a Sagnac mirror on the other side. Followed by the amplifier medium, three MRRs having different radii form a Vernier filter which can be tuned by controlling the microheaters placed on top of each MRR. The Vernier effect through the MRRs enables a strong noise suppression >55 dB. The backward signal excites the SFWM in the third ring (R3) and generates the frequency bin quantum states. Although silicon photonics is a

relatively new addition in the quantum domain, it holds an immense potential to become a mature technology and pave the way toward large-scale commercialization.

### 5.3.3. Discussions on Filter Architectures for Quantum Photonics

The quantum photonic section focuses on different approaches to achieve a high ER bandstop filter to drop the unused pump power and generation of entanglement between the signal-idler pair. It has been observed that the high ER, narrow bandwidth, and low-loss filter are equally important for the quantum photonic application. The initial part of this section includes a basic description of dropping and separating the pump and generated signal-idler pair through nonlinear effects, respectively, by combining MRR and distributed WBG geometry. To drop the unused pump power, the highest experimentally reported ER is found to be 100 dB, whereas a theoretical ER as high as 155 dB is achieved with a narrowband response. It has been also observed that silicon photonic components like MRRs and MZIs also play a pivotal role in the generation of different forms of entanglement between the signal-idler pair. The formation of different entanglements like path, time-bin, and frequency-bin is discussed briefly emphasizing the role of silicon photonic filters. Due to the various advantages of silicon photonics, filters are a hot and open topic to carry forward the research activity in the field of quantum photonics as well.

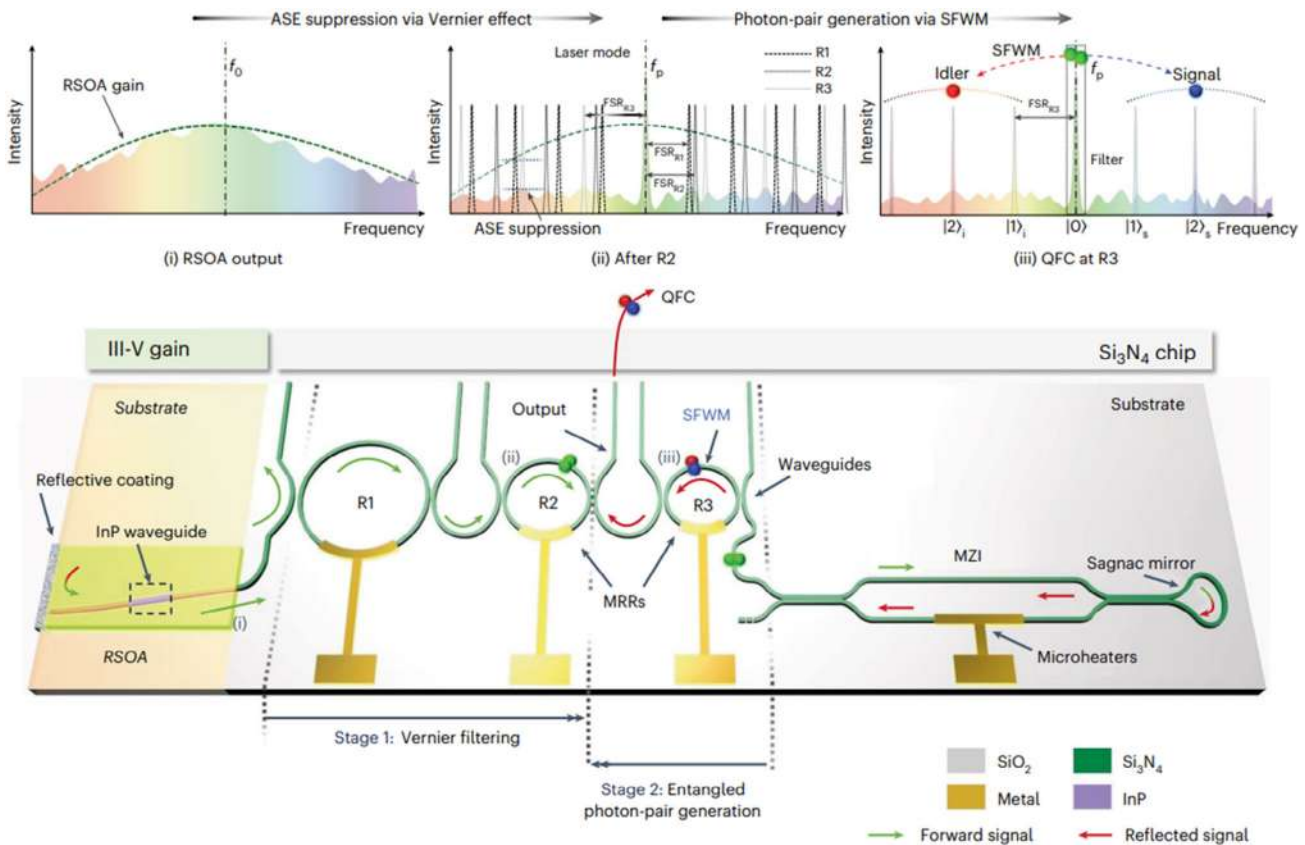


**Figure 29.** Schematic of the laser-IQP source with frequency bin-entangled photon pair in a hybrid integrated chip. Reproduced with permission.<sup>[243]</sup> Copyright 2023, Nature Photonics.

Silicon photonics possesses immense potential for quantum photonics due to its multifunctionality, strong third-order non-linearity, tight light guidance, small footprint due to large index contrast, etc. To sustain its growth and large-scale commercialization for real-world applications, silicon photonics still has to overcome multiple key challenges. One of them is the propagation loss. Although high-index contrast furnishes strong light confinement, it also makes it vulnerable to sidewall roughness, demanding a loss-tolerance approach. Normally, the propagation loss in silicon waveguides is  $2 \text{ dB cm}^{-1}$ , which can be significantly reduced by emerging fabrication technologies like etchless fabrication, oxidation, hydrogen thermal annealing, etc.<sup>[249–251]</sup> Instead of single-mode operation, tapering to the multimode waveguide can be one solution, but it also brings noises arising from multimode interference. Hybrid integration of silicon waveguides with different materials like silicon nitride and wedge silica with small angles can also reduce the losses to  $<0.1 \text{ dB m}^{-1}$ .<sup>[252]</sup> Another major source of loss in silicon is two-photon absorption (TPA). This limits the strength of the pump in the near-IR telecommunication band, where SFWM occurs. Recent approaches also attempt to operate at longer wavelengths, which significantly reduce the propagation losses associated with the TPA mechanism.<sup>[252]</sup> However, this also demands the development of the supporting infrastructure at the longer wavelength, which remains to be a challenge.

It is to be noted that, in the on-chip generation of pure and deterministic single photons, photo-pair plays a crucial role in quantum photonics, especially for large-scale quantum photonic circuits where a repeatable large number of identical photon sources is very important. An array of 4 SWFM sources is realized in silicon having a purity of around 95% showing its promise toward large-scale integration.<sup>[253]</sup> Recently, S. Paesani et al. reported single-photon sources in silicon with improved purity of 99.04%. However, the array number is still lower than low-index waveguides like  $\text{SiO}_2$  where 18 array of SWFM base sources are reported with purity of 97%.<sup>[254]</sup> An important issue although is that production of photons in silicon is the less deterministic nature since the probability is around 5–10%. Time and spatial multiplexing techniques can help overcome this issue.<sup>[255–257]</sup> In silicon, the  $\chi^{(3)}$  effect is normally used for such purpose. However, the  $\chi^{(3)}$  effect is weaker than  $\chi^{(2)}$  effect (absent in silicon) or the quantum dot technique. Designing a high

Q-factor filter can play an important role since the photon pair generation is nearly proportional to the third power of the Q-factor.<sup>[257]</sup> Besides the source, the reliability of quantum photonics also depends on its integration capability with a single-photon detector. In recent times, significant growth has been achieved with transition edge sensors, fully integrable superconducting nanowire detectors based on Si itself or hybrid integration with GaAs or  $\text{Si}_3\text{N}_4$ . The problem is such detectors normally operate at cryogenic temperatures. A significant research focus is given in developing such detectors close to room temperature.<sup>[258]</sup> Some recent developments like avalanche photodiode with germanium in silicon operating around 80 K have shown some promise in this direction. The on-chip detection efficiency of such detectors has shown a tremendous growth from 5.27%<sup>[259]</sup> to around 38%<sup>[259,260]</sup> within the past few years. However, significant research work is still required to improve the detection efficiency of such room-temperature detectors.

The real-world application of quantum photonics also needs to overcome the challenges associated with electronic–photonic integration. Often it is required that photonic circuits are integrated with electronic components for the control, power supply, as well as I/O to the classical domain. Since the quantum states are highly vulnerable to any external perturbations, integration with electronics makes it challenging to keep the photonic circuits immune to EMI, demanding its shielding. A significant research effort has been also recently given in 3D wafer technology to merge photonics and electronics in a compact geometry.<sup>[261]</sup> Overall, the above discussion shows the immense potential of silicon-based quantum photonics, its integration challenges, as well as its promises and future perspectives for large-scale quantum photonic circuits. Recent developments have shown the potential of quantum photonics in creating long-distance space-to-ground secure communication over distances of more than a thousand kilometres<sup>[262,263]</sup> through satellite links in which silicon photonics can play a crucial role in the near future.

## 6. Silicon Photonics Market

Due to their various advantages besides academic areas, silicon photonics has seen astonishing growth in the global market recently. There are several factors contributing to the growth of the silicon photonics market. These include compatibility with existing fabrication technologies and integrability with electronic components in the same platform, aspects that ensure compact and cost-effective devices. Moreover, silicon photonics enables signal processing at the speed of light and high-bandwidth operation, which are essential factors for high-capacity data processing and high data transfer rates that bring added value to the data centers and telecommunication sectors, along with low power consumption. In addition, miniaturization capability and immunity to EM interference, which reduce the requirement for shielding, are further aspects that make silicon photonics attractive for space applications, with increasing investment from both government and private initiatives and collaborations between the semiconductor industry, research institutes, and various companies. In the early days since its invention in the middle of the 1980 s, silicon photonics does not catch much attention towards commercialization. Two important milestones in silicon photonics are the invention of low-loss silicon waveguides at sub-micrometer scale in the late 1990 s and the significant advancement of microfabrication technology reaching linewidth  $\approx 100 \text{ nm}$  in the early 2000 s. These gave a boost to the research in silicon photonics, and it started to gain market attention in the late 2000 s which is reflected from Figure 2 shown in the Introduction of this paper. After the release of the first optical transceiver with silicon photonics by Luxtera (now known as Cisco), the market interest started to grow. A landmark moment that reflects the growing interest in silicon photonics took place in 2012 when Cisco purchased Lightwire, a startup specialized in optical interconnects. A true acceleration began in 2018 when companies like Cisco, Huawei, and others observed a marked increase in sales of silicon photonic-based transceivers. In 2020, Intel developed 100 Gbps 4-channel CWDM transceivers with low power consumption (around 4 W) and extended

temperature range from  $-40$  to  $85$  °C marked as an important milestone in silicon photonics market development. According to the reports published in ref. [264], the global silicon photonics market at present mostly focuses on telecommunications, data centers, and high-performance computing, military, defense, aerospace, etc. In 2022, the silicon photonics market stood at 1.3 billion USD, and it is predicted to reach 5 billion USD by the end of 2028 with a compound annual growth rate (CAGR) of 28.5% (see Figure 29).<sup>[265]</sup> Figure 30 shows the predicted growth rate and provides the region-wise growth of the silicon photonics market. It is estimated that the growth rate will be maximum in Asian-specific areas driven by a high number of internet users. The potential of the silicon photonics market resulted in gaining interest as well as the formation of various companies such as Intel corporation, Cisco system, MACOM technology

solutions, Lumentum operations, Marvel technology, etc. Among these companies, Intel and Cisco hold the highest market share with 58% and 29% in units according to the Yolegroup.<sup>[20]</sup> In Figure 31 geography-wise companies are represented to provide an overview of leading market players, as reported very recently by IDTechEx.<sup>[266]</sup>

The primary silicon photonics market is centered around optical communication mainly due to the rising demand for data centers in which WDM filters play a crucial role. It is estimated that among products the transceivers will share the highest growth rate. Since its first launch in 2016, Intel is still the industry leader for transceivers. The various companies presented in Figure 30 are the pilot lines to carry out the research activities in different institutes whereas few are fully commercial companies from foundries to delivering the final product. These foundries

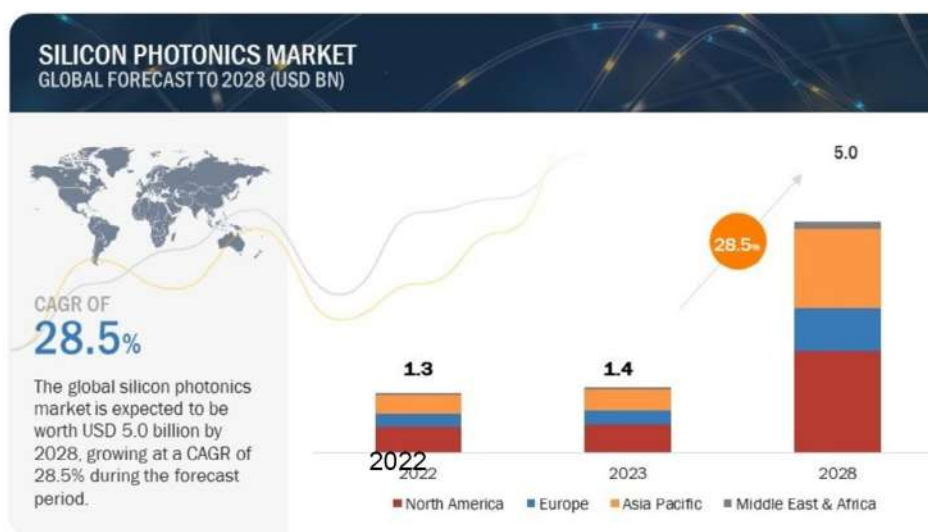


Figure 30. Market growth of silicon photonics.<sup>[265]</sup>



Figure 31. Different supply chains of silicon photonics and hybrid-silicon photonic components/systems by geography.<sup>[266]</sup>

provide multi-project wafers, process design kits and volume, and/or customized production to carry forward the research work and industrialization.<sup>[2,3]</sup>

Besides optical communications, silicon photonics has started to put its mark in domains like MWP. Being an emerging technology, major players that compile market research reports, such as Yole, Markets and Markets, Research and Markets, and Transparency Market Research, have not yet included MWP in their major market trends. However, it is explicitly stated that such new technologies can bring benefits to the defense, telecommunications, and computing sectors. In **Figure 32** a summary of different companies that developing MWP circuits is shown<sup>[267]</sup> which includes companies designing basic components, developing MWP modules, as well as packaging. A prominent application of MWP is observed in the domain of medical imaging, wherein it harnesses terahertz waves to generate high-quality, frequency-tunable images. This application offers distinct advantages over conventional methods, including X-rays and nuclear magnetic resonance, by providing superior imaging capabilities and essential spectroscopic information often absent in optical and X-ray modalities (MWP GmbH, Philips). Furthermore, MWP plays a pivotal role in communications, offering a promising avenue for telecommunications by enabling signal transmission over extensive bandwidths. To meet the demands of applications in medical imaging and communications, devices must exhibit characteristics such as high speed, wide bandwidth, low-power consumption, tunability, and resilience to EMI, making photonics an increasingly favored solution over digital electronics (iPronics, Miraex, Hamamatsu). Beyond medical imaging and communications, MWP finds applications in diverse fields, including military technology, medical technology, diagnostics, space communications, and sensing (MWP4SPACE, AirBus). Its utility extends to enhancing

the efficiency of high-powered lasers, achieved through minimizing losses in the gain medium and optimizing coupling efficiency to external cavities (OSRAM). Furthermore, MWP contributes to noise reduction in pump lasers using resonators to filter time-independent noise. The MWP market emphasizing silicon photonics also has started to grow in the wireless communication domain due to its superiority over conventional electronic counterparts.<sup>[268]</sup>

As shown in **Figure 33**, the quantum photonics market is expected to grow from 0.4 billion in 2023 to 3.3 billion USD in 2030 with a CAGR of 32.2%.<sup>[269]</sup> The main driving force behind the market growth of quantum photonics is secure communication and quantum photonics computing. During the forecast period, the Asian-specific market is expected to grow at the highest rate and the largest market share is held by the quantum computation segment. Given that companies like Toshiba from Japan, Xanadu from China, ID Quantique from Switzerland, and Quandela from France are developing a competitive ecosystem to drive investment in research and development to build highly reliable and efficient quantum systems, it is noted that quantum computing is gaining great attention in which quantum photonics can play a crucial role since photonic quantum computers can perform at room temperature. As a result, several companies like Xanadu Quantum Technologies, ORCA Computing, PsiQuantum, Quandela, and Quix Quantum have shown great interest in recent times.<sup>[270]</sup> Recently PsiQuantum has raised USD 450 million to build a commercial quantum computer,<sup>[271]</sup> which makes it one of the largest independent Quantum Technology companies. It is projected that the quantum computation market will grow at a CAGR of 19.6% from 2023 to 2030.<sup>[272]</sup> The growth of the quantum communication market is even higher with a CAGR of 29.3%.<sup>[273]</sup> Its market will grow from USD 0.82 billion in 2023 to USD 8.3 billion by 2032.

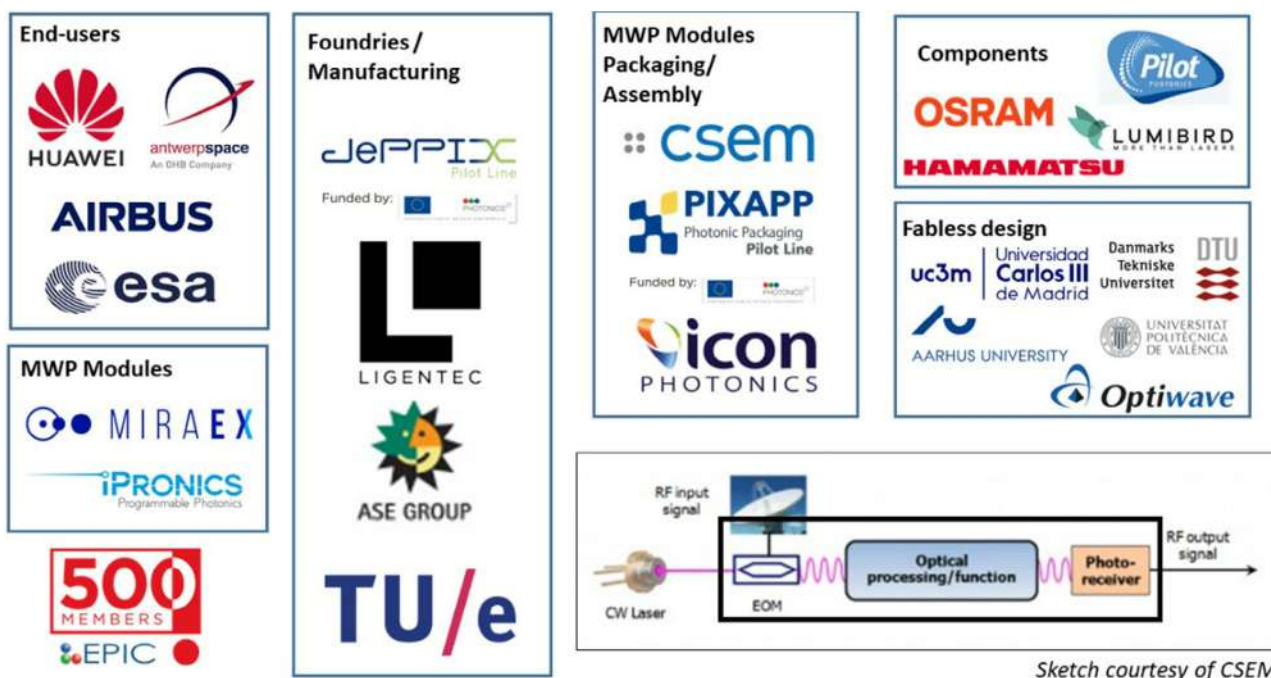


**Figure 32.** Supply chain of MWP-based components/systems. Reproduced with permission.<sup>[267]</sup> Copyright 2020, CSEM.

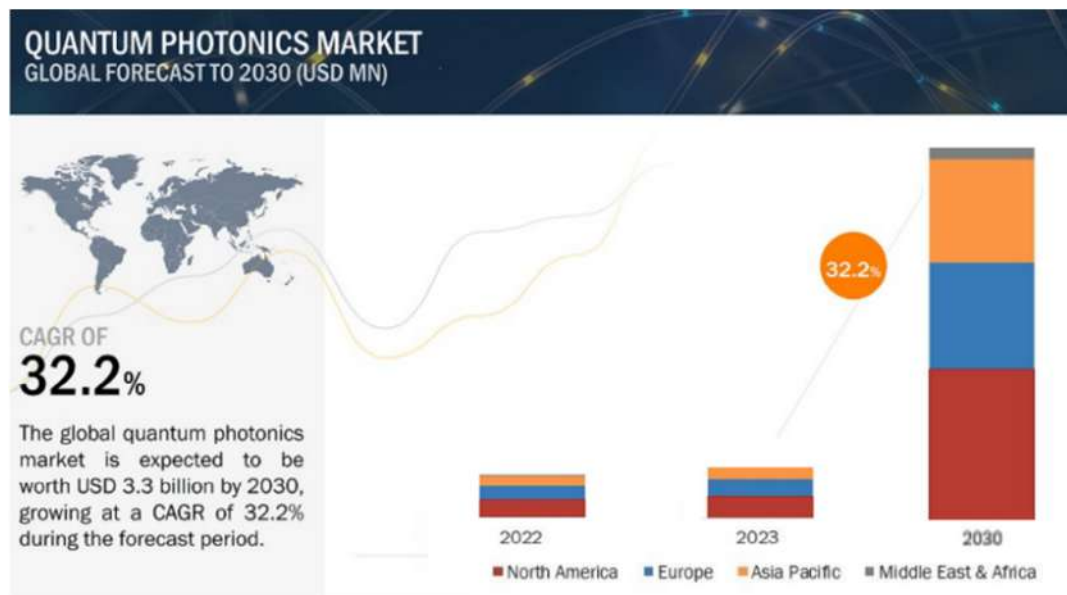


**Figure 33.** Market growth of quantum photonics.<sup>[269]</sup>

The major players in the quantum communication market include AmberFlux, Atos, Fujitsu, Toshiba, MagiQ, NEC Corporation, Mitsubishi etc. It is expected that the banking and finance sector will dominate the quantum photonics market during the predicted period due to real-time data analyses, preventing fraud, financial transactions through more secure encryption, etc. Besides quantum photonics is predicted to play a crucial role in sectors like healthcare, defense, transportation, etc.

## 7. Conclusions and Discussions

In summary, a comprehensive review of silicon photonic filters based on MRR, WBG, MZI, and AWGs is presented with their applications in optical communications, microwave, and quantum photonics. The initial part of the review discussed the basics of silicon photonics with the four most favorable filter architectures and a guideline to simulate these filters and realize reconfigurability. The developing trend of the different silicon photonic filters in an application-specific manner has been discussed. The optical communication section provides details about different filters with applications targeting the CWDM and DWDM/demultiplexing. It is important to note that WBG naturally provides a flat top band with sharp roll-off, making it particularly promising for WDM technology. In addition, the cascaded structure can increase the number of channels as well as provide the possibility of simultaneous tuning of central wavelength as well as the passing bandwidth. However, with WBG it is particularly challenging to achieve narrow bandwidth as it requires extremely small grating teeth to reduce the coupling coefficient which is difficult from a fabrication point of view. This feature hinders WBG's application in the DWDM system. The MZI and MRR-based structure cannot provide a flat top response in general. However, the cascaded geometry is capable of providing a flat top response with MZI and MRRs. Among all the

geometry, the smallest footprint can be achieved with MRR-based architectures due to their circular geometry. Therefore, with MRRs, it is possible to realize a low-power consumable flexible WDM system. For MZI and MRRs the main source of concern is the FSR as the number of channels is often limited by it. It has been observed that for a large number of channels, AWGs are particularly promising and usually preferred. Due to their large footprint, AWGs usually require large power consumption, hindering their application in flexible WDM systems. In addition, this section also includes the different approaches proposed by different research groups to realize polarization-insensitive and fabrication-tolerant silicon photonic filters which can significantly reduce the crosstalks between different channels as well as the IL. This section points out the importance of carrying forward the research work in silicon photonic filters which can simultaneously provide a flat-top response, sharp roll-off, low power consumption, polarization insensitivity, as well as great fabrication tolerance. The MWP section takes a portrait of different approaches to perform various kinds of filters with a large rejection ratio, tunable central frequency, small footprint, and desirable bandwidth according to the RF target application. The large tunability of MWP filters paves the way for their use in several applications, such as Space and telecom payloads, to obtain flexible structures able to be reconfigured according to the user demands. The quantum photonic section focuses on different approaches to achieve a narrow bandstop filter with a high ER which is important to drop the pump laser source. It is observed that among the four filter architectures, AWGs are found to be more suitable for dense WDM operations. The WBGs and MRRs can provide great flexibility in realizing tuning in terms of central wavelength as well as bandwidth. This makes it suitable for flexible WDM technology. The possibility of realizing reconfigurability makes them suitable for MWP where signal processing is required over a very small bandwidth. For quantum photonics, MRRs are found to be the dominating

one since the cavity structures provide an enhancement in generating the photon pair, which plays a crucial role.

We believe that the state-of-the-art analysis presented in this article can significantly help in understanding and advancing the research and industrial development of silicon photonics.

## Acknowledgements

This work was partially supported by the European Union under the Italian National Recovery and Resilience Plan (NRRP) of Next Generation EU, a partnership on “Telecommunications of the Future” (PE00000001 - program “RESTART”).

## Conflict of Interest

The authors declare no conflict of interest.

## Keywords

arrayed waveguide gratings, filters, Mach–Zehnder interferometers, microwave photonics, quantum photonics, ring resonators, silicon photonics

Received: January 15, 2024

Revised: March 12, 2024

Published online: March 30, 2024

- [1] R. Soref, J. Lorenzo, *IEEE J. Quantum Electron.* **1986**, *22*, 873.
- [2] A. E.-J. Lim, J. Song, Q. Fang, C. Li, X. Tu, N. Duan, K. K. Chen, R. P.-C. Tern, T.-Y. Liow, *IEEE J. Sel. Top. Quantum Electron.* **2014**, *20*, 405.
- [3] S. Y. Siew, B. Li, F. Gao, H. Y. Zheng, W. Zhang, P. Guo, S. W. Xie, A. Song, B. Dong, L. W. Luo, C. Li, X. Luo, G.-Q. Lo, *J. Lightwave Technol.* **2021**, *39*, 4374.
- [4] M. Lipson, *J. Lightwave Technol.* **2005**, *23*, 4222.
- [5] D. Liang, J. E. Bowers, *Light: Adv. Manuf.* **2021**, *2*, 59.
- [6] G.-H. Duan, C. Jany, A. L. Liepvre, A. Accard, M. Lamponi, D. Make, P. Kaspar, G. Levaufre, N. Girard, F. Lelarge, J.-M. Fedeli, A. Descos, B. Ben Bakir, S. Messaoudene, D. Bordel, S. Menezo, G. de Valicourt, S. Keyvaninia, G. Roelkens, D. Van Thourhout, D. J. Thomson, F. Y. Gardes, G. T. Reed, *IEEE J. Sel. Top. Quantum Electron.* **2014**, *20*, 158.
- [7] W. Yang, Y. Li, F. Meng, H. Yu, M. Wang, P. Wang, G. Luo, X. Zhou, J. Pan, *J. Semicond.* **2019**, *40*, 101305.
- [8] P. Wen, P. Tiwari, S. Mauthe, H. Schmid, M. Sousa, M. Scherrer, M. Baumann, B. I. Bitachon, J. Leuthold, B. Gotsmann, K. E. Moselund, *Nat. Commun.* **2022**, *13*, 909.
- [9] S. Cho, J. Park, H. Kim, R. Sinclair, B.-G. Park, J. S. Harris, *Photonics Nanostruct.* **2014**, *12*, 54.
- [10] S. Saito, F. Y. Gardes, A. Z. Al-Attili, K. Tani, K. Oda, Y. Suwa, T. Ido, Y. Ishikawa, S. Kako, S. Iwamoto, Y. Arakawa, *Front. Mater.* **2014**, *1*, 15.
- [11] K. Mirabbas Kiani, H. C. Frankis, C. M. Naraine, D. B. Bonneville, A. P. Knights, J. D. B. Bradley, *Laser Photonics Rev.* **2022**, *16*, 2100348.
- [12] H. Isshiki, F. Jing, T. Sato, T. Nakajima, T. Kimura, *Photonics Res.* **2014**, *2*, A45.
- [13] J. Komma, C. Schwarz, G. Hofmann, D. Heinert, R. Nawrodt, *Appl. Phys. Lett.* **2012**, *101*, 041905.
- [14] R. Soref, B. Bennett, *IEEE J. Quantum Electron.* **1987**, *23*, 123.
- [15] A. W. Elshaari, I. E. Zadeh, K. D. Jöns, V. Zwiller, *IEEE Photonics J.* **2016**, *8*, 2701009.
- [16] S. Wang, H. Wang, C. Li, C. Zhuang, R. Zeng, *High Voltage* **2022**, *7*, 840.
- [17] B. Jalali, V. Raghunathan, R. Shori, S. Fathpour, D. Dimitropoulos, O. Stafsudd, *IEEE J. Quantum Electron.* **2006**, *12*, 1618.
- [18] L. Chang, M. H. P. Pfeiffer, N. Volet, M. Zervas, J. D. Peters, C. L. Manganelli, E. J. Stanton, Y. Li, T. J. Kippenberg, J. E. Bowers, *Opt. Lett.* **2017**, *42*, 803.
- [19] A. Rickman, *Nat. Photonics* **2014**, *8*, 579.
- [20] Yole Group, <https://www.yolegroup.com/>.
- [21] Scopus - Document search | Signed in, <https://www.scopus.com/search/form.uri#basic>.
- [22] Y. Liu, A. Choudhary, D. Marpaung, B. J. Eggleton, *Adv. Opt. Photonics* **2020**, *12*, 485.
- [23] G. Brunetti, N. Saha, G. Campiti, A. di Toma, N. Sasanelli, F. Hassan, M. N. Armenise, C. Ciminelli, in *APPLEPIES 2023*, pp. 294–299.
- [24] S.-W. Jeong, T.-H. Lee, J. Lee, *IEEE Trans. Microwave Theory Tech.* **2019**, *67*, 2172.
- [25] A. Lalbakhsh, S. M. Alizadeh, A. Ghaderi, A. Golestanifar, B. Mohamadzade, M. B. Jamshidi, K. Mandal, W. Mohyuddin, *Electronics* **2020**, *9*, 1770.
- [26] D. Li, K.-D. Xu, *Electron. Lett.* **2020**, *56*, 721.
- [27] B. Zong, C. Fan, X. Wang, X. Duan, B. Wang, J. Wang, *IEEE Veh. Technol. Mag.* **2019**, *14*, 18.
- [28] W. Cheng, D. Lin, P. Wang, S. Shi, M. Lu, J. Wang, C. Guo, Y. Chen, Z. Cang, Z. Tian, Z. Liang, G. Hu, B. Yun, *Opt. Express* **2023**, *31*, 25648.
- [29] History of Silicon Photonics | DustPhotonics, <https://www.dustphotonics.com/an-overview-of-the-evolution-of-silicon-photonics/>.
- [30] S. Deleonibus, *EPJ Appl. Phys.* **2006**, *36*, 197.
- [31] D. Liu, H. Xu, Y. Tan, Y. Shi, D. Dai, *Microwave Opt. Technol. Lett.* **2021**, *63*, 2252.
- [32] T. Horikawa, D. Shimura, T. Mogami, *MRS Commun.* **2016**, *6*, 9.
- [33] S. K. Selvaraja, P. De Heyn, G. Winroth, P. Ong, G. Lepage, C. Cailler, A. Rigny, K. K. Bourdelle, W. Bogaerts, D. Van Thourhout, J. Van Campenhout, P. Absil, in *OFC 2014 2014*, pp. 1–3.
- [34] J. E. Heebner, V. Wong, A. Schweinsberg, R. W. Boyd, D. J. Jackson, *IEEE J. Quantum Electron.* **2004**, *40*, 726.
- [35] W. Bogaerts, P. de Heyn, T. van Vaerenbergh, K. de Vos, S. Kumar Selvaraja, T. Claes, P. Dumon, P. Bienstman, D. van Thourhout, R. Baets, *Laser Photonics Rev.* **2012**, *6*, 47.
- [36] T. Erdogan, *J. Lightwave Technol.* **1997**, *15*, 1277.
- [37] R. Cheng, L. Chrostowski, *J. Lightwave Technol.* **2021**, *39*, 712.
- [38] M. Papadovasilakis, S. Chandran, Y. Gebregiorgis, Y. Bian, M. Rakowski, S. Krishnamurthy, R. Augur, J. Viegas, in *Integrated Photonics Research, Silicon and Nanophotonics 2021*, p. IM2A-6.
- [39] J. Zou, F. Sun, C. Wang, M. Zhang, J. Wang, T. Lang, X. Wang, Z. Le, J.-J. He, *Opt. Laser Technol.* **2022**, *147*, 107656.
- [40] T. Barwicz, M. A. Popovic, M. R. Watts, P. T. Rakich, E. P. Ippen, H. I. Smith, *J. Lightwave Technol.* **2006**, *24*, 2207.
- [41] B. Kaleli, A. A. I. Aarnink, S. Smits, R. J. E. Huetting, R. A. M. Wolters, J. Schmit, in *STW ICT Conf (2010) 2010*, pp. 18–19.
- [42] Y. Wang, Z. Lin, C. Zhang, F. Gao, F. Zhang, *IEEE J. Sel. Top. Quantum Electron.* **2005**, *11*, 254.
- [43] C.-K. Chung, *J. Micromech. Microeng.* **2004**, *14*, 656.
- [44] X. Mu, S. Wu, L. Cheng, H. Y. Fu, *Appl. Sci.* **2020**, *10*, 1538.
- [45] L. Cheng, S. Mao, Z. Li, Y. Han, H. Y. Fu, *Micromachines* **2020**, *11*, 666.
- [46] D. Liang, G. Roelkens, R. Baets, J. E. Bowers, *Materials* **2010**, *3*, 1782.
- [47] J. Van Roey, J. van der Donk, P. E. Lagasse, *J. Opt. Soc. Am.* **1981**, *71*, 803.

- [48] D. Yevick, B. Hermansson, *IEEE J. Quantum Electron.* **1990**, *26*, 109.
- [49] Y. Chung, N. Dagli, *IEEE J. Quantum Electron.* **1990**, *26*, 1335.
- [50] M. D. Feit, J. A. Fleck, *Appl. Opt.* **1978**, *17*, 3990.
- [51] H. P. Nolting, R. Marz, *J. Lightwave Technol.* **1995**, *13*, 216.
- [52] W. P. Huang, C. L. Xu, *IEEE J. Quantum Electron.* **1993**, *29*, 2639.
- [53] G. R. Hadley, *Opt. Lett.* **1992**, *17*, 1426.
- [54] H. Rao, R. Scarmozzino, R. M. Osgood, *IEEE Photonics Technol. Lett.* **1999**, *11*, 830.
- [55] S.-T. Peng, A. A. Oliner, *IEEE Trans. Microwave Theory Tech.* **1981**, *29*, 843.
- [56] A. Sv Sudbo, *Pure Appl. Opt.* **1993**, *2*, 211.
- [57] G. Sztefka, H. P. Nolting, *IEEE Photonics Technol. Lett.* **1993**, *5*, 554.
- [58] S. Johnson, A. Oskooi, A. Taflove, *Advances in FDTD Computational Electrodynamics: Photonics and Nanotechnology*, Artech **2013**.
- [59] K. Yee, *IEEE Trans. Antennas Propag.* **1966**, *14*, 302.
- [60] Q. H. Liu, *IEEE Trans. Ultrason. Ferroelectr. Freq. Control* **1998**, *45*, 1044.
- [61] A. Hrennikoff, *J. Appl. Mech.* **1941**, *8*, A169.
- [62] A. Agrawal, B. M. A. Rahman, *Finite Element Modeling Methods for Photonics*, Artech **2013**.
- [63] I. M. Hammond, A. M. Hammond, R. M. Camacho, *Opt. Lett.* **2022**, *47*, 1383.
- [64] D. Seyringer, F. Uherek, J. Chovan, A. Kuzma, in *Ninth Int. Conf. Advanced Semiconductor Devices and Microsystems* **2012**, pp. 303–306.
- [65] A. H. Atabaki, E. S. Hosseini, A. A. Eftekhar, S. Yegnanarayanan, A. Adibi, *Opt. Express* **2010**, *18*, 18312.
- [66] G. Brunetti, F. Dell'Olio, D. Conteduca, M. N. Armenise, C. Ciminelli, *J. Lightwave Technol.* **2019**, *37*, 2970.
- [67] N. Saha, G. Brunetti, M. N. Armenise, C. Ciminelli, *Opt. Express* **2022**, *30*, 28632.
- [68] I. Rendina, *Electron. Lett.* **1992**, *28*, 83.
- [69] P. Pintus, M. Hofbauer, C. L. Manganelli, M. Fournier, S. Gundavarapu, O. Lemonnier, F. Gambini, L. Adelmini, C. Meinhardt, C. Kopp, F. Testa, H. Zimmermann, C. J. Oton, *Laser Photonics Rev.* **2019**, *13*, 1800275.
- [70] G. Brunetti, G. Marocco, A. Di Benedetto, A. Giorgio, M. N. Armenise, C. Ciminelli, *J. Opt.* **2021**, *23*, 085801.
- [71] F. Gao, W. Xie, J. Y. S. Tan, C. P. Leong, C. Li, X. Luo, G.-Q. Lo, *Micromachines* **2022**, *13*, 1925.
- [72] F. Morichetti, M. Milanizadeh, M. Petrini, F. Zanetto, G. Ferrari, D. O. de Aguiar, E. Guglielmi, M. Sampietro, A. Melloni, *Nat. Commun.* **2021**, *12*, 4324.
- [73] D. Liu, H. Wu, D. Dai, *J. Lightwave Technol.* **2019**, *37*, 2217.
- [74] J. Li, Y. Liu, Y. Meng, K. Xu, J. Du, F. Wang, Z. He, Q. Song, *IEEE Photonics Technol. Lett.* **2018**, *30*, 471.
- [75] N. Saha, G. Brunetti, M. N. Armenise, C. Ciminelli, *Proc. SPIE* **2023**, *12575*, 125750D.
- [76] P. Dong, W. Qian, H. Liang, R. Shafiha, D. Feng, G. Li, J. E. Cunningham, A. V. Krishnamoorthy, M. Asghari, *Opt. Express* **2010**, *18*, 20298.
- [77] P. Dong, W. Qian, H. Liang, R. Shafiha, N.-N. Feng, D. Feng, X. Zheng, A. V. Krishnamoorthy, M. Asghari, *Opt. Express* **2010**, *18*, 9852.
- [78] X. Wu, W. Liu, Z. Yuan, X. Liang, H. Chen, X. Xu, F. Tang, *IEEE Photonics J.* **2018**, *10*, 1.
- [79] D. Coenen, H. Oprins, Y. Ban, F. Ferraro, M. Pantouvaki, J. Van Campenhout, I. De Wolf, *J. Lightwave Technol.* **2022**, *40*, 4357.
- [80] F. Duan, K. Chen, Y. Yu, *Opt. Quantum Electron.* **2019**, *52*, 5.
- [81] F. Duan, K. Chen, Y. Yu, *Opt. Commun.* **2019**, *439*, 239.
- [82] F. Duan, K. Chen, Y. Yu, *Opt. Quantum Electron.* **2020**, *52*, 1.
- [83] Q. Xu, B. Schmidt, S. Pradhan, M. Lipson, *Nature* **2005**, *435*, 325.
- [84] W. Zhang, J. Yao, *Nat. Commun.* **2018**, *9*, 1396.
- [85] C. A. Barrios, V. R. Almeida, R. Panepucci, M. Lipson, *J. Lightwave Technol.* **2003**, *21*, 2332.
- [86] W. Zhang, N. Ehteshami, W. Liu, J. Yao, *Opt. Lett.* **2015**, *40*, 3153.
- [87] G. T. Reed, G. Mashanovich, F. Y. Gardes, D. J. Thomson, *Nat. Photonics* **2010**, *4*, 518.
- [88] D. M. Dourado, G. B. de Farias, R. H. Gounella, M. d. L. Rocha, J. P. Carmo, *Opt. Laser Technol.* **2021**, *144*, 107376.
- [89] Q. Fang, J. F. Song, X. Tu, L. Jia, X. Luo, M. Yu, G. Q. Lo, *IEEE Photonics Technol. Lett.* **2013**, *25*, 810.
- [90] H. Xu, D. Dai, Y. Shi, *Opt. Express* **2021**, *29*, 20617.
- [91] D. Liu, M. Zhang, Y. Shi, D. Dai, *IEEE Photonics Technol. Lett.* **2020**, *32*, 192.
- [92] D. T. H. Tan, A. Grieco, Y. Fainman, *Opt. Express* **2014**, *22*, 10408.
- [93] D. Munk, M. Katzman, Y. Kaganovskii, N. Inbar, A. Misra, M. Hen, M. Priel, M. Feldberg, M. Tkachev, A. Bergman, M. Vofsi, M. Rosenbluh, T. Schneider, A. Zadok, *IEEE J. Sel. Top. Quantum Electron.* **2019**, *25*, 1.
- [94] F. Rukerandanga, S. Musyoki, E. O. Ataro, *Heliyon* **2022**, *8*, e09567.
- [95] Q. Yi, S. Zheng, Z. Yan, G. Cheng, F. Xu, Q. Li, L. Shen, *Opt. Express* **2022**, *30*, 28232.
- [96] Z. Li, A. M. Heidt, J. M. O. Daniel, Y. Jung, S. U. Alam, D. J. Richardson, *Opt. Express* **2013**, *21*, 9289.
- [97] F. Horst, W. M. J. Green, S. Assefa, S. M. Shank, Y. A. Vlasov, B. J. Offrein, *Opt. Express* **2013**, *21*, 11652.
- [98] Z. Zhao, Z. Li, J. Niu, G. Zhang, H. Chen, X. Fu, L. Yang, *Photonics* **2022**, *9*, 252.
- [99] H. Xu, Y. Shi, *IEEE Photonics Technol. Lett.* **2018**, *30*, 169.
- [100] L. Han, B. P. P. Kuo, A. Pejkić, N. Alic, S. Radic, in *2019 Optical Fiber Communications Conf. Exhibition (OFC)* **2019**, pp. 1–3.
- [101] S.-H. Jeong, Y. Tanaka, *Appl. Opt.* **2018**, *57*, 6474.
- [102] T.-H. Yen, Y.-J. Hung, *J. Lightwave Technol.* **2021**, *39*, 146.
- [103] H. Xu, L. Liu, Y. Shi, *Opt. Lett.* **2018**, *43*, 1483.
- [104] J. F. Song, S. H. Tao, Q. Fang, T. Y. Liow, M. B. Yu, G. Q. Lo, D. L. Kwong, *IEEE Photonics Technol. Lett.* **2008**, *20*, 2165.
- [105] X. Jiang, J. Wu, Y. Yang, T. Pan, J. Mao, B. Liu, R. Liu, Y. Zhang, C. Qiu, C. Tremblay, Y. Su, *Opt. Express* **2016**, *24*, 2183.
- [106] N. Zhou, S. Zheng, Y. Long, Z. Ruan, L. Shen, J. Wang, *Opt. Express* **2018**, *26*, 4358.
- [107] B. E. Little, S. T. Chu, H. A. Haus, J. Foresi, J.-P. Laine, *J. Lightwave Technol.* **1997**, *15*, 998.
- [108] P. Dong, N.-N. Feng, D. Feng, W. Qian, H. Liang, D. C. Lee, B. J. Luff, T. Banwell, A. Agarwal, P. Toliver, R. Menendez, T. K. Woodward, M. Asghari, *Opt. Express* **2010**, *18*, 23784.
- [109] T. Hu, W. Wang, C. Qiu, P. Yu, H. Qiu, Y. Zhao, X. Jiang, J. Yang, *IEEE Photonics Technol. Lett.* **2012**, *24*, 524.
- [110] A. M. Prabhu, A. Tsay, Z. Han, V. Van, *IEEE Photonics Technol. Lett.* **2009**, *21*, 651.
- [111] A. M. Prabhu, A. Tsay, Z. Han, V. Van, *IEEE Photonics J.* **2010**, *2*, 436.
- [112] D. Liu, C. Zhang, D. Liang, D. Dai, *Opt. Express* **2019**, *27*, 416.
- [113] D. Liu, L. Zhang, Y. Tan, D. Dai, *J. Lightwave Technol.* **2021**, *39*, 5910.
- [114] D. Liu, J. He, Y. Xiang, Y. Xu, D. Dai, *APL Photonics* **2022**, *7*, 051303.
- [115] R. Boeck, J. Flueckiger, L. Chrostowski, N. A. F. Jaeger, *Opt. Express* **2013**, *21*, 9103.
- [116] Y. Tan, S. Chen, D. Dai, *Opt. Express* **2017**, *25*, 4106.
- [117] Y. K. Verma, S. Kumari, G. Bawa, S. M. Tripathi, *Opt. Quantum Electron.* **2022**, *54*, 839.
- [118] Y. Ren, D. Perron, F. Aurangozeb, Z. Jiang, M. Hossain, V. Van, *IEEE Photonics Technol. Lett.* **2019**, *31*, 1503.
- [119] D. Mu, H. Qiu, J. Jiang, X. Wang, Z. Fu, Y. Wang, X. Jiang, H. Yu, J. Yang, *IEEE Photonics J.* **2019**, *11*, 1.
- [120] W. Shi, X. Wang, C. Lin, H. Yun, Y. Liu, T. Baehr-Jones, M. Hochberg, N. A. F. Jaeger, L. Chrostowski, *Opt. Express* **2013**, *21*, 3633.
- [121] H. Qiu, G. Jiang, T. Hu, H. Shao, P. Yu, J. Yang, X. Jiang, *Opt. Lett.* **2013**, *38*, 1.

- [122] A. D. Simard, S. LaRochelle, *Opt. Express* **2015**, *23*, 16662.
- [123] H. Qiu, J. Jiang, T. Hu, P. Yu, J. Yang, X. Jiang, H. Yu, *J. Lightwave Technol.* **2017**, *35*, 1705.
- [124] S. Xie, J. Zhan, Y. Hu, Y. Zhang, S. Veilleux, J. Bland-Hawthorn, M. Dagenais, *Opt. Lett.* **2018**, *43*, 6045.
- [125] C. Greiner, T. W. Mossberg, D. Iazikov, *Opt. Lett.* **2004**, *29*, 806.
- [126] W. Shi, H. Yun, C. Lin, J. Flueckiger, N. A. F. Jaeger, L. Chrostowski, *Opt. Lett.* **2013**, *38*, 3068.
- [127] M. J. Strain, M. Sorel, *IEEE Photonics Technol. Lett.* **2008**, *20*, 1863.
- [128] J. Jiang, H. Qiu, G. Wang, Y. Li, T. Dai, D. Mu, H. Yu, J. Yang, X. Jiang, *Appl. Opt.* **2017**, *56*, 8425.
- [129] D. T. H. Tan, K. Ikeda, S. Zamek, A. Mizrahi, M. P. Nezhad, A. V. Krishnamoorthy, K. Raj, J. E. Cunningham, X. Zheng, I. Shubin, Y. Luo, Y. Fainman, *Opt. Express* **2011**, *19*, 2401.
- [130] A. Mistry, M. Hammood, H. Shoman, L. Chrostowski, N. A. F. Jaeger, *Opt. Lett.* **2018**, *43*, 6041.
- [131] T.-C. Wang, T.-H. Yen, C.-J. Yu, Y.-C. Wang, Y. Hung, in *Conf. Lasers and Electro-Optics, OSA Technical Digest*, Optica Publishing Group **2020**, p. JTh2F.32.
- [132] J. St-Yves, H. Bahrami, P. Jean, S. LaRochelle, W. Shi, *Opt. Lett.* **2015**, *40*, 5471.
- [133] J. Jiang, H. Qiu, G. Wang, Y. Li, T. Dai, X. Wang, H. Yu, J. Yang, X. Jiang, *Opt. Express* **2018**, *26*, 559.
- [134] X. Wang, H. Yu, H. Qiu, Q. Zhang, Z. Fu, P. Xia, B. Chen, X. Guo, Y. Wang, X. Jiang, J. Yang, *Opt. Express* **2020**, *28*, 14461.
- [135] T. Barwicz, M. R. Watts, M. A. Popović, P. T. Rakich, L. Socci, F. X. Kärtner, E. P. Ippen, H. I. Smith, *Nat. Photonics* **2007**, *1*, 57.
- [136] J. Zhang, H. Zhang, S. Chen, M. Yu, G. Q. Lo, D. L. Kwong, *Opt. Express* **2011**, *19*, 13063.
- [137] D. Liu, D. Dai, *Opt. Express* **2019**, *27*, 20704.
- [138] N. Ning, H. Yu, Q. Zhang, Q. Huang, Z. Fu, P. Xia, Z. Wei, X. Wang, Y. Wang, J. Yang, *Opt. Lett.* **2023**, *48*, 65.
- [139] V. Kannaiyan, S. K. Dhamodharan, R. Savarimuthu, *J. Opt. Commun.* **2022**, *43*, 493.
- [140] M. A. Butt, S. N. Khonina, N. L. Kazanskiy, *Opt. Laser Technol.* **2021**, *142*, 107265.
- [141] D. Dai, J. E. Bowers, *Nanophotonics* **2014**, *3*, 283.
- [142] S. Tondini, C. Castellan, M. Mancinelli, C. Kopp, L. Pavesi, *J. Lightwave Technol.* **2017**, *35*, 5134.
- [143] K. Okamoto, K. Ishida, *Opt. Lett.* **2013**, *38*, 3530.
- [144] J. Zou, T. Lang, Z. Le, J.-J. He, *Appl. Opt.* **2016**, *55*, 3531.
- [145] D. Dai, X. Fu, Y. Shi, S. He, *Opt. Lett.* **2010**, *35*, 2594.
- [146] L. G. de Peralta, A. A. Bernussi, S. Frisbie, R. Gale, H. Temkin, *IEEE Photonics Technol. Lett.* **2003**, *15*, 1398.
- [147] D. Admassu, T. Durowade, R. Sellers, S. Sivananthan, *Microsyst. Technol.* **2021**, *27*, 2785.
- [148] S. Chen, X. Fu, J. Wang, Y. Shi, S. He, D. Dai, *J. Lightwave Technol.* **2015**, *33*, 2279.
- [149] D. Dai, S. He, *Opt. Lett.* **2006**, *31*, 1988.
- [150] L. Wang, W. Bogaerts, P. Dumon, S. K. Selvaraja, J. Teng, S. Pathak, X. Han, J. Wang, X. Jian, M. Zhao, R. Baets, G. Morthier, *Appl. Opt.* **2012**, *51*, 1251.
- [151] G. Chen, T. Lang, J. Zou, J.-J. He, in *Asia Communications and Photonics Conf. 2013, OSA Technical Digest (Online)*, Optica Publishing Group **2013**, p. AF1A.5.
- [152] K.-F. Chung, P.-H. Fu, Y.-T. Shih, H.-K. Chiu, T.-T. Shih, D.-W. Huang, *Opt. Express* **2022**, *30*, 25842.
- [153] Y. Liu, X. Wang, Y. Yao, J. Du, Q. Song, K. Xu, *Opt. Lett.* **2022**, *47*, 1186.
- [154] A. Mirza, F. Sunny, P. Walsh, K. Hassan, S. Pasricha, M. Nikdast, *IEEE Trans. Comput. Aided Des. Integr. Circuits Syst.* **2022**, *41*, 3359.
- [155] A. Mirza, F. Sunny, S. Pasricha, M. Nikdast, in *2020 Design, Automation & Test in Europe Conf. Exhibition (DATE) 2020*, pp. 484–489.
- [156] S. Gringeri, B. Basch, V. Shukla, R. Egorov, T. J. Xia, *IEEE Commun. Mag.* **2010**, *48*, 40.
- [157] Q. Cheng, M. Bahadori, M. Glick, S. Rumley, K. Bergman, *Optica* **2018**, *5*, 1354.
- [158] S. Cheung, T. Su, K. Okamoto, S. J. B. Yoo, *IEEE J. Sel. Top. Quantum Electron.* **2014**, *20*, 310.
- [159] L. Wang, J. Zhang, J. An, J. Chen, B. Sun, T. Zhou, X. Yin, Y. Wang, Y. Wu, *Opt. Express* **2023**, *31*, 37829.
- [160] Z. Fang, R. Chen, J. Zheng, A. Majumdar, *IEEE J. Sel. Top. Quantum Electron.* **2022**, *28*, 1.
- [161] K. J. Miller, R. F. Haglund, S. M. Weiss, *Opt. Mater. Express* **2018**, *8*, 2415.
- [162] M. Wuttig, H. Bhaskaran, T. Taubner, *Nat. Photonics* **2017**, *11*, 465.
- [163] Y. Shi, Y. Zhang, Y. Wan, Y. Yu, Y. Zhang, X. Hu, X. Xiao, H. Xu, L. Zhang, B. Pan, *Photonics Res.* **2022**, *10*, A106.
- [164] J. Yao, J. Capmany, *Sci. China Inf. Sci.* **2022**, *65*, 221401.
- [165] M. Sotom, M. Aveline, R. Barbaste, B. Benazet, A. Le Kernec, J. Magnaval, M. Picq, *Proc. SPIE* **2017**, *10562*, 105621Y.
- [166] D. Marpaung, J. Yao, J. Capmany, *Nat. Photonics* **2019**, *13*, 80.
- [167] J. Capmany, B. Ortega, D. Pastor, *J. Lightwave Technol.* **2006**, *24*, 201.
- [168] J. Yao, *IEEE Microwave Mag.* **2015**, *16*, 46.
- [169] W. Zhang, J. Yao, *J. Lightwave Technol.* **2018**, *36*, 4655.
- [170] X. Xue, Y. Xuan, H.-J. Kim, J. Wang, D. E. Leaird, M. Qi, A. M. Weiner, *J. Lightwave Technol.* **2014**, *32*, 3557.
- [171] J. Sancho, J. Bourderionnet, J. Lloret, S. Combríe, I. Gasulla, S. Xavier, S. Sales, P. Colman, G. Lehoucq, D. Dolfi, J. Capmany, A. De Rossi, *Nat. Commun.* **2012**, *3*, 1075.
- [172] W. Zhang, J. Yao, in *2017 Int. Topical Meeting on Microwave Photonics (MWP) 2017*, pp. 1–4.
- [173] V. R. Supradeepa, C. M. Long, R. Wu, F. Ferdous, E. Hamidi, D. E. Leaird, A. M. Weiner, *Nat. Photonics* **2012**, *6*, 186.
- [174] D. Marpaung, B. Morrison, M. Pagani, R. Pant, D.-Y. Choi, B. Luther-Davies, S. J. Madden, B. J. Eggleton, *Optica* **2015**, *2*, 76.
- [175] C. Roeloffzen, C. G. H. Roeloffzen, L. Zhuang, R. G. Heideman, A. Borreman, W. Van Etten, in *10th Annual Symp. IEEE/LEOS Benelux Chapter*, IEEE, Piscataway, NJ **2005**.
- [176] D. G. Rabus, *Integrated Ring Resonators*, Springer-Verlag Berlin Heidelberg **2007**.
- [177] A. Velamuri, B. K. Das, *J. Lightwave Technol.* **2024**, *42*, 1586.
- [178] S. Song, S. X. Chew, X. Yi, L. Nguyen, R. A. Minasian, *J. Lightwave Technol.* **2018**, *36*, 4557.
- [179] Y. Long, J. Wang, *Opt. Express* **2015**, *23*, 17739.
- [180] L. Liu, F. Jiang, S. Yan, S. Min, M. He, D. Gao, J. Dong, *Opt. Commun.* **2015**, *335*, 266.
- [181] G. Li, J. Yao, H. Thacker, A. Mekis, X. Zheng, I. Shubin, Y. Luo, J. Lee, K. Raj, J. E. Cunningham, A. V. Krishnamoorthy, *Opt. Express* **2012**, *20*, 12035.
- [182] H. Qiu, F. Zhou, J. Qie, Y. Yao, X. Hu, Y. Zhang, X. Xiao, Y. Yu, J. Dong, X. Zhang, *J. Lightwave Technol.* **2018**, *36*, 4312.
- [183] L. Zhuang, M. Hoekman, W. Beeker, A. Leinse, R. Heideman, P. van Dijk, C. Roeloffzen, *Laser Photonics Rev.* **2013**, *7*, 994.
- [184] R. Grover, V. Van, T. A. Ibrahim, P. P. Absil, L. C. Calhoun, F. G. Johnson, J. V. Hryniewicz, P.-T. Ho, *J. Lightwave Technol.* **2002**, *20*, 872.
- [185] R. A. Cohen, O. Amrani, S. Ruschin, *Opt. Express* **2015**, *23*, 2252.
- [186] L. Xu, Y. Yu, X. Liu, X. Shu, X. Zhang, *ACS Photonics* **2021**, *8*, 3156.
- [187] F. Xia, L. Sekaric, Y. Vlasov, *Nat. Photonics* **2007**, *1*, 65.
- [188] A. Melloni, A. Canciamilla, C. Ferrari, F. Morichetti, L. O'Faolain, T. F. Krauss, R. D. La Rue, A. Samarelli, M. Sorel, *IEEE Photonics J.* **2010**, *2*, 181.
- [189] S. Romero-García, A. Moscoso-Mártir, J. Müller, B. Shen, F. Merget, J. Witzens, *Opt. Express* **2018**, *26*, 4723.

- [190] J. Cardenas, M. A. Foster, N. Sherwood-Droz, C. B. Poitras, H. L. R. Lira, B. Zhang, A. L. Gaeta, J. B. Khurgin, P. Morton, M. Lipson, *Opt. Express* **2010**, *18*, 26525.
- [191] L. Zhuang, *Opt. Lett.* **2016**, *41*, 1118.
- [192] J. M. Wyrwas, R. Peach, S. Meredith, C. Middleton, M. S. Rasras, K.-Y. Tu, M. P. Earnshaw, F. Pardo, M. A. Cappuzzo, E. Y. Chen, L. T. Gomez, F. Klemens, R. Keller, C. Bolle, L. Zhang, L. Buhl, M. C. Wu, Y. K. Chen, R. DeSalvo, *Opt. Express* **2012**, *20*, 26292.
- [193] K. Oda, N. Takato, H. Toba, K. Nosu, *J. Lightwave Technol.* **1988**, *6*, 1016.
- [194] M. Wang, X. Chen, U. Khan, W. Bogaerts, *Sci. Rep.* **2022**, *12*, 1482.
- [195] W. Jiang, L. Xu, Y. Liu, Y. Chen, X. Liu, Y. Yu, Y. Yu, X. Zhang, *ACS Photonics* **2020**, *7*, 2539.
- [196] X. Liu, Y. Yu, H. Tang, L. Xu, J. Dong, X. Zhang, *Opt. Lett.* **2018**, *43*, 1359.
- [197] A. Singh, R. Belansky, M. Soltani, *Opt. Express* **2022**, *30*, 43787.
- [198] R. An, G. Wang, W. Ji, W. Jiao, M. Jiang, Y. Chang, X. Xu, N. Zou, X. Zhang, *Opt. Lett.* **2018**, *43*, 3901.
- [199] X. Wang, W. Shi, H. Yun, S. Grist, N. A. F. Jaeger, L. Chrostowski, *Opt. Express* **2012**, *20*, 15547.
- [200] W. Zhang, J. Yao, *J. Lightwave Technol.* **2019**, *37*, 314.
- [201] G. Serafino, C. Porzi, P. Velha, N. Andriolli, P. Ghelfi, A. Bogoni, in *ECOC 2016; 42nd European Conf. Optical Communication* **2016**, pp. 1–3.
- [202] M. Burla, H. P. Bazargani, J. St-Yves, W. Shi, L. Chrostowski, J. Azaña, in *2014 IEEE Photonics Conf.*, IEEE, Piscataway, NJ **2014**, pp. 208–209.
- [203] B. J. Eggleton, C. G. Poulton, P. T. Rakich, M. J. Steel, G. Bahl, *Nat. Photonics* **2019**, *13*, 664.
- [204] A. Casas-Bedoya, B. Morrison, M. Pagani, D. Marpaung, B. J. Eggleton, *Opt. Lett.* **2015**, *40*, 4154.
- [205] H. Shin, J. A. Cox, R. Jarecki, A. Starbuck, Z. Wang, P. T. Rakich, *Nat. Commun.* **2015**, *6*, 6427.
- [206] E. A. Kittlaus, P. Kharel, N. T. Otterstrom, Z. Wang, P. T. Rakich, *J. Lightwave Technol.* **2018**, *36*, 2803.
- [207] L. Zhuang, C. G. H. Roeloffzen, M. Hoekman, K.-J. Boller, A. J. Lowery, *Optica* **2015**, *2*, 854.
- [208] D. Pérez, I. Gasulla, J. Capmany, *J. Lightwave Technol.* **2017**, *36*, 519.
- [209] D. Pérez, I. Gasulla, L. Crudgington, D. J. Thomson, A. Z. Khokhar, K. Li, W. Cao, G. Z. Mashanovich, J. Capmany, *Nat. Commun.* **2017**, *8*, 636.
- [210] D. Pérez, I. Gasulla, J. Capmany, *Nanophotonics* **2018**, *7*, 1351.
- [211] F. X. Min Tan, *Applied Optics and Photonics China*, SPIE **2021**.
- [212] D. Marpaung, C. Roeloffzen, R. Heideman, A. Leinse, S. Sales, J. Capmany, *Laser Photonics Rev.* **2013**, *7*, 506.
- [213] S. De, A. A. Bazil Raj, *J. Opt.* **2023**, *52*, 90.
- [214] C. Zhu, L. Lu, W. Shan, W. Xu, G. Zhou, L. Zhou, J. Chen, *Optica* **2020**, *7*, 1162.
- [215] J. Wang, F. Sciarrino, A. Laing, M. G. Thompson, *Nat. Photonics* **2020**, *14*, 273.
- [216] G. Moody, V. J. Sorger, D. J. Blumenthal, P. W. Juodawlkis, W. Loh, C. Sorace-Agaskar, A. E. Jones, K. C. Balram, J. C. F. Matthews, A. Laing, M. Davanco, L. Chang, J. E. Bowers, N. Quack, C. Galland, I. Aharonovich, M. A. Wolff, C. Schuck, N. Sinclair, M. Lončar, T. Komljenovic, D. Weld, S. Mookherjee, S. Buckley, M. Radulaski, S. Reitzenstein, B. Pingault, B. Machielse, D. Mukhopadhyay, A. Akimov, et al., *JPhys Photonics* **2022**, *4*, 012501.
- [217] A. Politi, M. J. Cryan, J. G. Rarity, S. Yu, J. L. O'Brien, *Science* **2008**, *320*, 646.
- [218] G. Zhang, Z. Zhao, J. Dai, S. Yang, X. Fu, L. Yang, *J. Lightwave Technol.* **2022**, *40*, 2052.
- [219] S. Paesani, Y. Ding, R. Santagati, L. Chakhmakchyan, C. Vigliar, K. Rottwitz, L. K. Oxenløwe, J. Wang, M. G. Thompson, A. Laing, *Nat. Phys.* **2019**, *15*, 925.
- [220] J. C. F. Matthews, A. Politi, D. Bonneau, J. L. O'Brien, *Phys. Rev. Lett.* **2011**, *107*, 163602.
- [221] M. Piekarek, D. Bonneau, S. Miki, T. Yamashita, M. Fujiwara, M. Sasaki, H. Terai, M. G. Tanner, C. M. Natarajan, R. H. Hadfield, J. L. O'Brien, M. G. Thompson, *Opt. Lett.* **2017**, *42*, 815.
- [222] A. Goswami, B. Krishna Das, *Opt. Lett.* **2022**, *47*, 1474.
- [223] C. Klitis, G. Cantarella, M. J. Strain, M. Sorel, *Opt. Lett.* **2017**, *42*, 3040.
- [224] R. R. Kumar, X. Wu, H. K. Tsang, *Opt. Lett.* **2020**, *45*, 1289.
- [225] R. R. Kumar, H. K. Tsang, *Opt. Lett.* **2021**, *46*, 134.
- [226] G. Brunetti, N. Sasanelli, M. N. Armenise, C. Ciminelli, *Opt. Laser Technol.* **2021**, *139*, 106978.
- [227] N. C. Harris, D. Grassani, A. Simbula, M. Pant, M. Galli, T. Baehr-Jones, M. Hochberg, D. Englund, D. Bajoni, C. Galland, *Phys. Rev. X* **2014**, *4*, 41047.
- [228] J. Michon, X. Le Roux, A. Huot de Saint-Albin, D. Oser, S. Tanzilli, L. Labonté, E. Cassan, L. Vivien, C. Alonso-Ramos, *Opt. Lett.* **2022**, *47*, 341.
- [229] N. Matsuda, H. Le Jeannic, H. Fukuda, T. Tsuchizawa, W. J. Munro, K. Shimizu, K. Yamada, Y. Tokura, H. Takesue, *Sci. Rep.* **2012**, *2*, 817.
- [230] R. T. Horn, P. Kolenderski, D. Kang, P. Abolghasem, C. Scarcella, A. Della Frera, A. Tosi, L. G. Helt, S. V. Zhukovsky, J. E. Sipe, G. Weihs, A. S. Helmy, T. Jennewein, *Sci. Rep.* **2013**, *3*, 2314.
- [231] S. Sharma, V. Venkataraman, J. Ghosh, *Phys. Rev. Appl.* **2022**, *18*, 44043.
- [232] X. Chen, Z. Fu, Q. Gong, J. Wang, *Adv. Photonics* **2021**, *3*, 064002.
- [233] J. W. Silverstone, D. Bonneau, J. L. O'Brien, M. G. Thompson, *IEEE J. Sel. Top. Quantum Electron.* **2016**, *22*, 390.
- [234] J. W. Silverstone, D. Bonneau, K. Ohira, N. Suzuki, H. Yoshida, N. Iizuka, M. Ezaki, C. M. Natarajan, M. G. Tanner, R. H. Hadfield, V. Zwiller, G. D. Marshall, J. G. Rarity, J. L. O'Brien, M. G. Thompson, *Nat. Photonics* **2014**, *8*, 104.
- [235] J. W. Silverstone, R. Santagati, D. Bonneau, M. J. Strain, M. Sorel, J. L. O'Brien, M. G. Thompson, *Nat. Commun.* **2015**, *6*, 7948.
- [236] R. Santagati, J. W. Silverstone, M. J. Strain, M. Sorel, S. Miki, T. Yamashita, M. Fujiwara, M. Sasaki, H. Terai, M. G. Tanner, C. M. Natarajan, R. H. Hadfield, J. L. O'Brien, M. G. Thompson, *J. Opt.* **2017**, *19*, 114006.
- [237] G. Zhang, C. Wang, K. T. Goh, S. Q. Ng, R. Ho, H. Semenenko, S. A. Srinivasan, H. Wang, Y. Chen, J. Y. Haw, X. Gong, J. Van Campenhout, C. C.-W. Lim, *CLEO 2023, Technical Digest Series*, Optica Publishing Group **2023**, p. FM4E.7.
- [238] C. Xiong, X. Zhang, A. Mahendra, J. He, D.-Y. Choi, C. J. Chae, D. Marpaung, A. Leinse, R. G. Heideman, M. Hoekman, C. G. H. Roeloffzen, R. M. Oldenbeuving, P. W. L. van Dijk, C. Taddei, P. H. W. Leong, B. J. Eggleton, *Optica* **2015**, *2*, 724.
- [239] R. Wakabayashi, M. Fujiwara, K. Yoshino, Y. Nambu, M. Sasaki, T. Aoki, *Opt. Express* **2015**, *23*, 1103.
- [240] X. Zhang, B. A. Bell, A. Mahendra, C. Xiong, P. H. W. Leong, B. J. Eggleton, *Opt. Lett.* **2018**, *43*, 3469.
- [241] M. Kues, C. Reimer, P. Roztocky, L. R. Cortés, S. Sciara, B. Wetzell, Y. Zhang, A. Cino, S. T. Chu, B. E. Little, D. J. Moss, L. Caspani, J. Azaña, R. Morandotti, *Nature* **2017**, *546*, 622.
- [242] F. Andrea Sabbatoli, L. Gianini, A. Simbula, M. Clementi, A. Fincato, F. Boeuf, M. Liscidini, M. Galli, D. Bajoni, *Opt. Lett.* **2022**, *47*, 6201.
- [243] H. Mahmudlu, R. Johanning, A. van Rees, A. Khodadad Kashi, J. P. Epping, R. Haldar, K. J. Boller, M. Kues, *Nat. Photonics* **2023**, *17*, 518.

- [244] M. Borghi, N. Tagliavacche, F. A. Sabbatoli, H. El Dirani, L. Youssef, C. Petit-Etienne, E. Pargon, J. E. Sipe, M. Liscidini, C. Sciancalepore, M. Galli, D. Bajoni, *Phys. Rev. Appl.* **2023**, *19*, 64026.
- [245] M. Clementi, F. A. Sabbatoli, M. Borghi, L. Gianini, N. Tagliavacche, H. El Dirani, L. Youssef, N. Bergamasco, C. Petit-Etienne, E. Pargon, J. E. Sipe, M. Liscidini, C. Sciancalepore, M. Galli, D. Bajoni, *Nat. Commun.* **2023**, *14*, 176.
- [246] R. M. Camacho, *Opt. Express* **2012**, *20*, 21977.
- [247] J. Chen, Z. H. Levine, J. Fan, A. L. Migdall, *Opt. Express* **2011**, *19*, 1470.
- [248] S. Azzini, D. Grassani, M. Galli, L. C. Andreani, M. Sorel, M. J. Strain, L. G. Helt, J. E. Sipe, M. Liscidini, D. Bajoni, *Opt. Lett.* **2012**, *37*, 3807.
- [249] M. P. Nezhad, O. Bondarenko, M. Khajavikhan, A. Simic, Y. Fainman, *Opt. Express* **2011**, *19*, 18827.
- [250] C. Bellegarde, E. Pargon, C. Sciancalepore, C. Petit-Etienne, O. Lemonnier, K. Ribaud, J.-M. Hartmann, P. Lyan, in *Silicon Photonics XIII*, SPIE **2018**.
- [251] A. Bera, Y. Marin, M. Harjanne, M. Cherchi, T. Aalto, in *Silicon Photonics XVII*, SPIE **2022**.
- [252] J. C. Adcock, J. Bao, Y. Chi, X. Chen, D. Bacco, Q. Gong, L. K. Oxenlowe, J. Wang, Y. Ding, *IEEE J. Sel. Top. Quantum Electron.* **2021**, *27*, 1.
- [253] D. Llewellyn, Y. Ding, I. I. Faruque, S. Paesani, D. Bacco, R. Santagati, Y.-J. Qian, Y. Li, Y.-F. Xiao, M. Huber, M. Malik, G. F. Sinclair, X. Zhou, K. Rottwitz, J. L. O'Brien, J. G. Rarity, Q. Gong, L. K. Oxenlowe, J. Wang, M. G. Thompson, *Nat. Phys.* **2020**, *16*, 148.
- [254] J. B. Spring, P. L. Mennea, B. J. Metcalf, P. C. Humphreys, J. C. Gates, H. L. Rogers, C. Söller, B. J. Smith, W. S. Kolthammer, P. G. R. Smith, I. A. Walmsley, *Optica* **2017**, *4*, 90.
- [255] G. J. Mendoza, R. Santagati, J. Munns, E. Hemsley, M. Piekarek, E. Martín-López, G. D. Marshall, D. Bonneau, M. G. Thompson, J. L. O'Brien, *Optica* **2016**, *3*, 127.
- [256] F. Kaneda, P. G. Kwiat, *Sci. Adv.* **2024**, *5*, 8586.
- [257] M. J. Collins, C. Xiong, I. H. Rey, T. D. Vo, J. He, S. Shahnian, C. Reardon, T. F. Krauss, M. J. Steel, A. S. Clark, B. J. Eggleton, *Nat. Commun.* **2013**, *4*, 2582.
- [258] N. Chen, Z. Wang, J. Wu, H. Li, S. He, Z. Fan, Y. Fan, X. Zhang, Q. Zhou, J. Xu, *Opt. Lett.* **2023**, *48*, 5355.
- [259] N. J. D. Martinez, M. Gehl, C. T. Derose, A. L. Starbuck, A. T. Pomerene, A. L. Lentine, D. C. Trotter, P. S. Davids, *Opt. Express* **2017**, *25*, 16130.
- [260] H. Wang, Y. Shi, Y. Zuo, Y. Yu, L. Lei, X. Zhang, Z. Qian, *Nanophotonics* **2023**, *12*, 705.
- [261] 3D-Integration on Wafer Level of Photonic and Electronic Circuits Citation for Published Version (APA): Spiegelberg, n.d.
- [262] Y.-A. Chen, Q. Zhang, T.-Y. Chen, W.-Q. Cai, S.-K. Liao, J. Zhang, K. Chen, J. Yin, J.-G. Ren, Z. Chen, S.-L. Han, Q. Yu, K. Liang, F. Zhou, X. Yuan, M.-S. Zhao, T.-Y. Wang, X. Jiang, L. Zhang, W.-Y. Liu, Y. Li, Q. Shen, Y. Cao, C.-Y. Lu, R. Shu, J.-Y. Wang, L. Li, N.-L. Liu, F. Xu, X.-B. Wang, et al., *Nature* **2021**, *589*, 214.
- [263] S.-K. Liao, W.-Q. Cai, W.-Y. Liu, L. Zhang, Y. Li, J.-G. Ren, J. Yin, Q. Shen, Y. Cao, Z.-P. Li, F.-Z. Li, X.-W. Chen, L.-H. Sun, J.-J. Jia, J.-C. Wu, X.-J. Jiang, J.-F. Wang, Y.-M. Huang, Q. Wang, Y.-L. Zhou, L. Deng, T. Xi, L. Ma, T. Hu, Q. Zhang, Y.-A. Chen, N.-L. Liu, X.-B. Wang, Z.-C. Zhu, C.-Y. Lu, et al., *Nature* **2017**, *549*, 43.
- [264] Silicon Photonics Market Analysis Report | 2022-2030, <https://www.nextmsc.com/report/silicon-photonics-market>.
- [265] Silicon Photonics Market Market Size, Revenue Trends and Growth Drivers | MarketsandMarkets, <https://www.marketsandmarkets.com/Market-Reports/silicon-photonics-116.html>.
- [266] Semiconductor Photonic Integrated Circuits 2023-2033: IDTechEx, <https://www.idtechex.com/en/research-report/semiconductor-photonics-integrated-circuits-2023-2033/914>.
- [267] EPIC Online Technology Meeting on Microwave Photonics - EPIC Association, <https://epic-assoc.com/events/epic-online-technology-meeting-on-microwave-photonics/>.
- [268] *Nat. Photonics* **2011**, *5*, 724.
- [269] Quantum Photonics Market Size, Share, Industry Report, Revenue Trends and Growth Drivers, [https://www.marketsandmarkets.com/Market-Reports/quantum-photonics-market-9223814.html?utm\\_source=Globenews&utm\\_medium=referral&utm\\_campaign=paidpr](https://www.marketsandmarkets.com/Market-Reports/quantum-photonics-market-9223814.html?utm_source=Globenews&utm_medium=referral&utm_campaign=paidpr).
- [270] 6 Companies Working with Photonic Quantum Computing 2022, <https://thequantuminsider.com/2022/03/24/6-quantum-computing-companies-working-with-photonic-technology/>.
- [271] BlackRock, Others Invest \$450 Million on PsiQuantum, <https://thequantuminsider.com/2021/07/27/investors-see-the-light-as-blackrock-leads-450-million-series-d-investment-into-psiquantum/>.
- [272] Quantum Computing Market Size And Share Report, 2030, <https://www.grandviewresearch.com/industry-analysis/quantum-computing-market>.
- [273] Quantum Communication Market Size, Share & Industry Analysis - 2032, <https://www.marketresearchfuture.com/reports/quantum-communication-market-12240>.
- [274] BeamPROP Beam Propagation Method Software - RSoft Photonic Device Tools | Synopsys Photonic Solutions, <https://www.synopsys.com/photonic-solutions/rsoft-photonic-device-tools/passive-device-beamprop.html>.
- [275] OptiBPM Overview, <https://optiwave.com/optibpm-overview/>.
- [276] Optical Propagation Software using EigenMode Expansion (EME) - FIMMPROP, <https://www.photond.com/products/fimmprop.htm>.
- [277] Ansys Lumerical FEEM | Waveguide Simulator, <https://www.ansys.com/products/photonics/feem>.
- [278] CAMFR Home Page, <https://camfr.sourceforge.net/>.
- [279] MEEP Documentation, <https://meep.readthedocs.io/en/latest/>.
- [280] gprMax: Electromagnetic simulation software, <https://www.gprmax.com/>.
- [281] openEMS | openEMS is a free and open electromagnetic field solver using the FDTD method, <https://www.openems.de/>.
- [282] RSoft Photonic Device Tools | Component Design Software | Synopsys, <https://www.synopsys.com/photonic-solutions/rsoft-photonic-device-tools/rsoft-products.html>.
- [283] Simulazione Ansys: l'ingegneria del futuro, [https://www.esss.co/it/simulazione-ansys/?utm\\_source=google&utm\\_medium=paidsearch&utm\\_campaign=ansys&gclid=CjwKCAjwyNSoBhA9EiwA5aYlB28ZKAAI5zNPwizVGDra12Eho2lHeUW5hUQkQSiCv4A2pf0vHnuRoCYO8QAvD\\_BwE](https://www.esss.co/it/simulazione-ansys/?utm_source=google&utm_medium=paidsearch&utm_campaign=ansys&gclid=CjwKCAjwyNSoBhA9EiwA5aYlB28ZKAAI5zNPwizVGDra12Eho2lHeUW5hUQkQSiCv4A2pf0vHnuRoCYO8QAvD_BwE).
- [284] Photon Design - Your source of photonics CAD tools, [http://www.photond.com/?gclid=CjwKCAjwyNSoBhA9EiwA5aYlB47yvrFssD3Wt2-88zohBHh3tkx7j9-fY3-f71xyiTOIU21B7kpRoCqHkQAvD\\_BwE](http://www.photond.com/?gclid=CjwKCAjwyNSoBhA9EiwA5aYlB47yvrFssD3Wt2-88zohBHh3tkx7j9-fY3-f71xyiTOIU21B7kpRoCqHkQAvD_BwE).
- [285] Photonic Crystal Simulation Toolkit including Band Solver and FDTD Engine - CrystalWave, <https://www.photond.com/products/crystalwave.htm>.
- [286] FEniCSx | FEniCS Project, <https://fenicsproject.org/>.
- [287] Elmer FEM – open source multiphysical simulation software, <http://www.elmerfem.org/blog/>.
- [288] FreeFEM - An open-source PDE Solver using the Finite Element Method, <https://freefem.org/>.
- [289] COMSOL Software Version 6.0 Release Highlights, <https://www.comsol.com/release/6.0>.
- [290] S. Nakamura, K. Sekiya, S. Matano, Y. Shimura, Y. Nakade, K. Nakagawa, Y. Monnai, H. Maki, *ACS Nano* **2022**, *16*, 2690.
- [291] Z. Xu, C. Qiu, Y. Yang, Q. Zhu, X. Jiang, Y. Zhang, W. Gao, Y. Su, *Opt. Express* **2017**, *25*, 19479.

- [292] S. Gan, C. Cheng, Y. Zhan, B. Huang, X. Gan, S. Li, S. Lin, X. Li, J. Zhao, H. Chen, Q. Bao, *Nanoscale* **2015**, *7*, 20249.
- [293] P. Pan, J. An, Y. Wang, J. Zhang, L. Wang, Y. Qi, Q. Han, X. Hu, *Opt. Laser Technol.* **2015**, *75*, 177.
- [294] S. Pitris, G. Dabos, C. Mitsolidou, T. Alexoudi, P. De Heyn, J. Van Campenhout, R. Broeke, G. T. Kanellos, N. Pleros, *Opt. Express* **2018**, *26*, 6276.
- [295] H. Yu, Y. Yin, X. Huang, D. Tu, Z. Yu, H. Guan, Z. Li, *IEEE Photonics J.* **2023**, *15*, 7900306.
- [296] K. Fotiadis, S. Pitris, M. Moralis-Pegios, C. Mitsolidou, P. De Heyn, J. Van Campenhout, R. Broeke, T. Alexoudi, N. Pleros, *IEEE Photonics Technol. Lett.* **2020**, *32*, 1233.
- [297] S. Yuan, J. Feng, Z. Yu, J. Chen, H. Liu, Y. Chen, S. Guo, F. Huang, R. Akimoto, H. Zeng, *Nanomaterials* **2023**, *13*, 182.



**Nabarun Saha** received his M.Sc. and Ph.D. in physics from the Indian Institute of Technology Delhi (IIT Delhi), New Delhi, India, in 2014 and 2020, respectively. After completing his Ph.D., he worked as a visiting researcher in Taiwan and a project scientist at IIT Delhi and IIT Kanpur. After that, he joined the Polytechnic University of Bari, Italy, as a postdoctoral researcher, where he is currently a researcher (RTDA). His areas of research focus on the development of integrated optoelectronics and photonics devices and systems, primarily within the realms of biomedical and space applications.



**Giuseppe Brunetti** received the M.Sc. in electronic engineering (cum laude) and Ph.D. in information engineering from Polytechnic University of Bari, Bari, Italy, in 2016 and 2020, respectively. His Ph.D. was focused on innovative photonic and optoelectronic devices for space applications with European Space Agency (ESA) sponsorship in the framework of the NPI project (367-2014). Since December 2020, he has been an assistant Professor at the Polytechnic University of Bari. His research interests include integrated optoelectronics and photonics devices and systems mainly in the context of the biomedical and Space field.



**Annarita di Toma** received her M.Sc. in electronic engineering (cum laude) from the Polytechnic University of Bari, Bari, Italy, in 2022. In 2022, she has joined the Optoelectronics Group. She is currently working toward a Ph.D. in the development of photonic devices and systems for space and biomedical applications.



**Mario Nicola Armenise** received the Laurea degree in electrical engineering from the University of Bari, Bari, Italy. Since 1986, he has been a full professor of optoelectronics with the Polytechnic University of Bari and retired in 2013. From 1994 to 1997, he was the deputy rector of the Polytechnic University of Bari. From 2004 to 2011, he was the chair of the Consortium of the Apulian Universities (CIRP). He is the author or coauthor of about 400 journal articles and conference talks, and the coinventor of two international patents. His research interests include integrated optoelectronics and photonics. He was a visiting professor at several universities and was invited to give seminars in Europe, the U.S., Japan, and former Eastern European countries. He is a fellow of the European Optical Society and was the president of the Italian Electronics Society and the Italian Optics and Photonics Society. He was a member of the Scientific Council of the Department of Science and Technology of Communications and Information of the French National Committee of Scientific Research, the Scientific Council of the Italian Space Agency, and the Scientific Council of the Department of Materials and Technologies of the Italian National Council of Research. He was the chair, co-chair, or member of the Program Committee of numerous international conferences. He gave invited talks at many international conferences. He has been the scientific coordinator of several national and international research projects. His research interests include integrated optoelectronics and photonics.



**Caterina Ciminelli** received the Laurea degree (1996) and Ph.D. (2000) in electronic engineering from the Polytechnic University of Bari, Italy. From 1999 to 2002, she did industrial research activity on optoelectronic components and subsystems with the R&D Division of Pirelli Optical Systems and Cisco Photonics, Italy, before joining the Polytechnic University of Bari as an assistant professor of electronics in 2002. From 2012 to 2021, she has been an associate professor. Since 2021, she has been a full professor at the Polytechnic University of Bari where she is the scientist responsible for the Optoelectronics Laboratory. She is the author or coauthor of more than 200 journal articles and conference papers. She is involved in several research projects, also as scientific coordinator. Her research interests include integrated optoelectronics and photonics.